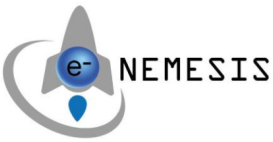

Justus-Liebig-Universität Gießen

I. Physikalisches Institut

Characterization of C12A7:2e- electride and its application in electric propulsion cathodes

Charakterisierung des Elektrids C12A7:2e- und dessen Anwendung in Kathoden für elektrische Triebwerke

Dissertation

zur Erlangung
des Grades
„Doktor rerum naturalium“
im Fach Physik

Malina Katrin Reitemeyer

Gießen 2024

Betreuer und Erstgutachter:	Prof. Dr. Peter Klar
Zweitgutachter:	Prof. Dr. Hans Leiter

Abstract

Die Kathode oder Neutralisator ist eine Hauptkomponente vieler elektrischer Antriebssysteme. Solche Kathoden stellen mittels plasmagestützter thermischer Emission Elektronen für das Triebwerksplasma und die Strahlneutralisation bereit. Das Elektridmaterial C12A7:2e- ist durch seine niedrige Austrittsarbeit ein vielversprechender Kandidat für zukünftige Kathoden. In dieser Arbeit werden Hall-Effekt-Messungen, Gewichtsänderung durch Oxidation, ESR und Raman-Spektroskopie verwendet, um Elektride verschiedener Elektronenkonzentrationen zu untersuchen. Die Ladungsträgerdichten aus Hall-Effekt-Messungen und der Reduktionsgrad, abgeleitet aus der Gewichtszunahme durch Oxidation korrelieren mit dem Raman-Spektrum, genauer mit dem Intensitätsverhältnis der Phonenbande bei 521 cm^{-1} und der Doppelbande um 600 cm^{-1} . Dies erlaubt eine einfache und non-invasive Beurteilung der Probenqualität mittels Ramanspektroskopie. Darüber hinaus wurden zwei Kathodenkonzepte mit scheibenförmigen Elektridinserts getestet. Das erste Design, eine thermionische Plasmakathode, wurde erfolgreich über mehrere Stunden betrieben und erreicht Extraktionsströme bis zu 1,4 A (1 A Keeper, 0,4 A Anode). Außerdem wurden Auswirkungen von Veränderungen des Insertmaterials identifiziert und mögliche Lösungen untersucht. Das zweite Design verwendet einen Magneten zur besseren Ionisation und kann bei Raumtemperatur gezündet werden. Es werden Ströme bis zu 70 mA erreicht. Verschiedene alternative Treibstoffe wurden untersucht, darunter Iod. Auch wurden Tests mit mehreren hundert Betriebsstunden mit Krypton durchgeführt. Verschiedene Verschleißmechanismen und deren Einfluss auf die Leistung der Kathode werden über den Verlauf des Tests untersucht.

A key component for many electric propulsion systems is the cathode or neutraliser. By combining the thermionic emission of a low work function material with a plasma environment, the device provides electrons for the thruster's plasma and beam neutralisation. The electride material C12A7:2e- offers a low work function and good ambient stability, making it a promising candidate as a cathode insert material. In this work, Hall effect measurements, weight gain by oxidation, EPR and Raman spectroscopy are applied to electride material over a wide range of electron concentrations. In particular, the carrier densities obtained by Hall effect measurements and the reduction degree obtained from weight gain by oxidation technique correlate with features in the Raman spectrum, to be specific with the intensity ratio of the phonon band at 521 cm^{-1} with respect to the double band at 566 cm^{-1} and 610 cm^{-1}. This allows a simple and non-intrusive assessment of sample quality based on the Raman spectrum of a sample. In addition, two cathode design concepts using disk-shaped C12A7:2e- electride inserts were tested. The first design, a thermionic plasma cathode, is successfully operated for several hours and achieves currents up to 1.4 A (1 A keeper, 0.4 A anode). Furthermore, reasons for voltage drifts and instabilities due to changes in the insert material are analysed and possible solutions identified. The second design uses a magnet to enhance gas ionisation and can be ignited at room temperature. Currents up to 70 mA are achieved. Various alternative propellants are studied, including iodine. In particular, several hundred hours of operation are performed with krypton as propellant. Insert degradation and device performance are closely monitored throughout the test.

Contents

Chapter 1

Motivation

Over the last decades, space flight has evolved from a niche technology, mainly used for military and scientific purposes to a backbone of modern infrastructure. Its fields of use vary nowadays from interplanetary scientific missions, over still costly, but more frequent telecommunication satellites to constellations formed of hundreds of small, low-cost satellites. This wide range of mission scopes poses different demands on the mass, reliability and cost-efficiency of the spacecraft, which have to be met also by its propulsion system. Different propulsion systems have been developed over the years, which can be discriminated by their energy source for thrust production. Chemical propulsion systems use a chemical reaction which releases energy from the propellant itself. Electric propulsion uses the propellant merely as a carrier medium and generates thrust by electrical power. The achieved velocity change Δv is determined by the exhaust velocity c_e and the ejected propellant mass Δm in relation to the total mass m_0

$$\Delta v = c_e \cdot \ln\left(\frac{m_0}{m_0 - \Delta m}\right). \tag{1.1}$$

For a given mass budget a high exhaust velocity is therefore desirable and has become a deciding factor for propulsion systems. As universal measure for a thruster's performance, the specific impulse I_{sp} has been established

$$I_{sp} = \frac{\dot{p}}{\dot{m} \cdot g_0} = \frac{c_e}{g_0}. \tag{1.2}$$

It describes the effective exhaust velocity, normalised with the standard gravitational acceleration. Thrusters with a higher specific impulse thus require less propellant for the same Δv, as it can be seen from the equations above. Compared to chemical propulsion systems, which have specific impulses in the range of 150 s to 500 s, electric propulsion systems possess higher specific impulses from 300 s to 10 000 s [79]. This allows for systems

with less propellant per Δv, which makes them attractive for mass- or cost-sensitive missions. Also, with the same propellant budget higher Δv can be achieved with electric propulsion. This is particularly interesting for deep-space missions, where probes with chemical propulsion systems have to rely on rare planetary constellations for swing-by manoeuvres. The disadvantage of electric propulsion, however, is the comparably low thrust of these systems. Therefore, certain orbital manoeuvres, which require short, high-thrust burns have to be adapted for electric propulsion systems. The most famous example is the geostationary orbit insertion. Here, an upspiralling trajectory has to be chosen when using electric thrusters.

Different types of thrusters have been developed to take advantage of the efficient thrust generation. Based on their operating principle, they are grouped into electro-thermal, electrostatic and electromagnetic thrusters. All make use of electric forces accelerating their propellant to velocities up to 50 km/s [79]. While some electric thrusters emit both ions and electrons, especially the most common designs of Hall effect thrusters (HET) and gridded ion engines (GIE), just extract ions from their plasma. On the long scale, this would lead to an accumulation of positive charge on the satellite, which would impede thrust and disturb systems on board. Therefore, an additional electron emitting unit, the so-called cathode or neutralizer, is needed. Different designs are presented in academic research, like microwave or inductively coupled plasma cathodes. However, the dominating flight-proven concept is that of a thermionic hollow cathode. The thermionic plasma cathode uses a low work function material to generate thermionic electrons by applying heat to the material. With these electrons and a gas flow through the device, a plasma can be ignited in the device from which electrons can be extracted. A detailed discussion about these devices will be given in Section 3.1. Essential for thermionic cathodes are low-work function materials, to limit the required operation temperature. Typically, barium oxide in a tungsten matrix (BaO-W) or lanthanum hexaboride (LaB6) are used as emitter material. Each material poses certain challenges to the device: BaO-W is highly sensitive to oxygen residuals in the propellant and the surrounding atmosphere and thus requires highly purified propellant and meticulous ground-testing. LaB6 on the other hand is more resistant to oxygen poisoning, but requires significantly higher operating temperatures around 1600 °C, contrary to BaO-W, which is operated at about 1100 °C. Also, when using LaB6 the risk of boron diffusion has to be considered, which limits the choice of materials in contact with the emitter material.

A promising alternative to these materials is the electride C12A7:2e-. Dis-

covered in 2003, is possesses a unique crystal structure, where anions can be bound inside calcium-aluminium-oxide-cages. In its electride form, these lattice sites are occupied by loosely bound electrons. The material is based on the oxide C12A7:O^{2-}, called mayenite, from which it can be derived by applying a highly reducing environment. The reduction degree from oxidized C12A7 to C12A7:2e- electride is an important property as it relates to other material characteristics such as the band structure or the electric conductivity. For this work, charge carrier densities and Raman spectra for electrides of various reduction degrees were measured to study its impact upon the material's properties. Systematic studies have so far only been performed on a series of electride glasses but not on material in its poly-crystalline form, which is the one used in cathode applications. Further details about C12A7:2e- electride are given in Chapter 2. Particularly important for the resulting thermionic emission current provided by the electride is its work function. A setup for measuring thermionic emission was therefore developed and electride and LaB6 samples were studied.

In cathode designs using a hollow cylinder insert, the heat that arises must be dissipated through the material. In the case of C12A7:2e- this often leads to melting of the insert material due to its low melting point of 1415 °C combined with a low thermal conductivity. Promising alternatives are therefore cathode designs that use a planar geometry. This facilitates the manufacturing of the insert and reduces the thermal load on the insert. In Chapter 3 of this work, two different designs using a planar geometry and a C12A7:2e- insert are presented. The first design, presented in Section 3.2, uses the design concept of a thermionic plasma cathode. An external heater is used for ignition and for maintaining the operating temperature. The design process is described with improvements derived from initial test results. The resulting design can be operated stably for several hours, currents up to 1.4 A (1 A keeper, 0.4 A anode) are achieved. Furthermore, a detailed analysis of device operation is presented. The second design, presented in Section 3.3, includes a magnet underneath the insert to enhance plasma generation. A special pulse mode was found to significantly stabilise the plasma and improve performance. The cathode was tested with various alternative propellants, including iodine. In addition, an endurance test of 300 hours with krypton as propellant was carried out with regular performance characterisation. Accompanying Raman spectroscopy of the insert made it possible to analyse compositional changes of the insert material during the endurance test.

Chapter 2

C12A7:2e- electride

C12A7:2e- promises advances to a variety of fields thanks to its unique electronic structure. It originates from the cage like framework of the crystal structure of its parent material, mayenite. In an ionic picture, the cage framework can be considered positively charged where the cages within this structure provide low-energy binding sites, which are normally occupied by negatively charged oxygen. A reduction process allows this oxygen to be extracted in its neutral state. The remaining electrons occupy the vacant oxygen binding sites, making C12A7:2e- an electride: A material in which anion defects act as donors and provide electrons. Unlike other electrides, C12A7:2e- is thermally and chemically stable at ambient conditions [60]. Also, the resulting cage electron density can be controlled by the synthesis process [58, 60]. This chapter begins with an overview of the material's crystal and resulting band structure and describes the synthesis methods to obtain C12A7:2e-. The resulting electronic properties have a major impact on potential applications. However, in the literature, samples are classified by different characterisation methods. Due to the lack of published comparisons between characterisation techniques, it is therefore difficult to effectively assess performance for different applications. This work uses a wide-spread set of C12A7:2e- samples of different degrees of reduction and production methods. The response to this divergence in sample quality is studied by four different techniques: Hall effect measurements, electron spin resonance, weight difference upon oxidation and Raman spectroscopy. In particular, correlations between these techniques are investigated, to allow for a method-independent assessment of C12A7:2e- samples.

2.1 Crystal Structure

The starting material for obtaining C12A7:2e- is C12A7:O^{2-}. C12A7 is in this case the cement chemical notation for 12 calcium oxide units CaO and 7 aluminium oxide units Al_2O_3 [5, 56]. These constituents form a zeolite-like cage structure, where in particular AlO_4 tetrahedra form the framework of the crystal [8, 43]. The tetrahedra, connected by a shared edge oxygen, are discriminated into two groups [78]: Twelve Al(2) tetrahedra (per unit cell) are connected to other tetrahedra via all four corners. The connecting oxygen at the corners is thereby called *bridging oxygen* and will be referred to as O(1) in the following. The other sixteen Al(1) tetrahedra share only three of their four oxygen atoms with other tetrahedra. The remaining oxygen, called O(2), may engage in bonds with calcium in the crystal [8, 90]. The calcium ions themselves are disordered in the crystal and only weakly bound to the surrounding framework [8]. Key to this particular crystal structure are the cages formed within the framework, each about 0.4 nm [57] to 0.6 nm in diameter [8][1]. A cage consists of six calcium, eight aluminium and sixteen oxygen atoms [109] and is symmetric with respect to the S4 axis, which passes through two opposite calcium atoms [90, 109]. Such a cage cell can be seen with its axis of symmetry in Figure 2.1b. Viewed in the ⟨100⟩-plane, a ring of Ca-O-Al-O-(Al or Ca)-O-Ca-O-(Al or Ca)-O-Al-O surrounds the cage centre [8]. Each cage shares its sites with eight directly adjacent cages of different orientation. Additional bonds are formed to four other cages [108]. Such an arrangement of neighbouring cages is shown in Figure 2.1a. In total, a unit cell, consisting of two stochiometric units of C12A7, contains 12 cages. The internal volume of the cages makes up a significant proportion of the unit's cell total volume, depending on the method of calculation up to 50% [109]. C12A7 belongs to the $I\bar{4}3d$ space group with a lattice constant of 1.198 nm [12].

The lattice structure $[Ca_{24}Al_{28}O_{64}]^{4+}$ is 4 times positively charged per unit cell [44], which allows anions to be loosely bound to the cage wall cations, i.e. calcium and aluminium [39, 90, 109]. Main binding partners are the two calcium cations located on the symmetry axis of the cage. In its oxide form two of the twelve cages contain double negatively charged oxygen O^{2-}, which is located off the symmetry axis [109, 90]. This bound oxygen leads to a displacement of the two calcium cations located on the symmetry axis and an aluminium atom Al(1) [90, 109], which in turn results in a significant reduction of the cage diameter [8, 60, 69, 109] and distorts the surrounding lattice. In particular, a significant divergence between occu-

[1] As discussed later in this section, this diameter is strongly influenced by the occupancy of the cage [60, 109].

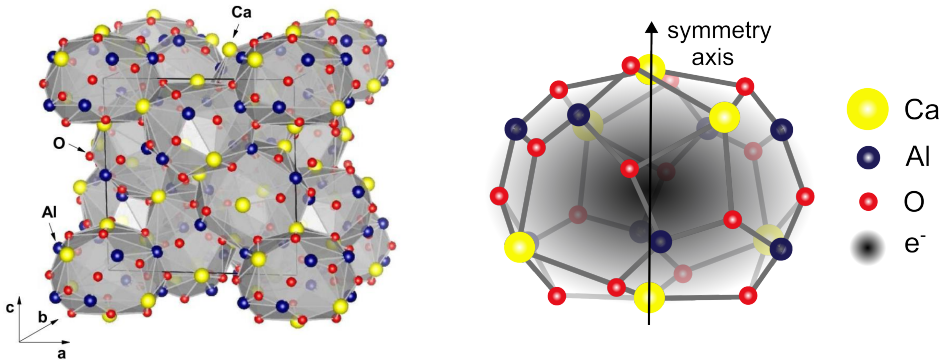

(a) (b)

Figure 2.1: Crystal structure of C12A7:2e- a) View of several cages, with the black cube corresponding to a unit cell. Reprinted (adapted) with permission from [87]. Copyright 2019 American Chemical Society. b) Crystal structure of a C12A7 cage. Inside the cage an anion such as O^{2-} or an electron can be bound. In this case C12A7:2e- is shown. The delocalised electron is shown as a grey cloud in the centre of the crystal. The symmetry axis of the cell passes through two calcium atoms. Reprinted (adapted) with permission from [60]. Copyright 2007 American Chemical Society.

pied and unoccupied cages is visible [60].

Using the synthesis techniques described in Section 2.3, the O^{2-} cage anion can be extracted from the cage as neutrally charged oxygen. The two electrons, previously associated with the oxygen anion, remain in the cages. These electrons are not bound to a specific atom in the crystal, but to the entire cage structure [109]. The resulting system can be expressed by $[C12A7]^{2+}$: $[2e^-]^{\delta}$ $[O^{2-}]^{(1-\delta)}$ where the parameter $\delta = [0, 1]$ represents the degree of reduction. In the following, the short form of C12A7:2e- will be used for all electrides, regardless of their degree of reduction and the term C12A7:O^{2-} will be used for the oxide form of C12A7. Due to the altered cage occupancy, the distortion of the formerly anion-binding cages decreases and approaches the morphology of an empty cage. In particular, the cage diameter increases with increasing degree of reduction [60, 90]. In the case of complete replacement, the cage diameter is close to that of an empty cage [60]. This leads to an expansion of the whole unit cell with increasing cage electron concentration [90]. However, this change in cage diameter does not significantly affect the unoccupied cages. Their diameter remains almost unchanged, regardless of the degree of reduction [109]. Unlike to other low work function materials, the electron in the cage is protected from ambient conditions by the cage wall, which inhibits oxygen diffusion into the cage [116]. This is the reason for the electride's extraor-

dinary chemical and thermal stability.

The surface structure of C12A7:2e- electride is of particular importance for applications as electron emitters. However, as-prepared samples exhibit low to insulating surface conductivity [104, 116, 117]. The reason for this is the mechanical treatment of the samples during the production process, in particular the cutting or polishing of the samples. During this process, the unique crystal structure of C12A7 is damaged and broken cages remain at the sample's surface. Therefore, no cage-related binding sites (CCB states) exist at the surface [104], i.e., the cages cannot be occupied by electrons (or anions) and an insulating surface layer establishes. This hypothesis is supported by measurements of the layer's thickness, which is about the size of a single cage [104, 116]. Since the positively charged framework is not balanced by negative cage occupants, the surface layer is positively charged and extends as depletion regime into the bulk. The extension is determined by the free carrier density, which scales with the degree of reduction of the sample, i.e., the surface layer is smaller for samples with a higher degree of reduction [75]. Also process temperatures above 200 °C during the mechanical process can lead to oxygen incorporation into the surface cages [139]. To restore the surface cages and remove possible adsorbed oxygen, the electride can be sputter annealed in a highly oxygen-deficient atmosphere [117]. STM imaging confirmed an intact cage surface and a good electrical conductivity after the treatment, even after the sample was exposed to ambient conditions [117]. Ref. 87 even stated, that in the case of intact cages, the cage electron density directly at the surface is higher than in the bulk. It should be noted, that the samples used in this work did not undergo such an annealing process.

2.2 Band structure and electron conduction

C12A7:O^{2-} is an insulator with a band gap of 7 eV [109]. The maximum of the framework valence band (FVBM) is located at -5 eV relative to the Fermi energy [109]. This band consists mainly of 2p orbitals of the framework oxygen [109]. The position of the cage oxygen off the cage symmetry axis, as mentioned above, causes a splitting of some framework oxygen 2p states, leading to a broadening of the framework valence band up to -3.0 eV [109]. At this energy level, also the cage oxygen 2p binding states are found. At 4 eV above the Fermi energy the framework conduction band (FCB) begins [109]. The corresponding band diagram is shown in Figure 2.2.

A speciality of C12A7 lies in its unoccupied cage states. These represent

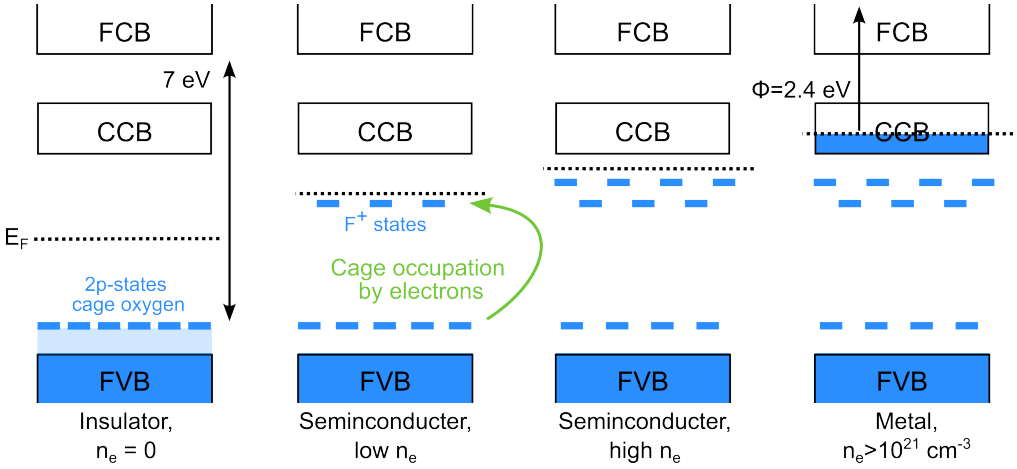

Figure 2.2: Evolution of the band structure of C12A7:2e- for different degrees of reduction. In the C12A7:O^{2-} state, i.e. $\delta = 0$, the material is an insulator with a band gap of 7 eV. Replacing the O^{2-} anions in the cages with electrons creates F^+ states below the cage conduction band. With increasing degree of reduction further F^+ states form closer to the CCB and the Fermi energy E_F approaches the CCB. At $n_e > 10^{21}$ ($\delta \approx 0.5$) C12A7:2e- is a metallic conductor with the Fermi energy located in the cage conduction band. In this case the material has a work function of 2.4 eV. The occupied states are shown in blue. FVB stands for framework valence band, CCB for cage conduction band and FCB for framework conduction band.

additional possible bonding sites in the crystal, which together form the so-called *cage conduction band* (CCB), located between the framework valence band and the framework conduction band. In the case of C12A7:O^{2-} this cage conduction band represents the empty cages and is found between 2.0 eV and 2.8 eV [109]. The cage conduction band is not to be considered as a sum of orbitals of surrounding lattice framework atoms, but rather as a linear string of 1s orbitals, analogous to finite potential wells with the cage structure serving as the potential barriers [60, 109].

As the oxygen anions in the crystal are gradually extracted, the band structure and the conductivity of the material also change [134]. These changes result partly from the reduced lattice distortion at lower oxygen densities, as described in Section 2.1, and partly from the new electron binding states. The first effect, the reduced lattice distortion, also reduces the dispersion of the 2p oxygen framework states. Thus, the FVBM decreases to below -5.5 eV, increasing the gap between the FVBM and the FCBM to -7.5 eV [109, 115, 116]. The CCB also narrows as the number of empty cages decreases, since the charge equivalent amount of electrons occupies more cages than oxygen (it is assumed that inside each cage only one electron is located) [109].

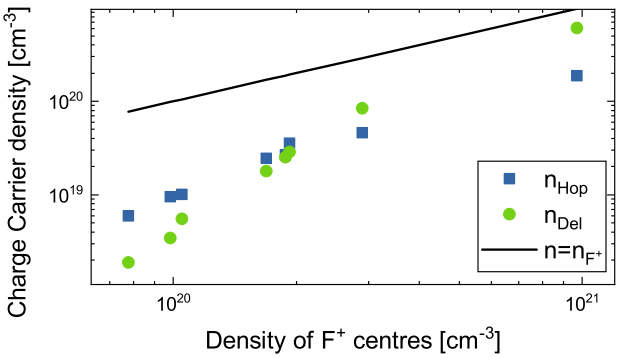

Figure 2.3: Evolution of the charge carrier densities of the two main conduction types in C12A7:2e- electrides, i.e., hopping conduction and transport by delocalised electrons, with increasing F^+ centre density. Data from Ref. 18 Fig. S2 d.

In terms of electron binding states, the electrons in the cages can be described as donor-like oxygen vacancies [58] or *F^+-like centres* [24, 116]. F^+ centres are a specific type of defect in a crystal structure: An anion vacancy provides an electron bound to the vacancy. This electron is in a hydrogen-like 1s state and behaves like a particle in a box [48, 101]. The F^+ centre/ cage electron density can be directly related to the degree of reduction δ of the electride with a maximum of $n_e = 2.33{\cdot}10^{21}\mathrm{cm}^{-3}$ [58] for a fully reduced sample ($\delta = 1$). At very low F^+ centre densities, the 1s states of the F^+ centres are located 0.4 eV below the cage conduction band [18]. To contribute to charge transport, electrons must overcome this potential barrier. Therefore, only those F^+ centre electrons with sufficient thermal energy contribute. According to Dinter et al. charge transport in C12A7:2e- electride comprises three different mechanisms: hopping conduction, where electrons move in the form of polarons to other cages and require an additional activation energy [74, 107], conduction by delocalised electrons and a surface conduction channel [18]. The contribution of the different mechanisms depends on the temperature and the degree of reduction. A summary of the respective charge carrier densities for a given F^+ centre density is shown in Figure 2.3. With increasing degree of reduction, the cage distortion continues to decrease and the F^+ centre states (cages containing electrons) approach the CCB (empty cages). For cage electron densities above $5{\cdot}10^{20}\mathrm{cm}^{-3}$ these two states start to overlap and form a joint impurity band with localised and delocalised states [75].

As the degree of reduction increases, the divergence between the occupied and unoccupied cages continues to decrease and more electrons populate

delocalised states [75]. At $n_e \approx 1{\cdot}10^{21}\mathrm{cm}^{-3}$ ($\delta \approx 0.5$) the semiconductor-metal transition occurs and C12A7:2e- becomes a metallic conductor [75, 60]. The Fermi level is located within in the cage conduction band. However, even in the metallic state some of the electrons remain localised in the cages [109, 75]. In this case, the Fermi energy is located 2 eV below the framework conduction band [116]. With an energy gap of 0.4 eV between the vacuum potential and the framework conduction band minimum, a work function of 2.4 eV results.

2.3 Synthesis

The synthesis of C12A7:2e- electride is a challenging process, for which several procedures have been developed in recent years. Except for the last process presented in this section, all involve a two-step process: First, the precursor material C12A7:O^{2-} is synthesised and subsequently reduced to C12A7:2e- electride. C12A7:O^{2-} is in most cases obtained from a reaction of $CaCO_3$ with γ-Al_2O_3. The solid mixture is heated in air for several hours at temperatures around 1300 °C [8, 39, 50, 56]. According to Ref. 25 the ambient atmosphere during the process results in a high phase purity. To convert this material to C12A7:2e- electride with its unique properties, the oxygen atoms in the cages have to be removed causing negatively charged oxygen vacancies. This can be achieved by various techniques, presented hereinafter.

The first method uses a metal vapour treatment, either with calcium [74], titanium [60] or vanadium [89] to reduce the mayenite and to extract the cage oxygen. The sample is sealed with the metal pellets in vacuum and heated to 700 °C for calcium treatment and about 1000 °C for titanium and vanadium. This treatment forms a thin metal layer on top of the sample which reacts with the cage oxygen close to the surface. Bulk atoms reach the surface by diffusion and also react with the respective metal [59]. The oxygen vacancies, forming in the C12A7, are double donors. The degree of reduction can be adjusted by the process time [74] and an almost complete reduction of C12A7 can be achieved [54]. This method precludes the incorporation of other anions such as OH^-, but the resulting metal oxide surface layer has to be subsequently removed by polishing. In the case of CaO (in the calcium process) this layer acts as a diffusion barrier to the cage oxygen, limiting the maximum achievable degree of reduction and leading to very long process times of several tens of hours [59]. Therefore, this process is limited to single crystals and thin films. These problems do not apply to titanium as reducing agent.

A reducing atmosphere without the disadvantages of a metal oxide surface layer uses carbon as the reducing agent [58]. The sample is heated in a carbon crucible to a temperature above 1000 °C with a nitrogen or argon gas flow for several hours [58, 50]. This creates a highly oxygen-deficient atmosphere with an oxygen partial pressure of about 10^{-18} atm [58]. The vaporised carbon reacts with the cage oxygen to form CO or CO_2, both of which are gaseous and leave no reaction residues on the sample surface. In this case the process duration has little effect on the degree of reduction. Instead, the cage electron density increases with process temperature [58, 50]. However, only degrees of reduction below 0.05 can be achieved by this method [54]. Conflicting results exist as to whether phase decomposition of C12A7 occurs above 1100 °C process temperature [58, 50]. The process is applicable to various forms of C12A7 such as polycrystalline material, single crystals or thin films [59].

A slightly different process uses a combination of C12A7:O^{2-}, C3A and aluminium in a mixture corresponding to the stochiometric composition of C12A7:2e- electride ($Ca_{12}Al_{14}O_{32}$). By a brief application of spark plasma sintering in an argon atmosphere, the composition reacts to high-quality electride with a degree of reduction over 0.5 [67]. Compared to other processes that achieve such a high sample quality, no reaction residue is left on the sample surface and the process is considerably shorter.

Instead of chemical reactions, a physical method called ion implantation can be used to extract the cage oxygen from C12A7:O^{2-} [81, 83]. Inert gas cations, mostly Ar^+, are accelerated in a vacuum to bombard the sample's surface. The oxygen is removed from the cages by atomic collisions [59]. The inert gas ions diffuse out of the material shortly after the process and only a few remain in the crystal [83]. This method allows precise control of the resulting cage electron density. In addition, this process precludes contamination due to the absence of additional substances. However, only thin films can be converted to electride by this process [58, 59], due to the micrometre depth of implantation [83].

The processes described above all involve two steps to synthesise C12A7:2e- electride: The preparation of the C12A7:O^{2-} oxide and the subsequent reduction to C12A7:2e- electride. These two steps can also be combined into a single step, making this process particularly interesting for mass production [58]. Instead of synthesising C12A7:O^{2-} as an intermediate, the melt solidification process derives the electride directly from the precursors C3A and CA, which are either sintered into pellets or used directly in powder form. To synthesise C12A7:2e- electride, the precursors are

heated in a graphite crucible with argon gas flow up to 1400 °C for several hours [50]. The process temperature was found to be critical to avoid the formation of other calcium aluminate phases in the process. Also important are so-called template anions to allow for the nucleation of the C12A7 specific crystal structure: For the C12A7 oxide, O^{2-} acts as a template anion, but OH^- or C_2^{2-} are also valid. In the absence of such template anions, C12A7 does not crystallise at all or decomposes into other calcium aluminate phases at high temperatures [56, 89]. The use of a graphite crucible combines the advantage of an oxygen-deficient atmosphere, as described above, with the provision of non-oxygen template anions. It is assumed that the cage crystal structure form with C_2^{2-} as template anion as the melt crystallises [56]. During cooling, the carbon is released from the cages, leaving bound electrons to form C12A7:2e- electride. Initially, C12A7:O^{2-} was proposed as starting reagent by the Hosono group [56, 57]. In this case, two heating cycles were used to first decompose the C12A7 into C3A and CA with incorporated C_2^{2-} template anions. A second heating cycle was then used to obtain C12A7:2e- as described above. However, recent research has found that the direct use of C3A and CA as precursors results in higher degrees of reduction [50], although this result has only been documented for powders. Degrees of reduction of up to 0.15 have been reported for this technique [50]. The inability to synthesise single crystals is the only drawback of this method.

In addition to the cage anion, other components of C12A7 can be modified by doping to improve the material's properties. In general, two approaches for C12A7 doping can be distinguished: First, the broadening of the C12A7 characteristic cages and thereby an enhanced diffusion of the cage anions/ electrons. Second, n-type doping to increase the number of electrons available for charge transport and other applications. To increase the cage diameter, elements from the same group of the periodic table, but of a higher period are preferred. In the case of aluminium this could be gallium [90], but the material obtained was found not to be stable during the reduction process. Instead of calcium, strontium or barium can be used. The replacement of calcium in C12A7 by strontium was performed either partially [82, 137] or completely [84, 85]. Strontium was found to widen the cages in the lattice framework due to its larger ionic radius, leading to an increased lattice constant of 1.233 nm upon complete replacement [82, 131]. The increased cage diameter increases the diffusion of cage anions/ electrons [85, 136]. Apparently this also affects the rate of reduction during synthesis: For a higher Sr concentration, a higher degree of reduction is achieved within the same process time [136, 137]. The result is among others an increased conductivity [137]. Optical absorption

and electronic band structure simulations also indicate a reduced band gap between the CCB and the FCB [85, 137], which means a minimally reduced work function. A disadvantage of Sr-doped C12A7, particularly for use in cathodes, is its lower thermal stability, as it has been reported to decompose at 1040 °C [131]. When lower period elements are used, as magnesium instead of calcium magnesium, the opposite behaviour occurs, i.e. the cages become smaller, and the electronic transport is hindered [6]. The charge total electron density can be increased by replacing aluminium (Al^{3+}) or calcium (Ca^{2+}) with an element of higher valence. Tin (Sn) takes a tetravalent form in C12A7 and introduces thereby an additional electron compared to aluminium. Indeed, a fivefold increase in cage electron density was measured upon replacement of 7% aluminium by tin [45]. A slight shrinkage of the cages was observed in return. As a substitute for calcium, neodymium (Nd) was successfully used to increase the charge carrier density in C12A7:2e- while maintaining the same electron mobility [3].

In this work, C12A7:2e- electride samples obtained from two different reduction processes have been studied. The samples supplied by *Advanced Thermal Devices* were reduced using a titanium treatment. In addition to the previously described C12A7:O^{2-} synthesis procedure, an additional melting step is applied to ensure a pure C12A7 phase. Further details are given in Ref. 25. These samples were subjected to the material characterisation described in this chapter and were also used as cathode insert material in Chapter 3. The electride samples provided by *Fraunhofer Institut für Keramische Technologien und Systeme - Fraunhofer IKTS* were obtained from sintered C12A7:O^{2-} powder. For reduction, the sample was heated in a graphite crucible to obtain a reducing atmosphere. Further details are given in Refs 125 and 126. These samples were also examined using various material characterisation techniques.

2.4 Methods for C12A7 Characterization

Within the complex structure of C12A7, its degree of reduction is of particular interest for evaluating synthesis methods, studying changes in the crystal structure, and analysing changes in the electronic structure and the charge transport behaviour. Comparing literature reports can be challenging due to differences in preparation techniques and sample quality. It is crucial to note that different characterization techniques probe different properties of the material, such as charge carrier density, spin density or optical absorption. The relationship between these parameters and the actual degree of reduction must be taken into account for cross-method analysis. Therefore, this work attempts a comprehensive material charac-

terisation to allow comparisons between different analytical methods. In the following section, four different methods, which provide information on the degree of reduction of C12A7:2e-, are presented. The fundamental principle of each method, previous results obtained for C12A7:2e- electride, and the results obtained in this work are presented. As all of them are more or less indirect methods of obtaining the material's degree of reduction, each method has its particular scope of application and its own limitations on the obtained results.

2.4.1 Hall Effect Measurements

The current flow through a material is determined by the material's conductivity σ as

$$\vec{j} = \sigma \vec{E} \tag{2.1}$$

with the current density $\vec{j}$ and the applied electric field $\vec{E}$. The following definitions describe the charge transport in an isotropic solid as defined in the *Drude model* [102, 133]

$$\sigma = \frac{n_{\text{eff}} e^2 \tau}{m^*} \tag{2.2}$$

$$\sigma = e \mu n_{\text{eff}} \tag{2.3}$$

with the effective charge carrier density n_{eff}, the mean collision time τ, the (effective) charge carrier mass in the band m^*, and the charge carrier mobility μ. In the presence of a magnetic field, the Lorentz force acts on the charge carriers and displaces them perpendicular to the current direction. The displaced charges build up an electric field perpendicular to the current direction. This effect is known as the *Hall effect* and the corresponding field as the *Hall field* [38]. The charge transport under the influence of a magnetic field applied along the z-direction is therefore described by a modified conductivity, the *magneto-conductivity tensor* [18, 102, 133]

$$\sigma_m = \frac{\sigma_0}{1 + (\mu B_z)^2} \begin{pmatrix} 1 & -\mu B_z & 0 \\ \mu B_z & 1 & 0 \\ 0 & 0 & 1 + (\mu B_z)^2. \end{pmatrix} \tag{2.4}$$

In an isotropic steady state system with a moderate magnetic field, the Hall field counteracts the displacement of charge carriers, i.e., $j_y = 0$. Combining this with Equations 2.1, 2.3, and 2.4 gives [48, 102, 133]

$$0 = \frac{\sigma_0}{1 + (\mu B_z)^2} (\mu B_z E_x + E_y) \tag{2.5}$$

$$E_y = -\mu B_z E_x \tag{2.6}$$

$$E_y = -\frac{1}{en} B_z j_x. \tag{2.7}$$

The constant that relates the resulting electric field in y-direction E_y to the magnetic field in z-direction B_z and the current in x-direction j_x is called the *Hall coefficient* R_H

$$R_\mathrm{H} = -\frac{1}{n_\mathrm{eff} e}. \tag{2.8}$$

Measuring the Hall coefficient of a sample is a common technique for determining the charge carrier density n_eff of a material [112]. In case of a non-uniform electron distribution, the Hall coefficient depends on the temperature and the magnetic field due to scattering mechanisms [7, 133]. Contributions from different bands must also be considered [48]. However, in the limit of strong magnetic fields, this modification is close to 1 [112, 133] and the Hall constant saturates [48].

The model presented above describes conduction by an effective charge carrier density. Only in the case of an uniform mobility, i.e., a single conduction band for all charge carriers, this effective charge carrier density is identical to the actual charge carrier density. Otherwise, charge carriers in different bands contribute to the effective charge carrier density weighted by their respective mobility [18, 48]

$$n_\mathrm{eff} = \frac{(\sum_i n_i \mu_i)^2}{\sum_i n_i \mu_i^2} \tag{2.9}$$

As discussed in Section 2.2, the conduction inside C12A7:2e- cannot be described by a single conduction path. The effective charge carrier density, measured by the Hall effect technique, is therefore a mobility-weighted average of the different charge carrier species and cannot be related directly to the cage electron density.

The previously presented relationships for the Hall voltage assume a rectangular rod where the cross-section is small compared to the length. However, the C12A7:2e- samples investigated in this work were platelet-shaped and did not fulfil this requirement. The *van der Pauw method* can be used for such samples with a small height to width ratio [120, 133]. Again, a current is applied between two contacts (here 2 and 4) while the voltage is measured between two other contacts (1 and 3), see Figure 2.4. The change in Hall voltage, caused by the application of a magnetic field B, is then determined. The Hall coefficient is given by [133]

$$R_H = \frac{[U_{13}(B) - U_{13}(0)] \cdot d}{I_{24} B}. \tag{2.10}$$

Van der Pauw showed that the exact position of the contact points does not affect the measured Hall coefficient, as long as they are sufficiently

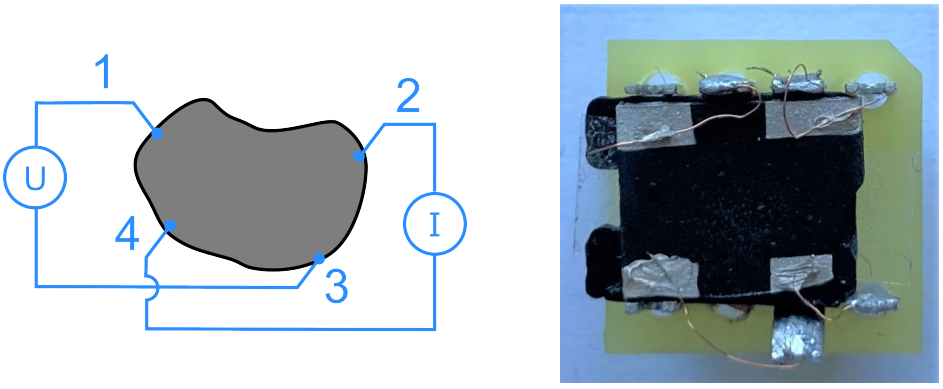

(a) (b)

Figure 2.4: Contacting C12A7:2e- samples in van der Pauw geometry: a) Schematic of four arbitrary contact points around the sample circumference, as required in van der Pauw geometry. The voltage U_{13} and the measured current I_{24} are indicated. b) Measurement setup used for electride samples: The sample is contacted at its four edges with sputter deposited platinum and silver conductive paste.

small and located around the circumference of the sample [121][2]. To avoid errors due to misalignment of the contacts or thermoelectric effects, each configuration is measured in both directions (i.e. U_{13} and U_{31}) and over a range of B with both polarisations of the magnetic field. An average of these values is then used to determine the Hall coefficient. A second configuration, using contacts 2 and 4 for voltage and contacts 1 and 3 for current, was used to verify the isotropy of the sample. From the result the effective charge carrier density can be derived. Together with an additional measurement of the sample's resistivity (without a magnetic field), also in van der Pauw geometry, the mobility and from Equation 2.3 the effective conductivity of the sample can be determined. This is done by applying a voltage between adjacent contact points, i.e. U_{12} and I_{34}. However, since the focus of this work is on the charge carrier density, no further details are given here, but can be found in Ref. 18.

The preparation of ohmic contacts for the C12A7:2e- electride samples is challenging, due to the insulating surface layer of the material. A sputter deposited platinum layer of a few hundred nanometres, applied to the contact points by an aluminium tape mask, results in low-resistance contacts. The commonly used conductive silver lacquer is not recommended, as this leads to a high contact resistance and interferes with the measurements. A detailed study of the contacts for C12A7:2e- showed that a gold contact had the best properties, but platinum was also considered, despite

[2] An estimate of the resulting deviations for misplaced contacts is also given there.

its price [125][3]. The measurements are performed at room temperature. A magnetic field of up to 10 T is applied perpendicular to the sample's surface. A current between 10^{-8} A and 10^{-2} A is used, depending on the conductivity of the sample.

Little literature has been published on determining the charge carrier density of C12A7:2e- by Hall effect measurements. Zhao et al. studied Sr-doped electrides and found charge carrier densities up to $2.13{\cdot}10^{21}\mathrm{cm}^{-3}$ [137]. No other characterisation technique was used for comparison. Waetzig et al. found charge carrier densities of $4.9{\cdot}10^{18}\mathrm{cm}^{-3}$ for their samples [126]. Accompanying thermogravimetric measurements indicated an degree of reduction corresponding to an electron density of $1{\cdot}10^{21}\mathrm{cm}^{-3}$, leading the authors to conclude that Hall effect measurements systematically underestimate the cage electron concentration because only mobile electrons can be detected by this method. This assumption was further studied by Dinter et al., who used temperature dependent measurements of the charge carrier densities and mobilities of a series of samples with different degrees of reduction to derive the transport model described above [18]. They found that Hall effect measurements are mainly sensitive to electrons propagating by hopping conduction due to the high mobility of this transport channel. As discussed above, the effective charge carrier density therefore differs in number from the total F^+ centres in the electride. A correlation is shown in Figure 2.3. When searching for the absolute F^+ centre density, i.e. the degree of reduction, of a sample, temperature dependent Hall and resistivity measurements have to be conducted to extract effective carrier densities and mobility values. Only in conjunction with modelling, estimates for the F^+ centre density can be given.

In this work, Hall effect measurements are used as one of the reference methods to compare with other material characterisation techniques. An overview of the values obtained for the different samples is therefore given in Table 2.1 and comparisons to other techniques in the following sections.

2.4.2 Full and Partial Oxidation Technique

The electride C12A7:2e- re-oxidises to C12A7:O^{2-} in a high temperature, oxygen rich atmosphere. The incorporation of oxygen during this process results in a higher mass density of C12A7:O^{2-}. The relative weight difference between C12A7:O^{2-} and completely reduced C12A7:2e- is 1.17%.

[3] In this work, platinum is chosen as the contact material due to its availability in the laboratory.

Name	n_{eff} [cm^{-3}]
B1	$3.3 \cdot 10^{18}$
B2	$2.62 \cdot 10^{19}$
B3	$3.06 \cdot 10^{19}$
B4	$4.5 \cdot 10^{18}$
B5	$6.2 \cdot 10^{18}$
B6	$9.1 \cdot 10^{20}$
B7	$7.5 \cdot 10^{19}$
B8	$2.3 \cdot 10^{19}$
S11	$8.38 \cdot 10^{20}$

(a) Produced by ATD

Name	n_{eff} [cm^{-3}]
F4-03	$2.95 \cdot 10^{19}$
F4-04	$9 \cdot 10^{19}$
F4-11	$6.15 \cdot 10^{19}$
F4-13	–
F4-19	$2.6 \cdot 10^{20}$
F4-22	$7.05 \cdot 10^{19}$
F4-26	$9.78 \cdot 10^{20}$

(b) Produced by IKTS

Table 2.1: Effective charge carrier densities derived from Hall effect measurements.

This weight gain can be used to deduce the degree of reduction δ of a given sample by comparing the weight gain achieved at complete oxidation $\Delta m = m_{Ox} - m_0$ of the studied sample with the maximum weight gain that would occur for a fully reduced sample $\Delta M = 1.17\% \cdot m_0$.

$$\delta_0 = \frac{\Delta m}{\Delta M} = \frac{m_{\text{Ox}} - m_0}{0.0117 m_0} \tag{2.11}$$

with the initial sample mass m_0 and the mass after oxidation m_{Ox}. This technique allows an accurate determination of the degree of reduction of a sample. However, as it requires oxidation of the given sample, this destructive technique is not applicable to the in-situ analysis of C12A7:2e-electride samples as required for various applications. For oxidation, the samples are heated to 700 °C in vacuum. They are then exposed to an oxygen partial pressure of 0.1 mbar for 10 minutes. By maintaining the temperature without oxygen flow for additional 10 minutes a homogeneous reaction is achieved [139]. The difference in weight before and after oxidation is determined using a Sartorius Supermicro scale (sensitivity 0.1 µg). Based on the measured weight gain, sample E-S4 has a reduction degree of $\delta = 0.236$, which translates to a cage electron density of $5.5 \cdot 10^{20} \text{cm}^{-3}$.

Attention has to be paid to the oxygen species incorporated into the cages during the process. In addition to O^{2-}, other oxygen radicals such as O_2^{2-} or O_2^- may be bound in the cages [19, 132] and invalidate the estimate of O^{2-} incorporation based on the weight change. With a Raman spectrum of the oxidised sample such molecular oxygen radicals can be identified (more details on this technique are given in Section 2.4.4). The Raman spectrum of the oxidised C12A7 sample, shown in Figure 2.5a, shows no sign of O_2^-.

Identifying O_2^{2-} is more difficult since the corresponding Raman band at 771 cm^{-1} overlaps with a framework vibration band at 772 cm^{-1} [53]. However, an approximation with a Gaussian function fits the data well and does not require the assumption of a second mode. Furthermore, procedures described in the literature on the formation of oxygen radicals in C12A7 all require very high temperatures at high oxygen partial pressures of 0.2 atm to 1 atm to achieve significant ratios of oxygen radicals in C12A7. For example, in Ref. 132 an oxygen partial pressure of 1 atm, a temperature of 700 °C, and a process time of 1 hour resulted in less than 5% radicals in C12A7[4]. A significant deviation of the estimated degree of reduction due to the incorporation of other oxygen radicals can therefore be excluded in our samples, given the low oxygen partial pressure and the short process time.

A similar procedure can be used to obtain a series of samples with a range of degrees of reduction. An electride sample is cut into several pieces. One piece is completely oxidised. From the resulting weight difference, the degree of reduction of the original sample is calculated as described above. The other parts of this sample are partially oxidised using shorter exposure times to the oxygen atmosphere compared to complete oxidation. The degree of reduction of the resulting samples δ_i is calculated from the weight gain during this process $\Delta m_i = m_i - m_0$ and the degree of reduction of the base material δ_0

$$\delta_i = \delta_0 - \frac{\Delta m_i}{\Delta M} = \delta_0 - \frac{m_i - m_0}{0.0017 m_0}. \tag{2.12}$$

A schematic illustration of this process is shown in Figure 2.6. In this work, a series of four samples with cage electron densities ranging from $1.9{\cdot}10^{20} cm^{-3}$ to $5e{\cdot}10^{20} cm^{-3}$ is used. The calculated electron densities are given in Table 2.2. Such a sample series is valuable to study the effects of the degree of reduction on other material parameters. The synthesis of low electron density electride samples is limited by the control accuracy of the process time. As reported in Ref. 139, the degree of reduction decreases linearly with time, i.e. low degrees of reduction can be achieved in a small time frame only. However, lower process temperatures can extend this narrow time frame [139][5]. The latency of the actual setup

[4] Using Ref. 132, Fig. 9 where for 700 °C process temperature (1 hour) a spin concentration of O_2^{2-} and O^- of about $5{\cdot}10^{19} cm^{-3}$ is measured. Each O^{2-} in the cage must be replaced by two radicals to maintain charge neutrality. The spin density of O^{2-} without radicals would be $1.16{\cdot}10^{21} cm^{-3}$ (2 spins per unit cell of size $(1.198\,nm)^3$). So with a single charged radical concentration of $5{\cdot}10^{19} cm^{-3}$, $1.135{\cdot}10^{21} cm^{-3}$ O^{2-} remain in the cages, i.e. 95.8% of all cage species.

[5] No further experiments were performed in this case as the oxygen atmosphere together with the high temperature severely damaged the heater used.

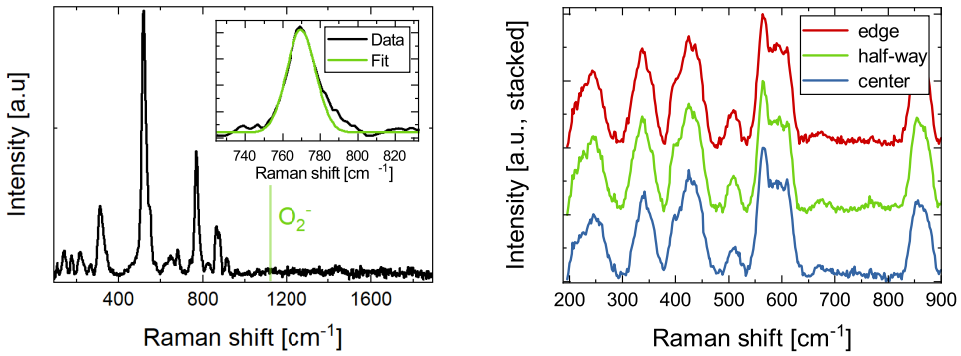

Figure 2.5: Raman spectra of (partially) oxidised C12A7 samples: a) Raman spectrum of a fully oxidised C12A7 sample. No peak is visible around 1128 cm^{-1}, which would be typical for O_2^- [53]. The band around 770 cm^{-1} can also be described by a single Gaussian peak (see inset). O_2^{2-} would lead to a second feature there [19]. More details on other aspects of the spectrum are given in Section 2.4.4. b) Raman spectra taken at different positions on the cut face of a partially oxidised C12A7:2e- sample.

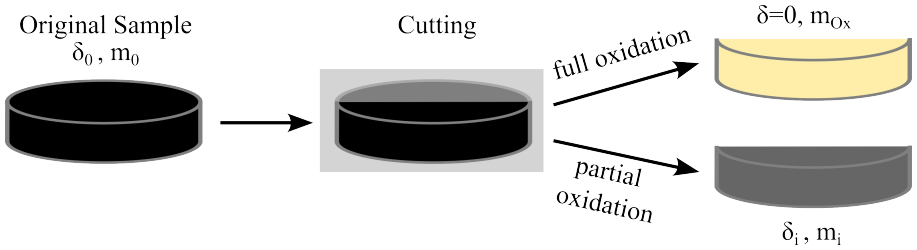

Figure 2.6: Schematic illustration of the oxidation technique: The original sample is cut into several slices. One of the slices is completely oxidised. From the increase in weight $m_{Ox} - m_0$ the degree of reduction of the original sample δ_0 can be calculated. The other slices are partially oxidised. From the weight gain during this process $m_i - m_0$ together with the degree of reduction of the initial sample, the degree of reduction of the resulting sample δ_i can be calculated.

only allows degrees of reduction above $\delta = 0.05$. To study both the bulk and the surface of the partially oxidised sample series during subsequent characterisation, the samples are cut in half. Raman spectra taken at different positions along the cut facet show a good spatial homogeneity of the degree of reduction, as shown in Figure 2.5b for sample E-S4-06. The maximum deviation to be expected in the degree of reduction is about 15%[6].

Name	δ_i	n_e [cm^{-3}]
E-S4-03	0	0
E-S4-04	0.08	$1.9 \cdot 10^{20}$
E-S4-05	0.159	$3.7 \cdot 10^{20}$
E-S4-06	0.206	$4.8 \cdot 10^{20}$
E-S4-07	0.214	$5 \cdot 10^{20}$
E-S4-14	0.236	$5.5 \cdot 10^{20}$

Table 2.2: Degrees of reduction and the corresponding cage electron densities derived from weight change during (partial) oxidation. The sample series is shown on the right: E-S4-03, the leftmost sample is fully oxidised, E-S4-04 to -07 (from left to right) are partially oxidised, and E-S4-14 is a pristine slice of the E-S4 sample (the rightmost sample).

2.4.3 Electron Spin Resonance Spectroscopy

An electron can be in different quantum states with respect to its angular momentum $\vec{J}$, characterised by its magnetic quantum numbers m_l and m_S. In the presence of an external magnetic field $\vec{B}$, these degenerate states split. In the ideal case the energy gap is given by [28 p.540, 61 p.399, 101 p.61]

$$\Delta E = g\mu_B \vec{B} \cdot \vec{J} \tag{2.13}$$

with the Bohr magneton μ_B and the *g-factor* which relates the angular momentum in units of $\hbar$ to the magnetic moment generated $\vec{\mu} = g\mu_B \vec{J} = g\frac{e\hbar}{2m_e}\vec{J}$ [101 p.61]. When this system is exposed to electromagnetic radiation of this energy, resonant absorption occurs. This effect is called *Electron Spin Resonance* or *Electron Paramagnetic Resonance*. In the case of electrons bound to a crystal lattice, this energy is modified by various interactions with the nucleus and the lattice [28 p.540]. For example, the position of resonant absorption, determined by the g-factor, is altered from

[6]For samples 04 and 14, the relative STDs between the peak area ratios are 11.9% and 14.9%, respectively. Assuming the linear relationship between peak area ratio and the F^+ centre density found in Chapter 2.4.5, the given value is estimated.

the value $g = 2.0023$ of a free electron by spin-orbit coupling of the electron or by local electrostatic potentials of neighbouring atoms [28 p.540, 101 p.68]. Coupling with the magnetic moment of the nucleus can add a hyperfine structure to the spectrum. Anisotropy of the unit cell can broaden the resonance line: If multiple crystallographic orientations are present in the sample, the angular momentum in each region will have different orientations with respect to the external magnetic field and the resulting spectrum will be a superposition of the individual orientations [28 p. 545]. However, it is this interaction of the electrons with their surroundings that allows many of these material properties to be measured by ESR. The magnetic permeability can be determined, i.e., whether a sample is paramagnetic or diamagnetic. By correlating the resonance energy with the external magnetic field, the g-factor can be deduced [101], which provides information about structures and energy levels. The number of unpaired spins can also be measured. This is done by comparing the integral of the absorption spectrum with that of a reference sample [28 p. 548].

A special case of ESR spectroscopy is the analysis of F^+ centres. These are crystallographic defects in which an electron is bound to an anion defect site. The unpaired spin of this electron can be detected by ESR spectroscopy. Unlike electrons bound to a specific atom, the electron bound to the vacancy interacts with all the surrounding atoms. These are usually the nearest neighbours and the next nearest neighbours [61 p.412, 28 p.544, 556]. Due to the large number of interactions, the resonance line is broadened. Several models exist for the electron wave function in such a vacancy. Good results, depending on the application, have been obtained for the *particle in a box* model and the *Linear Combination of Atomic Orbitals (LCAO) approximation* [61 p.412, 28 p.57, 564]. In the LCAO approximation the electron wave function is an equal superposition of the electron wave functions of the nearest neighbours. The consideration of p-type orbitals is thereby important for a good representation of the F^+ centre electron [28 p.564, 568].

In the special case of C12A7:2e- electride, the F^+ centres are the oxygen vacancies in the cages of the lattice. While C12A7:O^{2-} shows only a weak resonance signal at $g = 2.01$ [39, 58, 68, 135], for C12A7:2e- electride a much stronger resonance is measured with a g-factor of $g = 1.994$ [57, 58, 59, 74, 135]. Several reports by Li et. al. have found g values up to $g = 1.998$ [66, 67, 68]. The peak-to-peak half-width varies with the degree of reduction and the temperature [18]. Although ESR is sensitive to the cage electron states, significant discrepancies are reported when comparing the obtained spin density with the cage electron density estimated by

absorption spectroscopy [67, 74, 126, 129] or thermogravimetry [126, 67]. Most reports only mention an underestimation of the cage electron density for samples above $1{\cdot}10^{19}\mathrm{cm}^{-3}$ electron density [74]. However, Dinter et al. also report an overestimation for samples below this cage electron density when compared to the charge carrier density obtained from Hall effect measurements [18]. There are two reasons for this discrepancy. First, ESR has different sensitivities for the different cage electron species discussed in Section 2.2. Main contributor to the spin resonance are electrons in a delocalised state [18]. These are only a fraction of the total cage electrons as shown in the Figure 2.3. Whether the other electron species are not measurable by ESR or simply have a low signal strength remains uncertain. Second, in samples with high electron concentrations, antiparallel spin coupling between neighbours becomes more likely, especially since the $S = 0$ state is the most energetically favourable [109]. The resulting diamagnetic electron pairs or bipolarons reduce the measured effective spin [74]. This effect has also been measured for other crystals with colour centres, where these coupled vacancies have been termed *M centres* [28 p.548].

To study the electron spin resonance of C12A7:2e- electride samples in the scope of this work, a *Bruker ESP 900E* spectrometer operating at room temperature is used. Field modulation and lock-in techniques were employed. The derivative of the recorded absorption signals is approximated by the following function [97]

$$f(B) = A_0 \cos(\phi) \cdot \frac{(\sigma^2 - (B - B_r)^2)\tan(\phi) - 2\sigma(B - B_r)}{(\sigma^2 + (B - B_r)^2)^2} \tag{2.14}$$

where A_0 is an experimental factor, σ is the half-width of the signal, ϕ describes the asymmetry due to the Dyson effect, and B_r is the magnetic field strength at which resonance occurs for a given wavelength of the incident radiation. The intensity of the absorption is determined by the total number of unpaired spins in the sample. By post-referencing the spectrum's integral to a specimen of known spin concentration, the spin density can be determined. In the context of this work, weak pitch with a spin concentration of $5 \cdot 10^{19}\,\mathrm{spins/cm}^{-3}$[7] is used. An alternative is $CuSO_4{\cdot}5H_2O$ [59]. It is assumed, that the measurement system has the same sensitivity for the F^+ centre spin states in the C12A7:2e- electride as it has for the spin states in the weak pitch.

Bulk samples with high spin concentration, i.e., high electrical conductivity, show asymmetric line shapes. An example for an electride sample

[7] The spin density of this weak pitch reference was measured in the context of Ref. 99. This work in turn used standard carbon reference samples.

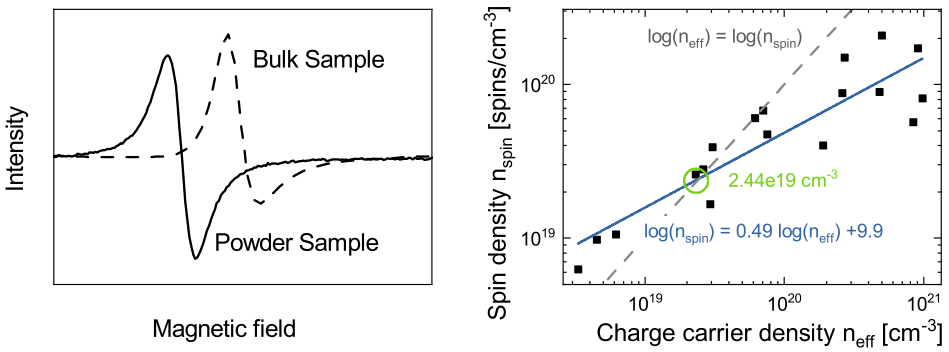

Figure 2.7: ESR signal of C12A7:2e- samples: a) In the case of highly conductive samples, the resonance spectrum of a bulk sample shows an asymmetric, Dysonian line shape. This behaviour disappears when the sample is ground to powder. b) Correlation of the spin density with the effective charge carrier density. These two properties correlate with the approximated linear equation (in double-exponential representation) shown at the top. For comparison, also the case of an identity is shown as a dashed line with the intersection at $2.44 \cdot 10^{19}\ cm^{-3}$.

with an electrical conductivity of $\sigma = 271\,\mathrm{S/cm}$ is shown in Figure 2.7a. In the case of a bulk sample the maximum and minimum of the signal differ significantly in intensity. This so-called Dysonian line shape has also been reported for other C12A7:2e- samples with high electron concentration [66, 74]. Due to the reduced skin depth in electrically well conducting samples, the microwaves used penetrate only into a thin layer at the surface of the studied specimen. Grinding the samples into fine powder with grain sizes corresponding to the penetration depth avoids this effect [135], as it can be seen for the sample shown.

The C12A7:2e- samples measured in this work show a single resonance peak with a g value of 1.994. This value is identical to that of other electride samples reported in the literature. In total, the spin densities of 18 different C12A7:2e- samples are determined. These samples possess spin densities ranging from $6.27 \cdot 10^{18}\,\mathrm{spins/cm^{-3}}$ to $1.72 \cdot 10^{20}\,\mathrm{spins/cm^{-3}}$. Figure 2.7b shows the correlation of the spin density (from ESR) with the effective charge carrier density obtained from Hall effect measurements. It is clearly visible that the two properties correlate. However, the two methods do not give identical values for their respective densities. Instead, they correlate with an exponent of 0.49, as shown by the linear fit line in the figure. Above a value of $2.44{\cdot}10^{19}\mathrm{cm^{-3}}$ the effective charge carrier density exceeds the spin density. Below, less charge carriers than spins are de-

tected. This shows that the two techniques differ in their sensitivity to the different electron populations of C12A7:2e-. A detailed discussion of this topic is given in Section 2.4.5.

2.4.4 Raman Spectroscopy

Fundamentals

In a crystal structure, atoms can vibrate with respect to their equilibrium positions. In the context of the whole lattice, these vibrations can propagate as waves through the crystal. The vibrational behaviour is essentially determined by the bonds to neighbouring atoms, which can be described by a spring force constant. The resulting vibrational modes can be distinguished by the atomic displacements they induce: If the displacement is in the direction of propagation, the vibrations are called *longitudinal*. If the displacement is perpendicular, the vibration is called *transversal* [101]. Mixed polarisations may also occur [48]. Furthermore, in the case of more than one atom in the primitive cell, the vibrational modes differ in terms of the relative motion of the atoms. In the *acoustic mode*, all atoms in the primitive cell vibrate in phase, whereas in the *optical mode* the atoms do not vibrate in phase. The optical modes, also called optical branches, exhibit a low dispersion compared to the acoustic branches [48]. In total, a three-dimensional crystal structure containing N atoms in its primitive cell shows $3N$ different vibrational modes, 3 acoustic and $3N - 3$ optical branches [62]. The excitation of these lattice vibrations can be regarded as quasi-particles, the *phonons*.

To study the phonons of a material, *photon-phonon interaction* can be used. When a photon probes a crystal structure, its electric field $\vec{E}$ affects the electrons of the crystal atoms and induces a polarisation $\vec{P}$. The relationship between the polarisation and the inducing electric field is described by the electric susceptibility χ of the crystal

$$\vec{P} = \chi \varepsilon_0 \vec{E}. \tag{2.15}$$

The electric susceptibility can change with the (thermal) vibration of the atoms in the crystal [133]. This modulation can be approximated in powers of the underlying vibration $\vec{Q}$ by

$$\chi = \chi_0 + \left(\frac{\partial \chi}{\partial \vec{Q}}\right)_0 \vec{Q} + ... = \chi_0 + \chi_1 \vec{Q}. \tag{2.16}$$

Applied to the polarisation of the crystal lattice, this results in two components of the polarisation. An undisturbed component due to the incident

photon $\vec{P}_0$ and a varying polarisation due to lattice vibrations $\vec{P}_1$. Assuming $\vec{Q}$ as a plane wave $\vec{Q}(t) = \vec{Q}_0 \cos(\omega_0 t)$ and the electric field due to the incident photon as $\vec{E}(t) = \vec{E}_0 \cos(\omega t)$, we get for $\vec{P}_1$

$$\vec{P}_1 = \frac{1}{2}\varepsilon_0 \chi_1 \vec{Q}_0 \vec{E}_0 \left[\cos\left((\omega + \omega_0)t\right) + \cos\left((\omega - \omega_0)t\right)\right]. \tag{2.17}$$

A detailed derivation can be found in Ref. 133 p.375. It can be seen that this polarisation term is described by two waves shifted from the original frequency by the frequency of the lattice vibration involved in the interaction [122, 133]. At these frequencies photons can be re-emitted [62]. In a simplified way, this interaction can be described as the inelastic scattering of a photon at a phonon of the crystal lattice [101]. If a phonon is created, a photon with a lower frequency is emitted, called *Stokes process*, if a phonon is annihilated, a photon with a higher frequency is emitted, called *anti-Stokes process* [62]. The frequency difference between the incident light and the re-emitted light is called *Raman shift*. In the case of acoustic phonons the process is called *Brillouin scattering*, for optical phonons *Raman scattering* [17, 101]. However, not all phonon modes are Raman active. As can be seen from the Equations 2.16 and 2.17 the following condition must be fulfilled for Raman scattering to occur:

$$\chi_1 = \left(\frac{\partial \chi}{\partial \vec{Q}}\right)_0 \neq 0 \tag{2.18}$$

This means that the electric susceptibility has to change during the vibration [48, 101, 122]. In this case a vibrational mode is called *Raman active* [122]. Taking the example of an iodine molecule I_2, the polarisability is a function of the atomic distance between the two atoms. Thus, the stretching vibration which varies the distance between the two iodine atoms is Raman active [105, 63].

The Raman spectrum of C12A7 in its oxidised form is dominated by two peaks at $521\,\mathrm{cm}^{-1}$ and $772\,\mathrm{cm}^{-1}$ [53, 78, 119]. Weaker features are also reported between $180\,\mathrm{cm}^{-1}$ and $400\,\mathrm{cm}^{-1}$. An assignment of Raman signals to specific lattice vibrations in the crystal is challenging due to a large size of the unit cell consisting of 116 atoms plus in its oxidised form two cage oxygen, which results in 354 possible vibrational phonon branches (not all Raman active and some due to the cubic symmetry degenerated). Different approaches are therefore taken to describe the Raman response of C12A7: A simple approach is to calculate the vibration frequency from the bonding strength of the respective atom to the neighbouring atoms and the atomic masses. In this picture, the peak at $521\,\mathrm{cm}^{-1}$ is assigned to the motion of the bridging O(1) between two aluminium atoms and the peak

at 772 cm^{-1} to an Al-O stretching mode [78]. Bands around 300 cm^{-1} are assigned to vibrations involving calcium [119] Another method is based on the aluminium tetrahedra that constitute the framework. Assuming the tetrahedra in the crystal structure vibrate similarly to their isolated configuration but in a different crystal field, the characteristic vibrational frequencies are somewhat comparable. The peak at 521 cm^{-1} is assigned to the ν_1 mode ('breathing mode'), the peak at 772 cm^{-1} is assigned to the ν_3 mode [119]. However, this approach does not consider the interaction between the different tetrahedra and the other elements of the unit cell. Ref. 47 uses finite displacement methods to compute a phonon DOS (density of states) of the material. According to this study the two phonon bands around 560 cm^{-1} and 830 cm^{-1} originate from aluminium and oxygen vibrations, the third band below 450 cm^{-1} involves calcium and oxygen. Factor group analysis and isotopic substitution allow for a more detailed insight into the origin of Raman signals. The involved atomic species and their crystallographic positions may be identified by this approach [53]. In this study both dominant peaks, at 521 cm^{-1} and 772 cm^{-1}, are assigned to the vibrational modes of Al(1) with O(1) or O(2).

Systematic Raman spectroscopy of electride samples has so far only been performed on one set of electride glasses [55]. Characteristic broad bands were found at 186 cm^{-1}, 430 cm^{-1}, 560 cm^{-1} and 780 cm^{-1}. Except for the 780 cm^{-1} feature, which was attributed to the stretching mode of Al-O in AlO_4 tetrahedra, the intensities of all modes varied with the electron concentration of the electride glass. In particular, the sharp band at 186 cm^{-1}, which becomes distinguishable for electron concentrations above $3.5 \cdot 10^{20} cm^{-3}$, was attributed to vibrations of electrons trapped in cages. It has to be emphasised that these results were obtained for a quenched C12A7:2e- melt in which no regular crystal structure could form. Therefore, these results can hardly be applied to the commonly used polycrystalline sinter material. Spectra for such crystal structures have been shown in Refs. 56, 93, 135, but have not been systematically discussed until now.

Raman Spectroscopy of C12A7 electride

In this work, a systematic study of C12A7:2e- is performed by Raman spectroscopy. A total of 35 samples are studied: 15 samples produced by ATD and 17 samples synthesised by IKTS. All samples are sintered powder samples, i.e. polycrystalline. Raman measurements are performed at room temperature using a Renishaw in Via Raman spectrometer combined with a Leica optical microscope system in a backscattering geometry. The majority of the measurements use a 532 nm diode laser as the exci-

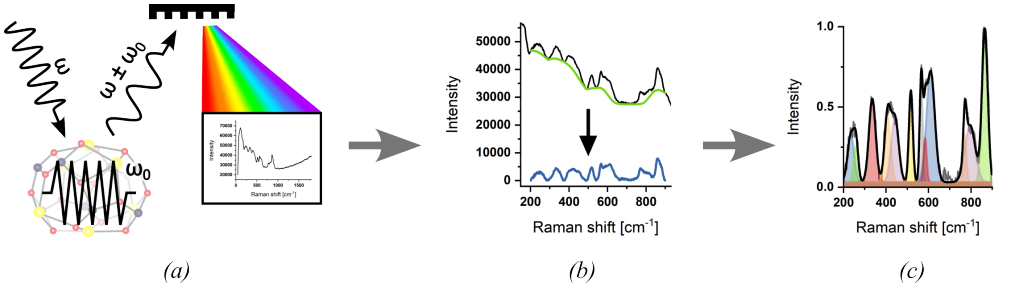

(a) (b) (c)

Figure 2.8: Schematic of the data acquisition and processing chain for Raman spectroscopy: a) The sample is excited by a laser of the frequency ω. The frequency of the Raman-scattered light is shifted due to inelastic scattering of the laser photons with a phonon of the crystal lattice of the frequency ω_0. By analysing the scattered light with a spectrometer, a Raman spectrum is obtained that displays intensity versus frequency shifts. b) The spectrum is then background-corrected and normalised to the [0,1]-range. c) All peaks are fitted with a Gaussian function for further analysis.

tation source. For the oxidation series[8] an Ar-ion laser with a wavelength of 515 nm is used, due to the availability in the laboratory. Reports on the relative peak intensities in C12A7:2e- spectra for different laser wavelengths showed only deviations of about 2% in this wavelength range [55], so this difference is considered negligible. The laser operates at a power of a few milliwatts and the diameter of the laser spot on the sample is approximately 1 µm. To focus the laser light onto the sample and to collect the scattered light a 50× objective is used. The collected light is dispersed by a diffraction grating in the spectro"-meter and then focused onto a CCD detector. As part of the post-processing of the acquired spectra, a background is subtracted with the *EstimatedBackground* function in *Wolfram Mathematica*[9]. For a better comparability, the spectra are then normalised to the $[0, 1]$-range. Phonon signals in the spectrum are approximated with Gaussian type peaks. Peak positions and intensities are extracted from these fits. A schematic illustration of the measurement and data processing steps is shown in Figure 2.8.

The homogeneity of the studied samples is verified by taking several Raman spectra at different positions. The homogeneity varies greatly between samples of different manufacturers. The samples supplied by ATD show very uniform Raman spectra over the entire surface. Only negligible differences are observed between different measurement points. In contrast, the Raman spectra of the samples supplied by IKTS have a very different appearance depending on the spatial position of the measurement. This is

[8] and the first samples from IKTS, which are not included in the subsequent analysis
[9] The corresponding code can be found in the Appendix of this work

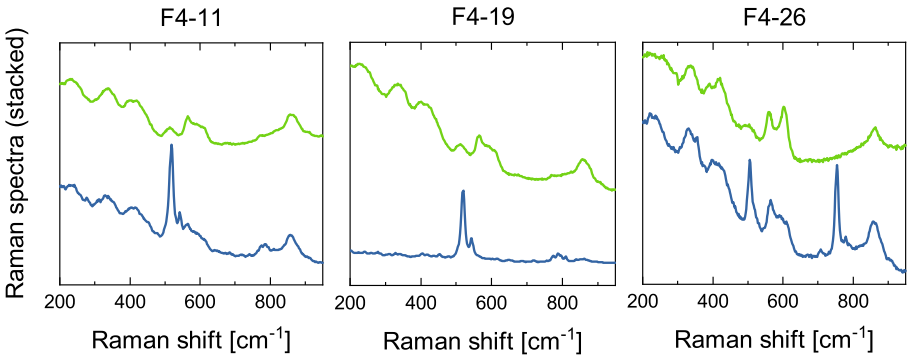

Figure 2.9: Raman spectra of IKTS samples show significant variation between different positions on the sample surface. For three samples, spectra recorded at two different positions are shown as an example. Notably, the region between 500 cm^{-1} and 650 cm^{-1} that is characteristic of C12A7:2e- differs significantly for different spots on each sample. Furthermore, in the blue spectra of the samples, peaks attributed to secondary calcium aluminate phases are found: At 543 cm^{-1} (CA) for F4-11 and F4-19 and at 753 cm^{-1} (C3A) for F4-26.

illustrated in Figure 2.9, which features Raman spectra of three samples. Different bands dominate the spectra at different positions. In particular, the region between 500 cm^{-1} and 650 cm^{-1}, which is indicative of the degree of reduction of C12A7 (as discussed later in this section), differs significantly for different spots on the sample. In the bottom (blue) spectra, the region is dominated by a single peak at 521 cm^{-1}, which is characteristic of C12A7:O^{2-}. In the upper (green) spectrum, a broad band around 600 cm^{-1} is visible, indicative of C12A7:2e-. This spatial variation depends on the sample studied, either encompassing the entire range of degrees of reduction up to fully oxidised sites or just signifying distinct states of C12A7:2e- electride. However, this finding demonstrates, that Raman spectroscopy can resolve locally different degrees of reduction in C12A7:2e- samples. There is also evidence of non-C12A7 calcium aluminate phases in the blue spectra in the figure: The spectra for F4-11 and F4-19 show an additional feature at 543 cm^{-1}, which is indicative of CA [119]. In the lower spectrum of F4-26 a peak at 753 cm^{-1} indicates the presence of C3A [119].

Selected spectra of C12A7 samples are shown in Figure 2.10, sorted by their effective charge carrier density as determined by Hall effect measurements or by the reduction degree determined by the weight gain technique. The most prominent Raman bands in these spectra, together with the position of their maxima, are summarised in Table 2.3. The Raman spectrum of the fully oxidised sample (bottom spectrum) is in very good agreement with the literature, showing two strong peaks at 521 cm^{-1} and

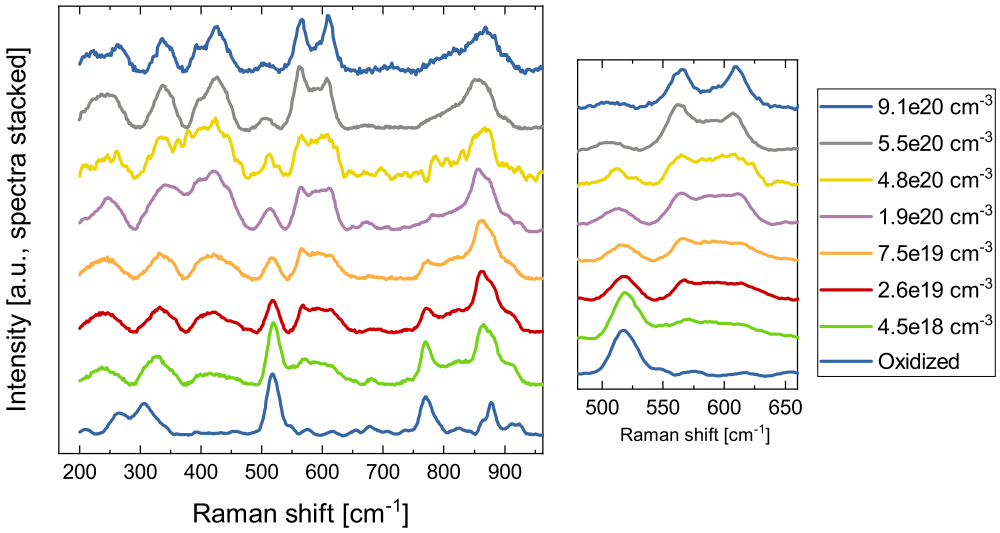

Figure 2.10: Raman spectra of C12A7:2e- electride samples with different degrees of reduction. The spectra are sorted according to the electron density/ effective charge carrier density of the sample, measured by the weight gain technique ($n_e = 1.9{\cdot}10^{20}\,cm^{-3}$, $n_e = 4.8{\cdot}10^{20}\,cm^{-3}$ and $n_e = 5.5{\cdot}10^{20}\,cm^{-3}$) or Hall effect technique (other spectra): The lowest spectrum shows a fully oxidised sample, the sample in the top spectrum has a charge carrier density of $9{\cdot}10^{20}\,cm^{-3}$. A detailed view of the region around $550\,cm^{-1}$ is shown on the right. The spectra have been background subtracted and intensity normalised.

772 cm^{-1} Raman shift and other minor features. For high electron concentration samples (top spectra) a band around 600 cm^{-1} with two distinct maxima at 566 cm^{-1} and 610 cm^{-1} Raman shift dominates the spectrum. A peak deconvolution of the band indicates that a third mode around 565 cm^{-1} is also hidden in the band. Across all spectra there is a systematic evolution of certain peaks from the oxidised state to samples with a high cage electron density. With increasing electron density the peaks at 521 cm^{-1} and 772 cm^{-1} Raman shift diminish. While a small feature at 521 cm^{-1} Raman shift is also measured for highly reduced samples, the 772 cm^{-1} Raman peak disappears above an effective charge carrier density of $n_{eff} = 2{\cdot}10^{20}cm^{-3}$. In contrast, the double peak around 600 cm^{-1} is present in every electride spectrum examined. Just a broad band for lower electron concentrations, the two peaks become distinguishable above $3{\cdot}10^{20}cm^{-3}$ electron concentration. The Raman bands in the region below 400 cm^{-1} also change and become three distinguishable peaks (details on peak positions given in Table 2.3).

In addition to the intensity of certain peaks, the position of the peak around 520 cm^{-1} also changes with the electron density. This trend is lin-

position [cm^{-1}]	species	trend	attribution [53, 89]
244	e		
264	o		asymmetric vibr. of Ca around cage center
306	o		expansion AlO_4, contraction of neighbours
338	e		
422	e		
521	b	decr.	symmetric stretching of AlO_4
566	e	incr.	
589	?		vibration of Al or O in framework
610	e	incr.	
772	b	decr.	asymmetric stretching of AlO_4
878	b		expansion AlO_4, contraction of neighbours

*Table 2.3: Overview of vibrational modes obtained from Raman spectra of C12A7 samples. The position of the maximum, the C12A7 species (**o**xide, **e**lectride or **b**oth), the evolution of the peak's intensity with increasing electron concentration n_{eff} and an attribution according to the literature is given.*

ear to the square root of the electron density and is shown in Figure 2.11a. For the oxidised state a peak position of $521\,cm^{-1}$ is extrapolated, which is in agreement with the values reported in the literature. With increasing electron density the peak moves to lower Raman shifts. At the theoretical maximum electron density the trend predicts a peak position of $494\,cm^{-1}$. A peak position dependent on electron density or doping level has also been reported for other semiconductors [10]. In addition to the position of the peak, its width also changes with a significance of over 1.5σ, increasing on average from about $22\,cm^{-1}$ to $25\,cm^{-1}$ as shown in Figure 2.11b. For the other peaks that change in intensity with electron density at $566\,cm^{-1}$, $610\,cm^{-1}$ and $772\,cm^{-1}$, a shift of their position may also occur, but no clear assessment can be made from the given data.

Based on these observations, conclusions can be drawn about the origin of the respective Raman modes. Since the intensity of the $521\,cm^{-1}$ mode scales with the carrier density, which in turn is related to the degree of reduction, i.e., the removal of cage oxygen, the mode must be related to changes that occur during this process. Based on experiments investigating other oxygen species in C12A7, vibrations of the oxygen in its cage can be excluded as origin of this mode. When the cage anion O^{2-} is gradually replaced by O_2^- or O_2^{2-}, Raman spectroscopy shows changes in the

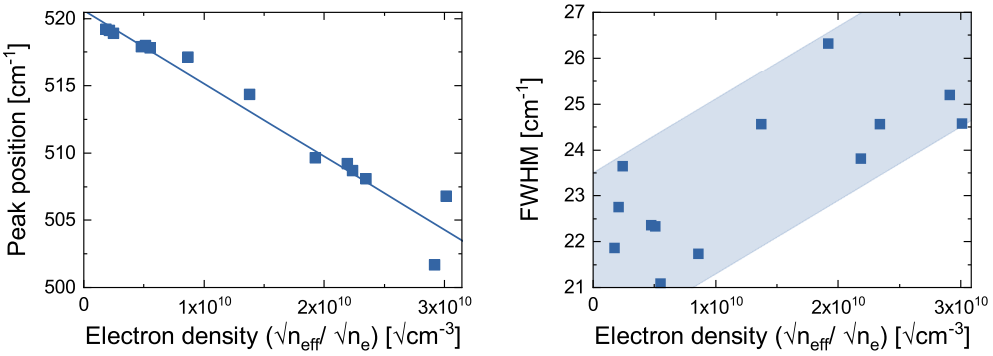

(a) *(b)*

Figure 2.11: Development of the 521 cm^{-1} peak with the square root of the electron density. a) Peak position: A systematic shift to lower wavelength can be observed. b) Full width half maximum of the peak: the width of the peak increases with electron density.

intensity of the molecular vibrations of these molecules, but no change in the 521 cm^{-1} mode is observed [19, 132]. If the cage oxygen itself were responsible for this mode, a change in intensity would be expected upon replacement by other oxygen species. The 521 cm^{-1} mode is therefore rather related to the cage deformation caused by the incorporated oxygen, as described in Section 2.1. In addition to the two calcium atoms, an aluminium atom is involved in the coordination of the cage oxygen and is also displaced from its original position. Together with the knowledge that the peak at 521 cm^{-1} has been attributed in the literature to stretching modes of oxygen in an aluminium tetrahedron [53], the peak at 521 cm^{-1} can be attributed to vibrations in this specific aluminium tetrahedron. It has also been reported that the 521 cm^{-1} peak shifts with the bond angle over the bridging oxygen [78]. This report is in good agreement with the observed peak shift with the degree of reduction, as the cage deformation decreases with increasing cage electron concentration. The increased band width in this case would be due to a superposition of the band at 521 cm^{-1} originating from the remaining cages containing oxygen with the signal at 494 cm^{-1} from the electron-containing cages. The question left unanswered by this discussion concerns the similarity between electron-containing cages and empty cages, particularly in view of the converging cage diameter [60]. In this case, empty cages should have a similar Raman spectrum to electron-containing cages. As 10 of the 12 cages in a C12A7 unit cell are empty even in the oxidised state, their Raman signal should also be visible. However, the double peak around 600 cm^{-1} only appears for the electride form of C12A7. The origin of this band is still unclear.

For the mode at 772 cm^{-1} a similar reasoning as for the 521 cm^{-1} mode can be applied: The intensity decreases with the degree of reduction and has also been reported to belong to an aluminium tetrahedron. This peak is therefore attributed to another vibrational mode of the same aluminium tetrahedron.

Analysis of the peak area correlation

As shown in the previous section, the intensity of both the peak at 521 cm^{-1} and the double peak around 600 cm^{-1} changes with electron density. To study this relationship quantitatively, the peak area ratio Λ is introduced. It is determined from the Gaussian fitted Raman peaks of C12A7:2e- samples

$$\Lambda = \frac{A_{566} + A_{589} + A_{610}}{A_{521}}. \tag{2.19}$$

The indices used refer to the approximate peak position as the center of the peak may shift slightly with the degree of reduction. The correlation of this ratio with the cage electron density (weight gain technique) or the effective charge carrier density (Hall effect measurement) can then be studied. As there are significant discrepancies between the Hall measurements performed by IKTS and those conducted in this study, only samples whose electron density was measured in-house with the setup described in Section 2.4.1 are used in establishing the correlation described in the following. This excludes ten samples produced by IKTS. For the other samples, an average of the peak area ratios obtained at different positions is used. In the case of the samples produced by IKTS, the spatial inhomogeneities described above resulted in large uncertainties for both the effective charge carrier density and the peak area ratio. Figure 2.12 shows the peak area ratio Λ with respect to the cage electron density (weight gain technique) and the effective charge carrier density (Hall effect measurement). It is clear that the peak area ratio correlates with both the cage electron density and the charge carrier density. The trend is also independent of the manufacturer: While the spatial inhomogeneities observed in the IKTS samples show large uncertainties, the samples still follow the same trend as the ATD samples. The overall trend is best represented by a square root function ($R^2 = 0.91$).

The results presented in this section show that Raman spectra of C12A7 samples provide useful information about the material's crystallographic and electronic structure. Not only can secondary calcium aluminate phases and different incorporated oxygen species be distinguished, the Raman spectra provide also detailed information about the degree of reduction of

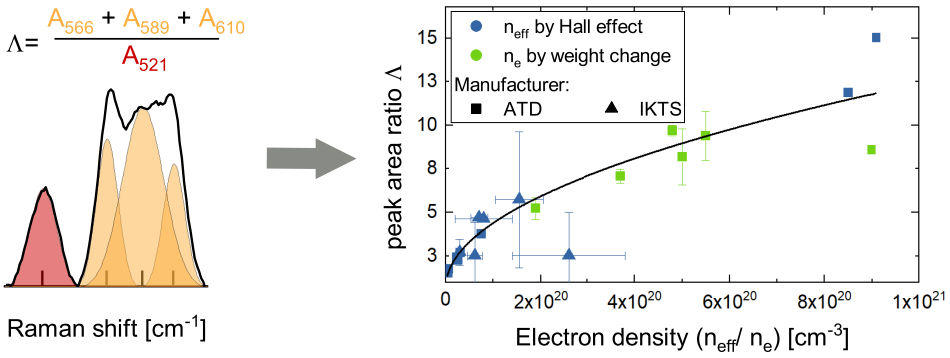

Figure 2.12: Peak area ratio Λ according to Equation 2.19 with respect to the electron density obtained by other characterisation techniques. A visual representation of the peak area ratio is shown on the left. The electron density was obtained either by the Hall effect technique (blue) or by the weight gain technique (green). The shape of the markers indicates the manufacturer of the sample: squares for ATD, triangles for IKTS. The trend line shown is a fit based on a square root function.

a C12A7:2e- sample and give an indication of the microscopic processes taking place in the crystal. Several bands have been identified in the spectrum which change with the degree of reduction of the electride and allow a first assessment of the quality of a given sample. The peak area ratio introduced in this work is therefore a useful technique to provide a quantitative estimate of the electron density of a sample based on its Raman spectrum.

2.4.5 Summary

In this study, a variety of characterisation techniques was applied to C12A7:2e- samples of different degrees of reduction. Correlations between ESR and Raman spectroscopy and the two reference techniques were investigated. Both the spin density obtained by ESR spectroscopy and the peak area ratio obtained from Raman spectra were found to correlate with the effective charge carrier density and the degree of reduction measured during controlled oxidation. This demonstrates that both ESR and Raman spectroscopy can be used to assess the degree of reduction of a C12A7:2e- sample.

As explained in Section 2.2, it should be noted that neither the Hall effect technique nor the ESR directly measures the total amount of cage electrons in the electride. Instead, each technique is sensitive to a different population of electrons. However, the results presented above can be correlated with the actual degree of reduction of C12A7, represented by the density

of F^+ centres, by modelling of the transport data. Figure 2.13a provides an overview of this correlation. Interestingly, the effective charge carrier density obtained by the Hall effect technique does not vary linearly with the F^+ centre density, but instead shows an increasing slope with increasing F^+ centre density, i.e. as the number of cage electrons increases, a larger proportion of electrons contribute to the charge transport. The reason for this behaviour is not fully understood, but may be explained by the lower hopping activation energy [18] as the electrons approach the metallic state, where the electrons are best described by a free electron gas. Using the three-band model introduced in Ref. 18 and extended in this work to express directly the correlation of the different charge carrier populations with the F^+ centre density n_F, see Appendix A.1, the following relation is obtained for the hopping carrier density

$$n_{\mathrm{Hop}}(n_F) = \left(-9.72 + 0.5\,\log\left(\frac{n_F}{\mathrm{cm}^{-3}}\right)\right) n_F \exp\left(-\frac{\left(1.09\,\mathrm{eV} - 0.052\,\mathrm{eV}\log\left(\frac{n_F}{\mathrm{cm}^{-3}}\right)\right)\cdot e}{k_B T}\right). \tag{2.20}$$

As it can be seen in Figure 2.13a, this model describes the measured values for the effective charge carrier density quite well. Furthermore, in the studied F^+ centre density range, the model can be very well approximated by a parabola. The deviation between the three band model and the parabola simplification is shown in Figure 2.13b. The absolute deviation is more than an order of magnitude smaller than the respective values and therefore this approximation is appropriate for the given range. This finding is supported by Ref. 75. Here the free charge carriers (also determined by Hall effect measurements) correlate to the power of 1.5 with the electron density. Both parameters were determined by a Drude-Lorentz model from absorption spectra, where the total electron density was referenced to ESR spin densities.

In the case of the spin density, a linear relationship is expected since there is one unpaired spin per F^+ centre. This behaviour was also reported by Ref. 74. However, in the mentioned reference the experimentally determined spin density deviates from this linear relationship at about $1\cdot10^{19}\,\mathrm{spins/cm}^{-3}$ and is said to saturate due to anti-parallel spin coupling. This observation could not be reproduced in the present work. Even considering the smaller range of degrees of reduction of the samples in this work compared to the given reference, a saturation would be visible. On the contrary, the measured data rather follows the trend of the low reduction degree samples presented in Ref. 74. More samples in the high F^+ centre density region would be required to investigate a possible saturation due to the increased probability of spin pairing. Also for the spin

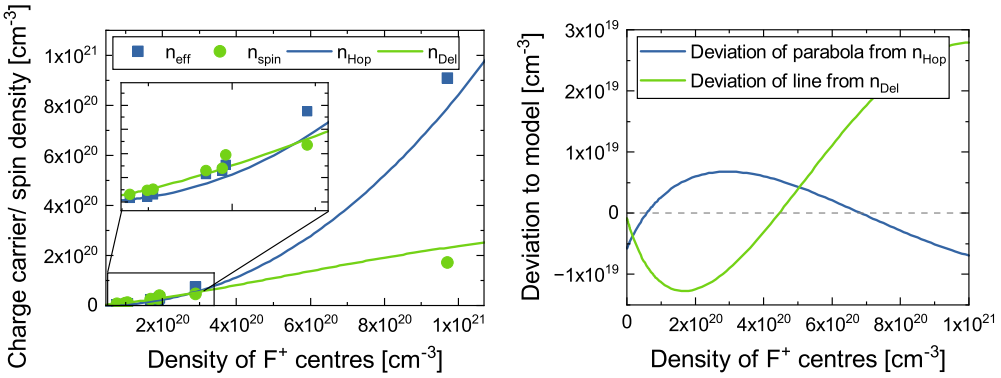

Figure 2.13: a) Correlation of the F^+ centre density according to Ref. 18 with the carrier density n_{eff} from the Hall effect technique (blue squares) and the spin density n_{spin} from ESR spectroscopy (green circles) for C12A7:2e- samples. In addition, the predictions of the three-band model for the hopping and delocalised charge carrier densities are shown as lines. b) Deviation between the three-band model and the approximation by a parabola (in the case of n_{Hop}) and a line (in the case of n_{Del}), respectively.

density the three band model can be used to predict the development with increasing F^+ centre density. The following relationship is obtained

$$n_{\mathrm{Del}}(n_F) = \left(10.72 - 0.5\,\log\left(\frac{n_F}{\mathrm{cm}^{-3}}\right)\right) n_F \exp\left(-\frac{\left(1.09\,\mathrm{eV} - 0.052\,\mathrm{eV}\log\left(\frac{n_F}{\mathrm{cm}^{-3}}\right)\right)\cdot e}{k_B T}\right). \tag{2.21}$$

The trend of the measured data points is well modelled by this relationship, as it can be seen in Figure 2.13a. In first approximation the model is well described by a line. The small deviations are shown in Figure 2.13b. The square root relationship observed for the spin density with the charge carrier density, as shown in Figure 2.7, can be explained by these approximations: the parabolic trend of n_{eff} with the total number of F^+ centres together with the linear trend of n_{spin} with the F^+ centre density leads to the observed square root correlation of n_{spin} with n_{eff}.

Raman spectroscopy was used as another technique to obtain information about the electride. As described in Section 2.4.4, certain peaks were found to correlate with the charge carrier density. The peak area ratio was introduced to quantify this behaviour. The obtained peak area ratio values with their associated F^+ centre densities are shown in Figure 2.14. It can be seen that there is a significant correlation between the peak area ratio and the F^+ centre density. The correlation is well described by a linear trend. The evolution of the relevant peaks for the peak area ratio

was partly explained by the cage relaxation that occurs when the cage oxygen is replaced by two electrons. To the author's knowledge, no exact relationship between the cage diameter and the degree of reduction has been published to date. However, the data obtained in this work suggest that the cage deformation may be linearly dependent on the degree of reduction, since the peak area ratio shows a linear correlation with the F^+ centre density. As already discussed for the spin density, the observed square root relationship between the peak area ratio and the charge carrier density, as shown in Figure 2.12, can be explained by the parabolic trend of n_{eff} with the F^+ centre density in conjunction with the linear evolution of the peak area ratio.

The peak area ratio also allows an assessment of the oxidation technique which was used to determine the degree of reduction of C12A7:2e- samples. Two sets of samples, one with a known F^+ centre density and one with a known degree of reduction calculated from the oxidation technique, are compared using the peak area ratio, which was determined for both sets of samples. As it can be seen in Figure 2.14, both densities are of a similar order of magnitude and show the same global trend but differ slightly in value. This could be attributed to the accumulated uncertainties in analysing both the peak area ratio and the F^+ centre density. Also a systematic underestimation of the degree of reduction by the oxidation technique cannot be excluded. Nevertheless, this demonstrates that controlled oxidation with accompanying weight gain measurement is a viable technique for assessing the degree of reduction of a C12A7:2e- sample.

This meta-analysis demonstrates that each characterization technique is sensitive to other parameters of C12A7:2e- electride. A comprehensive understanding of material properties and their development with the degree of reduction demands a combination of these insights.

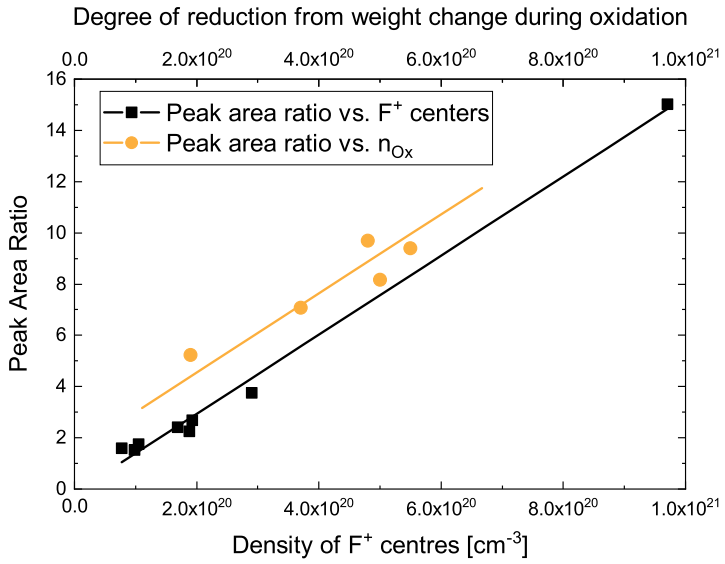

Figure 2.14: Analysis of the correlation between the peak area ratio and the density of F^+ centres (represented by black squares with a linear trend line) and the degree of reduction determined from the weight gain resulting from controlled oxidation (represented by yellow circles with a linear trend line). As there is no direct correlation data available for F^+ density and the weight gain technique, the two techniques are compared using the peak area ratio for the corresponding samples. It is evident that the values acquired through controlled oxidation demonstrate a comparable tendency with respect to the peak area ratio as the F^+ centre density.

Chapter 3

Cathodes with C12A7:2e- inserts

The most common thruster designs, the *gridded ion engine* (GIE) and the *Hall effect thruster* (HET) both rely on an additional electron emitting unit as part of the corresponding propulsion system, the so called *cathode*. Whereas some GIE, like inductively coupled thrusters, only require an external electron supply for the ignition of the plasma inside the thruster, HET and other GIE, like Kaufman-type thrusters, also require the cathode during operation to maintain their plasma discharge. Both types share the fact, that only positively charged ions are extracted from the thruster into the plume. Additional electrons for plume neutralization are therefore required to prevent an accumulation of negative charge on the spacecraft. This chapter provides a brief introduction to the theoretical aspects of cathodes. In the following, two different cathode design concepts and the corresponding test campaigns are presented.

Just as the areas of application vary, so do the requirements for space cathodes. The extraction current of the cathodes depends on the thruster concept. It ranges from a few milliamperes to several amperes for high-power electric propulsion systems. For thrusters that require an additional electron supply for their plasma discharge, about the fivefold to tenfold amount of the extraction current is additionally required for plasma generation [27, 33]. One therefore distinguishes between *discharge cathodes* and *neutralizing cathodes*. Regardless of the amount of extraction current, a high power efficiency is required. Furthermore, conventional satellite systems demand a high reliability and a lifetime in the range of several 10 000 hours [14]. In contrast, the very cost-conscious new-space market accepts a lower reliability of their systems in return for a high cost-efficiency.

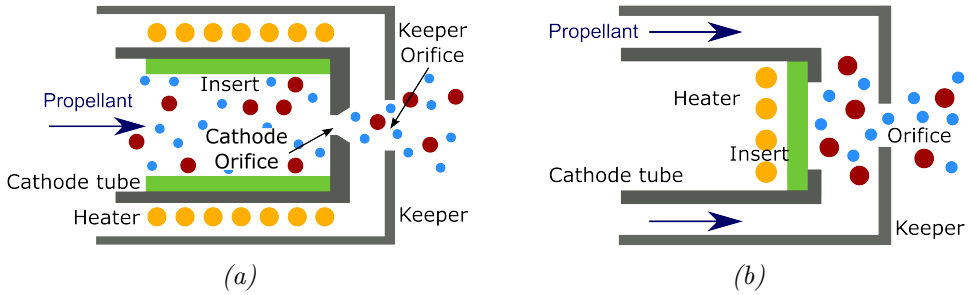

Figure 3.1: Schematic view of two thermionic cathode designs: The insert is contained by the cathode tube. Heat is supplied by the heater to ignite a plasma inside of the cathode. The cathode structure is surrounded by the keeper. Orifices confine the plasma and allow extraction.

3.1 Previous Work on Cathodes

Various design concepts have been developed to emit electrons into free space. The simplest is a heated filament, usually made of a refractory metal. Its elevated temperature releases electrons by thermionic emission, as described by the Richardson-Dushman-equation

$$J = AT^2 \cdot \mathrm{e}^{-\frac{\Phi}{k_B T}} \tag{3.1}$$

with the material specific *Richardson constant* A and the work function of the material Φ [14, 16]. However, such designs require very high temperatures and suffer from a high evaporation rate of the filament and a strong space charge limitation [33, 94]. Plasma cathodes avoid space charge limitations by creating a so-called *plasma bridge* between the cathode and the anode [9]. Common designs are inductively coupled plasma cathodes (mostly called RF-cathodes) and thermionic plasma cathodes. RF-cathodes can produce currents in the range of 100 mA to 3.5 A, but suffer a low power efficiency below 10^{-2} A/W [124]. Thermionic plasma cathodes are the most efficient design with a power efficiency up to 0.7 A/W and can reach currents of over 100 A [32]. Therefore, thermionic plasma cathodes are the common choice for electric propulsion systems.
A thermionic plasma cathode uses the thermionic electron emission of an emitter material, the so-called *insert*. The released electrons collide with the propellant atoms and ignite the plasma. Since the emitter materials exhibit work functions in the range of 2.0 eV to 2.67 eV [14, 35, 115], additional thermal energy is used to overcome the potential barrier given by the work function of the material. A *heater* is used to raise the emitter temperature to the desired value. During operation, the insert is then (additionally) heated by the plasma. To establish electrical contact with the insert, the *cathode tube* houses the insert. On the downstream side, the gas

flow is inhibited by the *cathode orifice* to increase the neutral gas pressure in the emitter region. Most designs employ a *keeper* with its own orifice further downstream. The keeper stabilises the plasma, especially in case of fluctuations of the coupled thruster plume, and protects the cathode below from sputtering [33]. Two generic thermionic cathode designs are shown in Figure 3.1: One with a cylindrical, the other with a planar emitter.

Thermionic plasma cathodes use a plasma to enhance electron extraction from the emitter material, to heat the insert and to enable higher extraction currents [9]. The plasma environment, however, strongly depends on the domain inside the cathode. Three different plasma regions are distinguished: First, the insert region, upstream of the cathode orifice; second, the orifice region within the channel of the cathode orifice; and third, the plume downstream of the cathode orifice.

The insert region plasma is characterized by a high neutral gas density, due to the cathode orifice staunching the gas flow. The result is a collisional plasma [33], slowing down back-streaming ions from the orifice and inhibiting high energy sputtering of the insert. Plasma parameters are thereby significantly influenced by the cathode's geometry, in particular the ratio of the orifice diameter to the insert's inner diameter. Typical plasma densities for the plasma in the insert region are in the range of $10^{19}\,\mathrm{m}^{-3}$ to $10^{21}\,\mathrm{m}^{-3}$ [31, 33, 65, 88] with low electron temperatures of 1.6 eV to 4 eV [29, 36, 80, 88]. With decreasing orifice size, the pressure gradient along the flow path increases, together with the plasma density [34]. The plasma has a smaller axial extension compared to plasmas in cathodes with larger orifices.

Where the plasma gets in contact with the surrounding walls, in particular in case of the insert, a plasma sheath establishes. This electron depleted region forms because otherwise, as the electron velocity exceeds the ion velocity, more electrons than ions would reach the wall in a given time interval, violating the quasi-neutrality condition of the plasma. Therefore, a potential difference establishes between the insert and the bulk plasma to impede the electron flow from the plasma to the wall. In addition, this electric field enhances the electron emission from the insert (field enhanced thermionic emission) and accelerates the emitted electrons into the plasma bulk. The sheath voltage adjusts to balance the incident electron current with the incident ion current and the current of the thermionic electrons leaving the surface. The total electron emission is either limited by the available thermionic emission current, depending on the insert temperature, or the opposed negative space charge, which is partly compensated

by plasma ions in the sheath. A 2D model for a cylindrical hollow cathode shows, that a significant amount of the thermally emitted electrons returns to the emitter and does not contribute to electron emission for the thruster due to space charge effects [80]. Due to the smaller axial extension of the plasma in cathodes with small orifices, the thermionic electron emission is limited to a smaller area of the insert. Thus, cathodes with smaller orifices are limited in their maximum current and are mostly used for low-current demands [33]. Besides electrons, also plasma ions are accelerated by the sheath potential, in this case towards the insert. Impacting ions can cause sputtering of the surface, leading to insert erosion in the long run. The extend of degradation depends on the sheath potential[1].

The particle incidence, i.e., electrons and ions, on the walls serves another important role: The temperature transport between the plasma and the surrounding structure of the device. Thermionic electrons convey heat from the insert into the plasma, whereas plasma ions and electrons heat the insert surface and the device structure. Further power input arises from scattering of electrons at heavy particles within the plasma, called *resistive heating*. The dominant heating mechanism in a cathode depends on the cathode geometry: For large orifices the cathode and the insert are primarily heated by ion bombardment in the insert region. For smaller orifices, the previously discussed shorter attachment length comes into play and less heat is deposited directly by the plasma into the insert. In this case, the dominant heat input arises from the orifice by heat conduction and radiation. Cathodes with small orifices experience therefore higher insert temperatures close to the cathode orifice. This has to be considered in the design phase to protect the emitter material from damage. The desired operation mode for space cathodes is reached when the plasma heating is sufficient to compensate the heat losses to the walls alone and an external heater is no longer needed. This mode is called the *self-sustained heating mode* [33].

Further downstream in the cathode, the plasma enters the orifice region regime. It is dominated by a high electron current density, since all electrons contributing to the extraction current have to pass this small aperture. The dominant heating in this region therefore also originates from the electrons, interacting with the heavy particles. Either they ionize neutral gas atoms or they are scattered causing the so called *plasma resistance* ranging from $0.3\,\Omega$ (large orifice) to $3.5\,\Omega$ (small orifice) along the orifice [33]. Depending on the orifice diameter, the generated heat is either

[1] For hollow cathodes, Ref. 33 reports the ion bombardment energy as low as 20 eV, which essentially precludes sputtering.

deposited at the walls or convected into the plume. Especially for small-diameter orifices, the ionization rate in the orifice region is significant due to the high neutral gas density [33]. This leads, on the one hand, to a high erosion rate, limiting the cathodes lifetime. On the other hand, also a high electron production is noted, which significantly enhances the resulting extraction current of the cathode.

In the class of thermionic plasma cathodes, the most common insert geometry is a hollow cylinder and the corresponding design is called *hollow cathode*. Hollow cathodes have the advantage of a good thermal confinement: The thermal losses from the plasma are mostly absorbed by the insert and maintain its operation temperature, leading to a high power efficiency. Also, the flow path of the propellant is comparably simple. However, hollow cylinders are considerably harder to machine than disks. Also, in hollow cathodes just a part of the emitter is effectively used as electron emitter and the plasma density varies along the emitter axis. Another design concept was developed in the 1990's by MIREA university in Moscow. Here, a planar insert design with a LaB6 pellet accompanied a SPT-100 Hall effect thruster and has since been used for laboratory testing of Hall effect thrusters [51, 103]. Experimental and numerical analysis have been performed for this type of cathode [52]. Applying a numerical model to this cathode and the NSTAR cathode revealed differences in plasma parameters between the cylindrical and the planar design, like in plasma and neutral gas density and in electron temperature [98]. However, this can presumably be explained by the different orifice sizes of the two cathodes. Considering hollow cathodes with a larger orifice, as shown in Ref. 33, distribution and magnitude of, i.e., the plasma density become more comparable. This assumption is supported by the simulations performed in Ref. 37, where a 0D model is applied to a hollow and a planar cathode with similar orifice diameters[2]. A major drawback of the planar design, which probably also prevented further development into a flight-capable cathode, were the significant heat losses to the cathode's outer wall [37]. This thermal energy did not contribute to heating the emitter, which is why continuous heating of the emitter during operation was required [52].

However, the planar design concept becomes relevant again for cathodes using C12A7:2e- as emitter material. Here, the advantage of thermal confinement of hollow cathodes turns into a disadvantage for the temperature-sensitive, poorly thermally conductive material. In hollow cathodes, melt-

[2] Attention has still to be paid, since a different insert material (LaB6 in the hollow cathode, C12A7:2e- in the planar cathode) and working gas (xenon vs. krypton) were used for the simulations shown in the respective report.

ing occurs frequently and destroys the insert [22, 76, 141]. Therefore, Drobny et al. tested a planar geometry without an external heater with promising results [20]. The device requires high mass flows of 20 sccm krypton and a high voltage for ignition. Nonetheless, almost 1000 hours of operation were reported so far with 2 A of extraction current. Also Airbus Defence and Space Friedrichshafen develops a planar insert design with a C12A7:2e- emitter, equipped with an external heater [124]. First ignition attempts with this design have been successful.

For electric propulsion systems today, the standard propellant is xenon. It has a decade-long flight heritage, a fairly low ionisation energy and is an inert gas. However, with an increasing number of satellites launched each year, and a more cost-sensitive space market, cost efficiency becomes a key decision criterion for electric propulsion systems. The price for xenon recently amounted to thousands of euros per kilogram. Besides the cost for the propellant itself, also the supporting periphery like the gas supply system has to be considered. Xenon requires a pressurised storage system and has a low storage density. Alternatives are therefore sought in more abundant elements. As it is desirable that the entire propulsion system runs on the same propellant, also the cathode accompanying the thruster has to be tested upon compatibility with the new propellant.

The noble gas krypton shares advantages of xenon, like its chemical inertness. However, krypton is thirteen time more abundant than xenon [86], resulting in about a quarter of the price [26, 114]. In addition, due to its similarity to xenon, existing propulsion system can be operated with krypton with only minor adaptations and do not require a complete redesign [23, 70, 91]. Yet, krypton has a higher ionization energy (14.0 eV vs. 12.1 eV [71]) and provides a lower mass per atom for thrust generation [124]. This xenon-krypton-efficiency-gap has been widely discussed for electric thrusters and extensive research has been performed to identify and overcome causes and to enhance operation efficiency with krypton [70]. Furthermore, test campaigns of an ion thruster and its cathode operating on krypton showed a higher erosion rate compared to xenon [91]. Despite this, krypton-fueled Hall effect thusters are used successfully in-flight on Starlink satellites. Testing hollow cathodes with krypton, Makela et al. reported that their cathode required higher anode potentials compared to operation with xenon [73]. The same was confirmed by numerical simulations [29, 92]. Also the initial breakdown voltage for ignition is elevated [1] and slightly higher insert temperatures were reported [29]. According to [1], the transition between the stable spot mode and the unstable plume mode shifts to lower mass flows for krypton. Besides that,

hollow cathodes can be operated both with krypton and xenon, without major differences in design and operation [92].

Another candidate as alternative propellant is iodine, which offers many advantages compared to xenon. It has a significantly larger ionization cross section [2, 96, 114], while also having a lower ionization potential (9.3 eV to 12.1 eV [71]). In addition, iodine normally occurs in its molecular state, leading to twice the atomic mass for thrust generation. Another notable advantage is its high storage density [42]. As a condensible propellant, iodine can be stored in solid form on the space craft and then vaporized with a small heating power when needed for operation. This eliminates the risks of a compressed gas tank [49] and allows a higher propellant mass budget, since the pressurized gas system can be spared[3]. But, a condensible propellant also carries the risk to condensate on other space craft surfaces (or in case of ground testing inside the test facility). This could impede the efficiency of solar panels or optical instruments or damage the space craft. The major disadvantage of iodine is its high chemical reactivity with many common materials, like aluminium, iron or titanium. Although, Zschaetzsch et al. stated, that propulsion typical iodine exposure and corrosion do not impede the structural integrity of the exposed materials [140], an iodine specific material selection should be made, when setting up a new thruster system.

Also for thermionic cathodes, material compatibility is an important issue. In particular, it is disputed which insert materials are compatible with iodine. Benavides et al. tried to ignite a cathode with a BaO-CaO-Al_2O_3 impregnated insert and iodine as propellant. No stable operation was achieved during these tests and a subsequent device inspection revealed a serious depletion of the emitter and deposition of emitter material on surrounding surfaces [4]. This behaviour was also confirmed in a pretest, where iodine was injected in the cathode without igniting a plasma. Tallifer et al. also used a barium oxide emitter to analyse the difference in plasma environment between the propellants iodine and xenon. He reported of a higher discharge and plasma potential for iodine compared to xenon operation [113]. Those were attributed to power losses due to molecular processes like dissociation and rotational excitation, as well as dissociative attachment of electrons. In a thorough plasma characterization also the reduction of the low energy electron population was noted and attributed to the previously described processes. The plasma density and electron temperature were slightly elevated for iodine [114]. The discharge

[3]This is according to Ref. 114 the main cost saving when using iodine, even though the propellant itself is also considerably cheaper than xenon [95]

was said to be stable for high discharge currents. However, no information was given on the actual operation time. A previous design by the same author failed to operate with iodine longer than a few minutes [113]. In another paper, a cathode from the same company, Busek, is described as having an operating time of over 50 hours with iodine [15]. Unfortunately, no first-hand information or further operational details can be found on this set of experiments.

For the other common emitter material, LaB6, less research has been performed on iodine compatibility. Szabo et al. reported that a hollow cathode with a LaB6 insert was operated over an hour with iodine, but no further detail was given [111]. To the contrary, no stable ignition could be achieved with a LaB6 emitter by the authors of Ref. 64. Positive results were reported for C12A7:2e- insert material. A cathode with a simplistic C12A7:2e- emitter was ignited heaterless with iodine. 20 hours of operation time were achieved without signs of degradation of the insert [96]. Hua et al. could maintain their discharge for up to twelve minutes, but were unable to extend operation time [46]. Instabilities in the gas supply system were suspected as the cause. An unstable gas breakdown was used to heat and clean the emitter surface prior to operation. Also in this case no iodine-related material degradation was observed.

The three reports of successful iodine operation above one hour operation time, namely Ref. 114 with BaO, Ref. 111 with LaB6 and Ref. 96 with C12A7:2e-, were all conducted within the iSat project: A NASA cubesat mission to demonstrate the flight-capability of a full-iodine propulsion system. The project was abandoned due to the immaturity of the propulsion system [49], in particular, due to the lack of a cathode, which fulfils the projects requirements of lifetime and discharge current [4]. It has therefore to be concluded, that subsequent to the above mentioned positive reports an unnamed obstacle prevented the flight readiness of the described cathodes. Flight experience with iodine is so far limited to the LunaH-Map mission with the BIT-3 ion thruster by Busek [72] and the NPT30-I2 thruster by ThrustMe [95]. Both systems do not use hollow cathodes for plume neutralization but an RF-cathode and a heated filament, respectively. Therefore, the development of an iodine compatible thermionic cathode is still an open research question. It is essential to make use of the advantages, which are promised by using iodine as propellant for electric propulsion systems. Thus, an iodine-only propulsion system is still to be developed. The most promising results are so far reported for C12A7:2e- emitters, as also concluded by Ref. 123.

3.2 Thermionic Planar Cathode

A thermionic plasma cathode utilises thermionic emission from an insert as a source of electrons for an electric propulsion system. This section introduces a novel design using a disk-shaped insert instead of a hollow cylinder. The planar geometry is beneficial for the challenging-to-machine C12A7:2e- material and enhances heat dissipation to mitigate insert melting. Lessons learned from the first design version are presented and used for an improved second design. The test procedure for the cathode operations presented in this section is illustrated below. Operation in diode mode allows for an analysis of the short and long-term stability of the device. A platinum grid coating of the insert is introduced to decrease stability issues. Operation in both diode and triode mode is presented and the performance in these two modes is evaluated. Successful operation of the thermionic planar cathode for several hours is achieved in triode mode. The section concludes with a discussion how the state of the insert used in the cathode impacts different operating parameters.

3.2.1 Design

The concept of a thermionic plasma cathode with a disk-shaped insert is particularly advantageous for C12A7:2e- electride as insert material. This section outlines the general design for version 1 of the design concept. An excerpt of the operations with this design is given, demonstrating the general functionality of the concept. However, a number of drawbacks are identified. The design is modified accordingly, yielding design version 2. The issue of insert fragmentation and measures for mitigation are described. An analysis of the effect of different cathode and keeper orifices concludes the section.

Design Version 1

The planar thermionic cathode design employs the same components as a classical hollow cathode. An insert is contained and electrically contacted by a cathode. A 25.4 mm (1 inch) diameter, 2 mm thick C12A7:2e- disk is used as the electron emitter. A commercial PG-PBN (pyrolytic graphite - pyrolytic boron nitride) heating element from ThermicEdge is placed underneath the insert to support ignition. The 1/8" diameter gas inlet is located at the rear of the neutraliser, which directs the gas flow around the internal cathode-insert assembly. The keeper surrounds the entire structure. The keeper orifice is made of graphite to reduce sputtering and can be exchanged to vary the orifice diameter. It has a conical opening which widens by a factor of three in the direction of flow. All orifice diameters

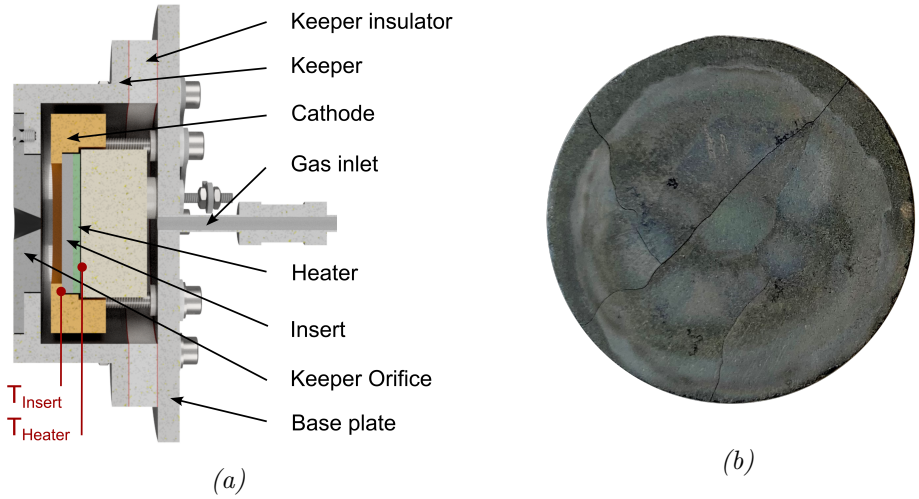

Figure 3.2: a) Cut view of the thermionic planar cathode's CAD model, b) Image of a fragmented insert.

given below are the minimum diameters. For the first design, an orifice of 2 mm to 6 mm was used. A schematic view of the first design is shown in Figure 3.2a. Two temperature sensors, type K thermocouples, are used in the design to allow close temperature monitoring. One temperature sensor is located at the rear side of the heater. The other one is mounted directly on the front face of the insert, which is particularly important for monitoring the insert temperature accurately during operation and for mitigating melting. However, due the low thermal conductivity of C12A7:2e-, the temperature at the centre of the insert is significantly higher (by about 100 °C) than at the edge, where the thermocouple is located. In addition, the sensor is in good thermal contact with the cathode body. This causes additional heat conduction from the insert to the cathode, reducing the local temperature at the sensor position. As a result of these two effects, the sensor underestimates the temperature of the insert's surface.

The planar cathode in design version 1 ignites reproducibly with the 1/8" diameter propellant supply line fully open, corresponding to over 60 sccm of xenon flow and a high voltage of 1200 V at an external ignition wire located some millimetres downstream of the keeper orifice. Discharge currents of up to 2 A are achieved with 1 A each for the keeper and anode, with a keeper voltage of 14 V to 16 V. However, the device only operated stably on short time scales of 25 to 50 seconds before instabilities terminated operation. During the testing of the design version 1, several design drawbacks were identified. Firstly, the heater contact pads deteriorate rapidly as a result of poor electrical contact between the heater contact pads and

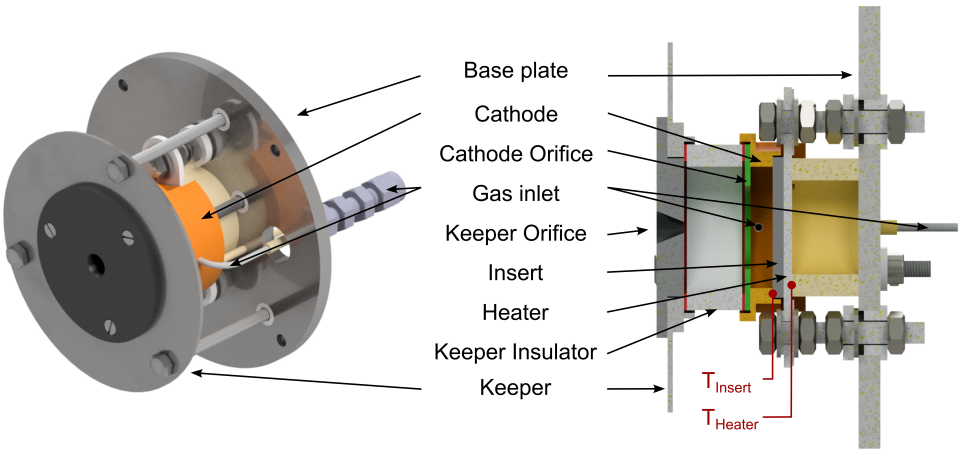

Figure 3.3: CAD model of the planar cathode design version 2 in isometric view (left hand side) and cut view (right hand side) with relevant design parts indicated. The positions of the two thermocouples are indicated in red.

the threaded rods. Secondly, the design requires high flow rates for operation due to an inefficient flow path around the central insert-cathode assembly. The internal pressure maximum is not located in front of the insert, but rather close to the keeper insulator. This also excludes the possibility of applying high voltages to the keeper, thus preventing ignition by the keeper. Instead, an additional ignition wire on the downstream side of the keeper is required for ignition.

Design Version 2

Design version 2 takes into account the issues identified in the earlier design. Figure 3.3 shows a schematic of the updated version. The keeper is now situated at a considerable distance from other conductive components, instead of enclosing the cathode assembly. This alteration prevents arcing between the keeper and the cathode body during the high voltage ignition phase. A boron nitride insulator located between the keeper and the cathode contributes to this improved design. Various lengths of this insulator are available for testing. However, only the 10 mm version was used for the tests presented in this work. In design version 2, two 1/16" tubes feed the propellant directly into the cathode chamber. These tubes are connected to the cathode by two lateral threads located opposite each other. Molybdenum, a well machinable material, is used therefore in design version 2 for the cathode instead of graphite as in the previous version. Cathode and keeper are both equipped with easily interchangeable orifices to study the effect of different orifice diameters. The keeper orifice is made

of graphite. The cathode orifice is made of graphite foil. Graphite material combines a high temperature tolerance with a high sputtering yield. Initial tests with a molybdenum cathode orifice revealed significant sputtering from the orifice onto the insert, therefore, this material was omitted. The external heater is exchanged for a model employing tabs, which yields a better electrical connection than the contact method used in version 1.

The electride disks used in the tests are 25.4 mm in diameter and only 2 mm thick. Combined with the low bending strength of C12A7 [126], mechanical stress along its radius can hardly be compensated by the material. Therefore, various measures are taken to reduce radial mechanical stress and angular gradients in contact pressure on the insert disk. First, a soft graphite foil is placed between the cathode and the insert. Second, a radial gap between the insert and the cathode accounts for the different thermal expansion coefficients of molybdenum and C12A7:2e-. Third, additional spring washers for mounting the keeper plate further decrease the contact pressure. By these measures, the fragmentation of the insert disk was significantly reduced, but not entirely eliminated. Figure 3.2b displays an image of a fragmented insert. No fragmentation was visible, when the plasma was not ignited, and the insert was only heated to ignition temperature and allowed to cool down afterwards. This suggests that thermal stress arises from the plasma in contact with the insert and the seemingly non-uniform heat input from it. Insert fragmentation can therefore be reduced by improving the plasma homogeneity in terms of time and lateral distribution. Nonetheless, moderately fragmented inserts can still be ignited and operated successfully, thus, insert fragmentation is not an operationally critical problem.

Orifice Diameters

Optimising plasma optics is a crucial yet intricate process in the development of thermionic cathodes. The cathode orifice influences the pressure gradient and the extension of the plasma along the insert, and thus the dominant insert heating mechanism and plasma density, as discussed in Section 3.1. The keeper orifice regulates gas and electron conductance of the cathode. The altered conductance impacts the ideal gas flow for stable operation and the resistive losses when extracting electron current via the anode [77]. Extensive research has been done to find the ideal geometry for different performance requirements in the case of hollow cathodes. For planar thermionic cathodes, however, no systematic study is published so far. Therefore, the knowledge of hollow cathodes has to be used to estimate the effect of different cathode and keeper orifice diameters. Although the

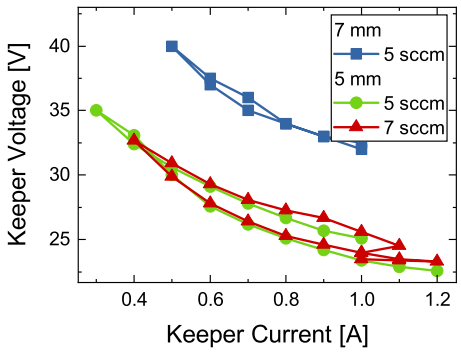

Figure 3.4: Performance of the planar cathode with a 5 mm cathode orifice compared to a 7 mm orifice. With a smaller orifice, a lower keeper voltage is required per keeper current. Contrary to operation with a 7 mm orifice, increasing the gas flow from 5 sccm to 7 sccm does not improve the performance.

plasma extends along the radial axis in planar cathodes, it is reasonable to assume that altering the cathode orifice diameter will have comparable impacts as in hollow cathodes. This also holds true for the keeper orifice, although in the standard configuration of the device the cathode-keeper distance of 11 mm is significantly longer than in typical hollow cathodes. A systematic study of the influence of different geometries must take into account the effects of insert wear, as discussed later, and the resulting systematic drift in device performance.

In the standard setup for the thermionic plasma cathode, the cathode orifice measures 7 millimetres and ignition occurs reliably. For $I_K = 1\,\mathrm{A}$, keeper voltages below 20 V are required (when the cathode operates with a pristine insert), as presented below. A smaller cathode orifice reduces the required keeper voltage significantly. In the case of a 5 mm cathode orifice the keeper voltages decreases to 25 V compared to 32 V with a 7 mm orifice, see Figure 3.4 (non-pristine insert, $I_K = 1\,\mathrm{A}$, $Q = 5\,\mathrm{sccm}$). In contrast, the absence of a cathode orifice, i.e., an orifice diameter of 22 mm, increases the required keeper voltage above the nominal range. Only thin DC-plasmas with high keeper voltages ($> 300\,\mathrm{V}$) and low currents ($< 40\,\mathrm{mA}$) can be maintained in this configuration. These results are in good agreement with the performance characterisation discussed in Section 3.2.3, where higher gas flows reduced the required keeper voltage at constant current. Evidently, increased internal gas pressures, or equivalently, higher neutral particle densities, lead to a decrease in the keeper voltage. Conversely, lower internal pressures significantly reduce the particle density and increase the required keeper voltage. An orifice to staunch the gas flow is

therefore required to operate the cathode at moderate keeper voltages. This can be achieved either through a cathode orifice or with a very short insert-keeper distance. In the latter case in the keeper orifice staunches the gas flow, as described in Ref. 20. Excessive reduction of the gas flow, on the other hand, does not enhance performance and may even lead to its decline. Increasing the internal pressure of the cathode by increasing the gas input from 5 sccm to 7 sccm does not notably change the performance in the case of the 5 mm orifice.

3.2.2 Test Procedure

The insert is the key element of any thermionic plasma cathode. The experiments described use C12A7:2e- inserts with a high electron concentration. The term *pristine insert* is used here to refer to inserts that have not been used in any previous test campaign, whose surface was cleaned before the test or which were flipped so that the former back-side (not previously used) is now the emitting surface. Inserts that do not meet these criteria are referred to as *non-pristine*.

The circuitry for testing the thermionic planar cathode is illustrated in Figure 3.5. The heater is powered by a *TTI CPX400* power supply (max. 60 V, 20 A). All other power supplies operate with respect to a common reference potential, known as the *SSG (secondary star ground)*. This potential usually differs from the facility ground. The keeper and the anode have a positive potential difference with respect to the SSG, described by the keeper voltage U_K and the anode voltage U_A. A *Keysight N6775A* power supply (max. 60 V, 5 A) is utilized as the keeper power source. For ignition, an additional power supply, a *GwInstek SPD-3606* (max. 120 V, 3 A when both channels are in series), is used to provide up to 120 V additional voltage. It is turned off afterwards. For the anode, a *FUG MCP 140-125* power supply (max. 125 V, 1 A) is used. An additional high voltage power supply, a *FUG MCN 750M-500* (max. 1500 V, 500 mA) can be used to support the creation of a plasma bridge between the cathode and the anode. To combine the two voltages and prevent damage or short circuits to the power supplies, a dedicated diode-box is used.

Prior to ignition, the insert is heated to increase thermionic electron emission. To achieve an even temperature distribution and prevent material stresses, a gentle ramp heating scheme is used, as shown in Figure 3.6a. During the final heating phase, external power of over 135 W is supplied. Due to inadequate thermal shielding of this laboratory model, this heating power is maintained during operation. The emission of electrons is

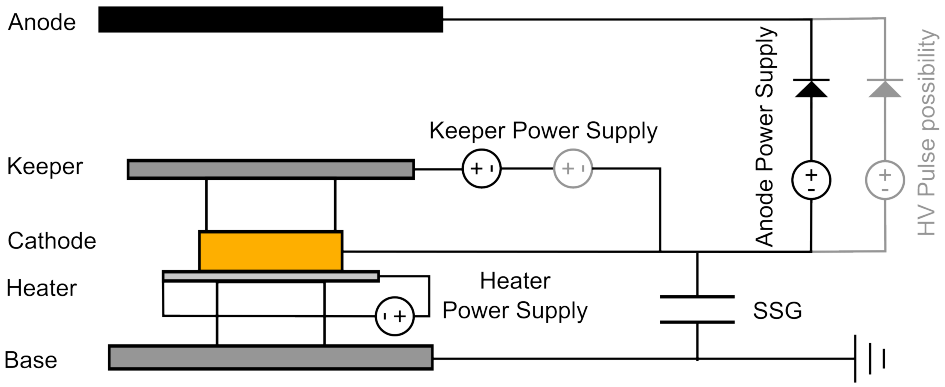

Figure 3.5: A schematic diagram of the circuit used to test the thermionic plasma cathode. The relevant cathode components are depicted on the left. The SSG (secondary star ground) functions as a common reference potential for the device, which usually differs from the facility ground. Auxiliary power supplies can be used for both the keeper and the anode during ignition to achieve higher voltages. Such optional power supplies are shown in grey. The heater has a separate circuit.

additionally enhanced by applying a voltage between the cathode and the keeper, the so-called *Schottky modification* Φ_S of the effective work function Φ by an electric field E [40, 41]

$$\Phi = \Phi_0 + \Phi_S = \Phi_0 - \sqrt{\frac{e^3 E}{4\pi\varepsilon_0}}. \tag{3.2}$$

The ignition voltage required depends on the wear of the insert, but is in the range of 60 V to 180 V. The cathode's plasma gets ignited by the thermionic electrons from the insert, which ionise the injected propellant. The applied voltage decreases rapidly, presumably due to the rise in insert temperature and the establishment of a plasma sheath between insert and plasma, that enhances the effective electric field for electron emission. Within a minute the voltage stabilises at an equilibrium voltage of 12 V to 19 V for pristine inserts. A typical voltage curve is presented in Figure 3.6b. For inserts that are not in pristine condition, the equilibrium voltage is generally higher, ranging from 18 V to 40 V in most tests. Sanding the surface of the insert before ignition significantly reduces this voltage (to 16 V from 24 V in a single case). Nevertheless, it remains slightly elevated compared to the original value of 12 V.

The power supply is operated in constant current mode in this case $I_K = 1$ A. This limit during the ignition process is essential for stable operation afterwards. According to the Richardson-Dushman formula (see Equa-

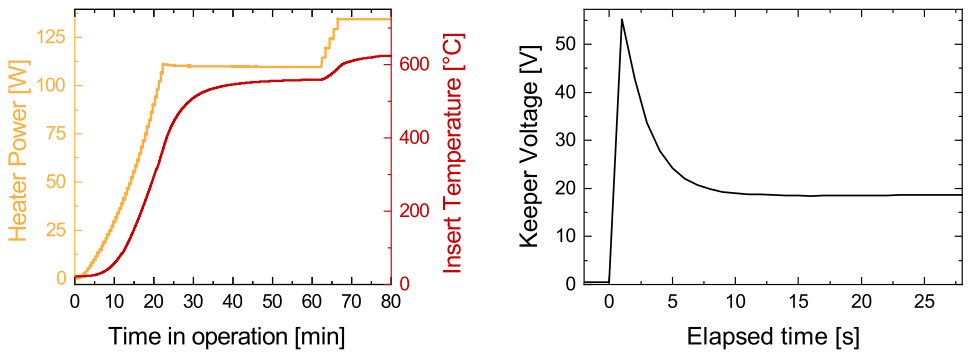

(a) (b)

Figure 3.6: a) The heating profile utilized for the external heater prior to ignition. b) The time profile of the keeper voltage after ignition, with the voltage rapidly declining to a value lower than that necessary for ignition.

tion 3.1) and the Schottky modification (Equation 3.2) the thermionic emission of the insert is limited by its temperature and the electric field at the surface of the insert. Both of which are low during the ignition stage, resulting in a low current delivered. In the presence of plasma, the temperature of the insert rapidly rises. The plasma also increases the electric field at the insert surface, due to the formation of a sheath. Additionally, the electrical conductivity of C12A7:2e- increases with temperature [138 p.32], resulting in an amplified electron supply from the bulk of the insert. Thus the discharge current can be increased after ignition. When higher extraction currents are demanded during the ignition process, a positive surface charge can accumulate (described in detail later in this section) and terminate operation. If plasma extinction occurs, it is generally necessary to regenerate the insert for an hour using a lower heating power of 110 W before re-ignition is possible.

3.2.3 Diode mode operation (keeper)

In diode mode, the plasma within the cathode is sustained by a current flow from the cathode to the keeper. This mode is useful for assessing general operation and the influence of various design parameters on the cathode. Operational stability in diode mode depends on the condition of the C12A7:2e- insert employed. Pristine inserts typically demonstrate high stability without significant variation, as demonstrated in Figure 3.7a. In contrast, inserts that are not in pristine condition may exhibit significant fluctuations or even hinder operation completely, depending on the insert's wear. Figure 3.7b illustrates an example of operation with a non-pristine

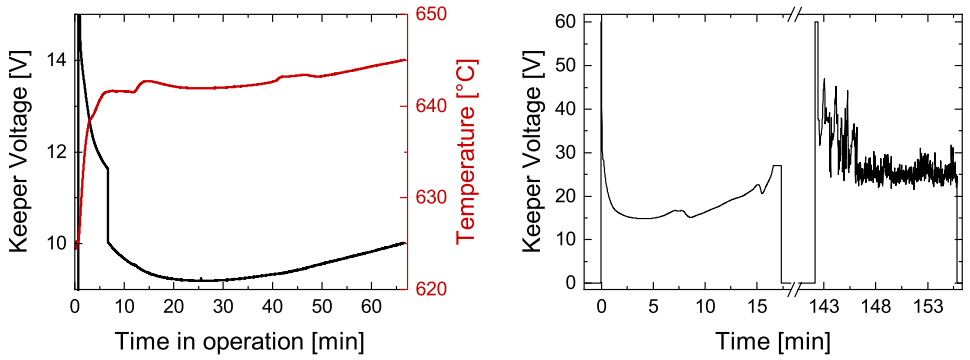

(a) (b)

Figure 3.7: Differences in operation of the planar cathode with pristine and non-pristine inserts. a) Representative cathode operation with a pristine insert, Q=5 sccm. For a constant keeper current of $I_K = 1$ A, a continuous drift of the keeper voltage is observed. Due to the increased power input, the insert temperature also increases. b) Cathode operation with a non-pristine insert (this test was conducted on the day following the run shown in a)), Q=5 sccm. During the first operation (0 min to 15 min), no oscillations were observed; however, the keeper voltage increased rapidly. Following a regeneration break, the cathode displayed extreme instability with significant fluctuations.

insert: The initial ignition attempt is successful and stable on short time scales, but the keeper voltage rises rapidly. The subsequent attempt, after a regeneration phase, oscillates strongly.

Given stable operation in constant current mode, in this case $I_K = 1\,\mathrm{A}$, the keeper voltage U_K exhibits a positive gradient for both pristine and non-pristine inserts. It can be distinguished between a permanent increase, where the keeper voltage remains elevated upon reignition of the cathode, and a temporary increase, i.e. the increase only occurs during a single test run and returns to its initial value after regeneration and reignition. At the current state of research, it is likely that a cathode with a pristine electride insert only faces a permanent increase in U_K during operation (assuming I_K is held constant). In this case, the increase can be determined directly from the time evolution of the keeper voltage during operation. Applied to the operation show in Figure 3.7a, an increase rate of about $0.03\,\mathrm{V/min}$ is determined, which is a typical range for the permanent increase rate. In the case of non-pristine inserts, the temporary increase (which will be discussed below) dominates the time evolution of U_K. The permanent increase is only apparent in the increasing equilibrium voltages after ignition over several test runs, which is illustrated in Figure 3.8.

In order to identify the origin of the permanent increase in keeper voltage,

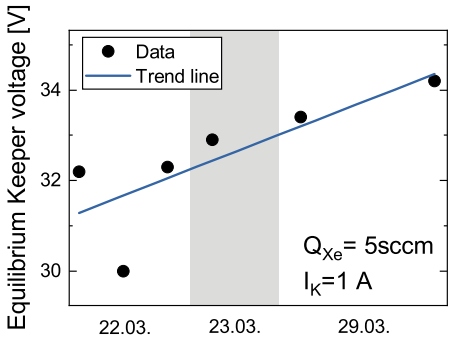

Figure 3.8: Equilibrium keeper voltage for operation with 1 A keeper current and 5 sccm xenon flow over several ignition cycles. A slight increase over the ignition cycles is observed, shown by the trend line. However, it is not significant when compared to the variance within a single test run.

the crystal structure of electride samples is studied. The electron emission characteristics of C12A7:2e- originate from the unique crystal structure of C12A7:O^{2-} calcium aluminate from which the cage oxygen is extracted leaving electrons behind. However, the presence of secondary calcium aluminate phases in the material reduces the number of sites available for binding electrons to the crystal, thus reducing the electron emission capability of the material. The pristine inserts studied in this work exhibit a pure C12A7:2e- phase composition, as measured by X-ray diffraction (XRD). No calcium aluminate phases other than C12A7:2e- are detected. Also the manufacturer ATD claims a 100% pure C12A7:2e- material [25]. Also, no significant signs of secondary calcium aluminate phases are found in an insert that was operated for over two hours with 1 A keeper current and 0.2 A anode current, neither by Raman spectroscopy nor by XRD. The corresponding diffraction pattern is shown in Figure 3.9a. All diffraction signals can be attributed to C12A7:2e-. Zschätzsch et al. reported the formation of secondary calcium aluminate phases during the operation of their hollow cathode with a C12A7:2e- insert over extended time periods. In particular, C3A and C5A3 were detected by Raman spectroscopy (and XRD, although not covered in the report) [138]. These secondary phases led to an increase in the keeper voltage, which ultimately terminated the operation. However, these secondary phases only started to occur at insert temperatures of 1000 °C [89, 138], which is significantly higher than the operating temperatures present in this work. Only an insert that underwent surface melting during operation shows a notable quantity of the C3A-phase, as illustrated in Figure 3.9b.

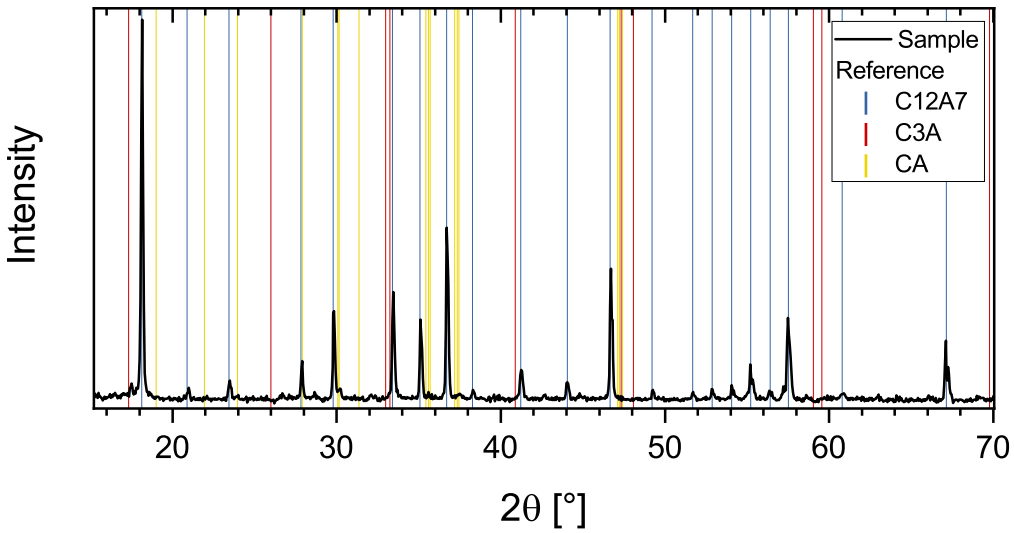

(a) after 2 hours of operation

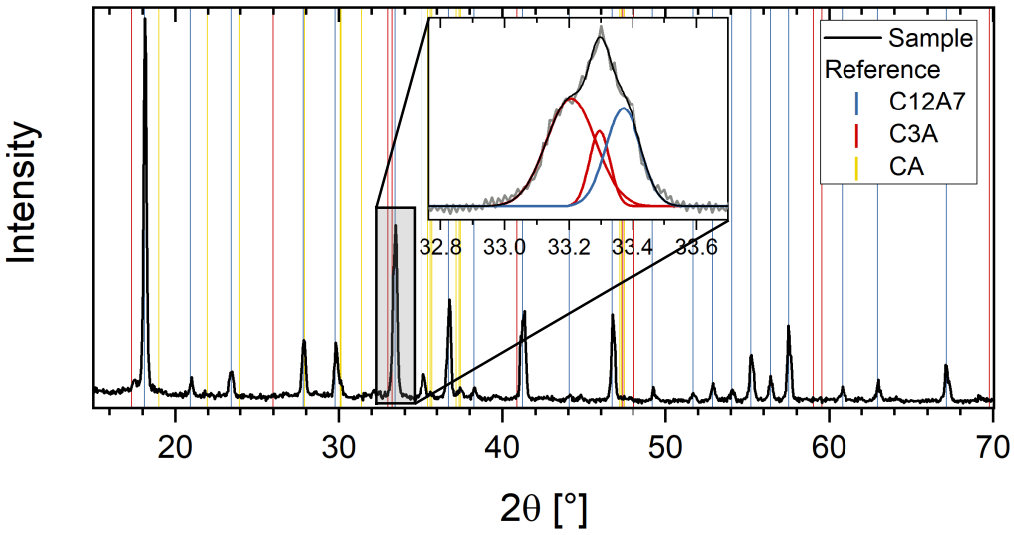

(b) after melting

Figure 3.9: XRD diffraction pattern of two planar inserts after operation in the planar cathode: a) after two hours of nominal operation and b) after melting of the insert. The diffraction pattern in the inset in b) provides a detailed analysis of the XRD signal around 33°, which is a convolution of one C12A7 and two C3A signals. Reference data for the different calcium aluminate phases is shown as coloured lines, data from [11, 110, 130].

In the case of non-pristine inserts, an additional temporary increase occurs and dominates the evolution of the keeper voltage with significantly higher increase rates of 0.07 V/min up to 3.7 V/min. This gradient prevents reproducible measurements of the cathode's performance and limits the time of continous operation to less than 30 minutes, as the increasing power input and the resulting temperature increase would otherwise damage the insert. Only during a single test run, a non-pristine insert showed a keeper voltage gradient equivalent to that of a pristine insert. Between the initial operation of this insert and the mentioned test run, an insert temperature of approximately 460 °C (heater power 66 W) was maintained. The nominal operation procedure involves an intermittent cool-down to room temperature between separate cathode operations.

The increase of the insert temperature, illustrated in Figure 3.7a, can be excluded as the cause of the increasing keeper voltage. If such a relationship existed, temporary increases in temperature as observed at 15 minutes and 45 minutes of operation, see Figure 3.7a, would also affect the keeper voltage. However, there is no such correlation. Instead, an inverse relationship applies: a higher keeper voltage is associated with a higher power input, which increases the insert temperature.

A partial surface coating of the C12A7:2e- insert can be used to prevent a temporary increase of the keeper voltage during operation. For this, two different platinum grid structures are sputtered onto electride samples. The high surface coverage of 54% in the first design hinders thermionic emission of the C12A7:2e- electride. Plasma discharges employing such an insert therefore require keeper voltages above 200 V. The second design utilises a significantly lower surface coverage (inset in Figure 3.10a). Initial operation with this insert indicates a comparable increase rate for U_K as a plain insert (0.03 V/min), see Figure 3.10a. This means that the improved electrical contact of the surface does not affect the permanent increase of the keeper voltage, which further evidences that this phenomenon is not dependent on charge transportation over the surface. It is questionable whether the improved stability observed in the given comparison can be attributed to the coated surface. Further testing with uncoated inserts showed similar stability levels. As the insert was cooled down to ambient temperature after the first operation, temporary effects should be visible in the following test runs. However, as depicted in Figure 3.10b, the voltage increase during operation remains at a low level of 0.05 V/min and no temporary increase is detected with respect to the previous ignition. Nevertheless, after the test, sputtered deposits from the cathode orifice covered the surface of the insert, including the grid. This could also hin-

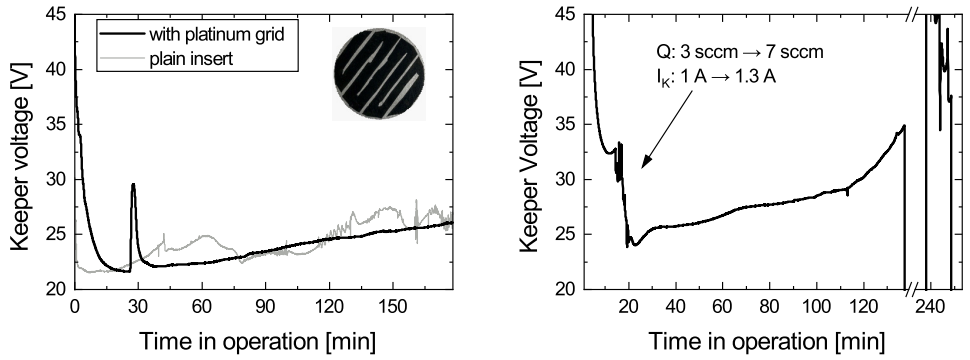

(a) *(b)*

Figure 3.10: a) Time evolution of the keeper voltage (with $I_K = 1$ A and $Q = 3$ sccm) for two different cathode inserts: one with a sputter deposited platinum grid (version 2) and one without. The increase in keeper voltage is almost identical for both insert versions. The insert with the sputter deposited platinum grid (version 2) is shown in the inset. b) Subsequent operation with the same insert after venting and inspection. The keeper voltage increases at a rate comparable to operation with a pristine insert, even though this insert has been used previously. Furthermore, the keeper voltage following a regeneration break does not fall below the final voltage of the previous iteration, which would suggest a temporary increase.

der the long-term effectiveness of the platinum grid. In addition, potential sputter erosion of the platinum grid itself can degrade performance.

Examining the performance of the thermionic planar cathode, operating with a C12A7:2e- insert, in detail confirms the trends described above. The key factor in the performance of the cathode is the condition of the insert employed. While a cathode with a pristine insert operates with keeper voltages in the range of 15 V to 19 V depending on the parameters, non-pristine inserts require significantly higher voltages for operation. In order to achieve keeper currents between 0.7 A and 1.3 A keeper voltages ranging from 30 V to 45 V are necessary in the subsequent test runs. Figure 3.11a displays the development of the keeper voltage per keeper current over five test cycles. The permanent increase of the keeper voltage with the operating time is also visible here, as the keeper voltage for a given current increases systematically over the test cycles. The pristine insert displays almost ohmic behaviour, yet an opposite behaviour is observed for the subsequent test cycles: an increase in current leads to a decrease in necessary voltage. The $U_K(I_K)$ relationship of the pristine insert is illustrated in detail in Figure 3.11b. The voltage-current characteristics shift to higher voltages for lower gas flows. Here, operating at 3 sccm necessitates voltages ranging from 17 V to 19 V, while operating at 5 sccm only

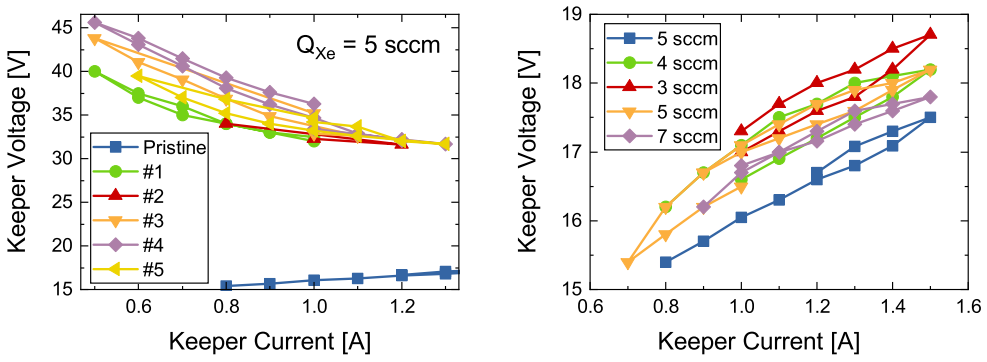

(a) *(b)*

Figure 3.11: Current-Voltage Characteristics in Diode Mode Operation: a) Development of the U-I characteristics over several test runs for 5 sccm xenon flow. The cathode was re-ignited between each measurement. Another test run (including venting) with a different orifice configuration was conducted between the initial run and No. 1 and is not shown here. The test chamber was vented between test runs 3 and 4. No cool-down was performed between test runs no. 1 and 2 and between 4 and 5. b) U-I characteristics for operation with a pristine insert. Measurements were taken in the order they appear in the legend (top to bottom) without any reignition performed in between.

requires 15 V to 17 V. However, precise quantitative conclusions cannot be drawn from these measurements as the one-minute time interval between them was inadequate to ensure stable plasma conditions after the propellant flow rate was changed. This issue is apparent when comparing the two $U_K - I_K$ curves for Q=5 sccm in Figure 3.11b. Similar values would be anticipated as the operating parameters are identical. Instead, the keeper voltage of the second 5 sccm measurement (yellow line) is higher than the first (blue line) for a given current. Apparently, the cathode was not in an equilibrium state when the second performance mapping was measured at 5 sccm. Instead, the measured $U_K(I_K)$ was influenced by the preceding performance mapping at 3 sccm. Due to the lower flow rates, U_K is higher for a given I_K. In the one-minute time interval between the change of the flow rate from 3 sccm back to 5 sccm, the keeper voltage adjusted to the new plasma environment, but did not fully reach its equilibrium state, leading to the observed higher keeper voltage. If the cathode is reignited prior to each measurement, there is no systematic shift in performance. In subsequent measurements this procedure is used therefore to ensure comparable conditions. Nevertheless, the overall trend is still clearly visible. In line with previous research, the amount of propellant used influences the keeper voltage required for a given current: the increased amount of propellant causes a higher particle density in the cathode, which reduces the plasma potential.

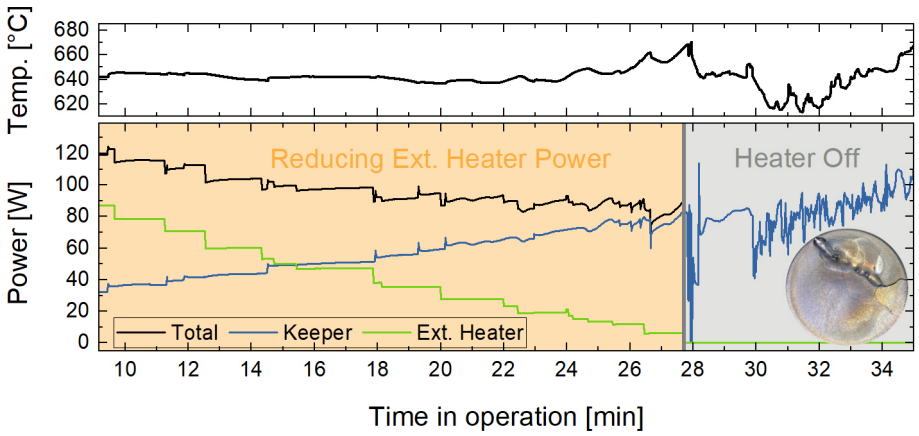

Figure 3.12: Time evolution of the heating powers (total input power, keeper power, and external heater power) is shown for two stages: first with a gradual decrease in external heater power, and then without external heater power. The plasma input power was adjusted to maintain the insert's surface temperature (top graph). Once the external heater is stopped, strong oscillations occur in the keeper voltage. The inset depicts the front side of the insert after operation, revealing that the insert melted where a previous crack had occurred.

The self-sustained heating mode is the preferred operating mode for space cathodes. This mode is reached when the plasma heating from the current drain to the keeper and the anode is sufficient to compensate the heat losses to the walls alone and an external heater is no longer required. Due to the electride material's low thermal conductivity, maintaining the same front-surface temperature of the insert in this mode will require a lower total power input. Heat is applied directly to the electron-emitting surface, rather than needing to be transferred through the bulk of the insert. An attempt to operate in self-sustaining heating mode is shown in Figure 3.12. In the shown case, the insert temperature remains constant while the plasma heating replaces the external heater (keeper current not shown in the figure). As previously explained, a lower total power input is required in self-sustained heating mode, only 83 W compared to 135 W in external heating mode. However, soon after entering self-sustained heating mode, the keeper voltage displayed significant oscillations, and the discharge was intentionally terminated. The subsequent inspection of the insert revealed a molten surface. It is unclear whether the oscillations were caused by the molten surface since this damaged surface displayed unstable emission properties (in other test campaigns with a hollow cathode, oscillations were indicative of insert melting), or vice versa since the heat input peaks at 115 W during the oscillation phase, suggesting that the melting

point of the material is exceeded. Significantly reducing the plasma input power to mitigate insert melting is not possible as this input power would not suffice to maintain the insert operating temperature. In other tests where the plasma input power was below 60 W, the insert temperature decreased rapidly as soon as the heater was turned off and the plasma went extinct. The implementation of an extra heat shield around the cathode could decrease thermal losses and facilitate self-sustained cathode operation.

3.2.4 Triode mode operation (keeper and anode)

The triode mode permits the extraction of electron current from the cathode. A plasma bridge between the cathode and the thruster (or in this case the external anode) allows an electron supply without space charge limitations and at comparably low voltages. When switching from diode mode to triode mode, the plasma must extend beyond the cathode and pass the empty space to the anode. This requires a sufficient electric field between the cathode and the anode. Initial attempts using an electric field of approximately 400 V/m failed. An additional pulse of 300 V pulse and a reduction in the keeper-anode distance from 200 mm to 20 mm increases the electric field to over 10 kV/m and establishes a plasma bridge between the cathode and the anode. Furthermore, the plasma bridge must be supported by a sufficiently high gas density. A propellant flow of 3 sccm (with a 1 mm keeper orifice and a 7 mm cathode orifice) is insufficient, as shown in Figure 3.16. However, once the plasma bridge is established, the gas flow can be reduced to this value (see the caption of Figure 3.16 for details). The planar cathode's performance operating in triode mode is illustrated in Figure 3.13. Electron currents ranging from 0.2 A to 0.4 A necessitate voltages between 32 V to 37 V, details are shown in Figure 3.13a. The anode voltage correlates with the current demanded in this case. A decrease in propellant flow, corresponding to a lower particle density in the plume, requires a higher voltage to maintain the same extraction current [33 p.312]. This trend is even visible for the small change of 0.5 sccm in Figure 3.13a and is shown over a wider flow range in Figure 3.13b. The voltage does not increase linearly with decreasing flow, but rather follows a nonlinear trend. Notably, at 3 sccm, a high voltage is necessary to compensate for the thin plasma environment.

Different discharge modes are defined for the operation of thermionic plasma cathodes. The *spot mode* is characterised by stable anode and keeper voltages without oscillations and manifests itself as a small plasma ball in front of the keeper orifice. The spot mode is also associated with a reduced

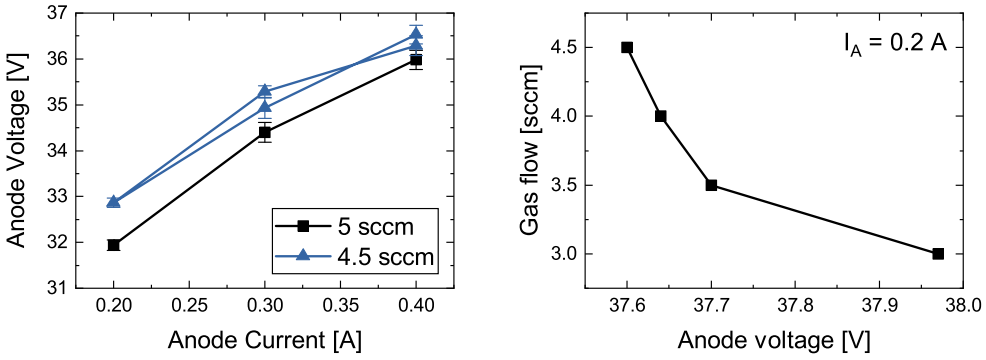

(a) *(b)*

Figure 3.13: Performance characteristics for the planar cathode operating with an external anode a) anode voltage to current relation for fixed gas flows of 4.5 sccm and 5 sccm, b) anode voltage for different gas flows at $I_A = 0.2$ A. Values were not obtained in equilibrium state.

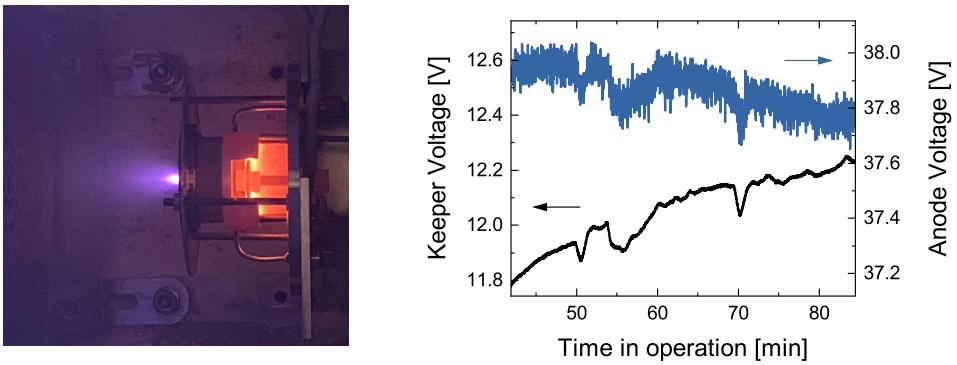

(a) *(b)*

Figure 3.14: Planar cathode operating in triode mode with electron current extraction. a) Image of the cathode with the plume. The external anode is located at the left side of the image. b) Anode and keeper voltage during a typical planar cathode operation in triode mode. The anode voltage (in blue) shows only small oscillations of about 0.2 V in amplitude. The keeper voltage (in black) is stable on a short time scale. Both voltages show a long-time drift.

keeper wear. Consequently, the spot mode is the preferred operating mode for hollow cathodes. In contrast, the *plume mode* shows strong oscillations[4] and a bright plasma cone [30, 33]. This change in mode occurs as a result of the cathode leaving its optimum operating point towards a lower propellant flow or an increasing current demand. Given the plume shape, depicted in Figure 3.14a, and the stability of the applied voltages, shown in Figure 3.14b, the cathode is considered to be operating in spot mode. A plume mode was not observed for the thermionic planar cathode.

Once a plasma bridge is established successfully, the cathode can operate for several hours in triode mode. More than four hours in triode mode have been accumulated so far. The Figures 3.15, 3.16, and 3.17 present the time evolution of the relevant operational parameters. These test runs show high extraction currents up to 1.4 A ($I_K = 1$ A and $I_A = 0.4$ A) with moderate keeper and anode voltages between 11 V and 14 V and between 36 V and 38 V, respectively. Also operation in anode diode mode is possible. Further tests are required here to identify the parameters required to maintain a stable insert temperature. A still existing challenge is the long term stability of the system. Although the system demonstrates a high level of stability in the range of minutes, the keeper voltage rises continuously over longer periods of time and so does the insert temperature. A constant insert temperature is key to mitigating insert melting and long-term stability. The parameters to balance the current extraction with the thermal input and losses are to be identified in future test campaigns.

[4]For the NSTAR cathode, the plume mode is defined as the point where keeper voltage oscillations exceed ±5 V [33].

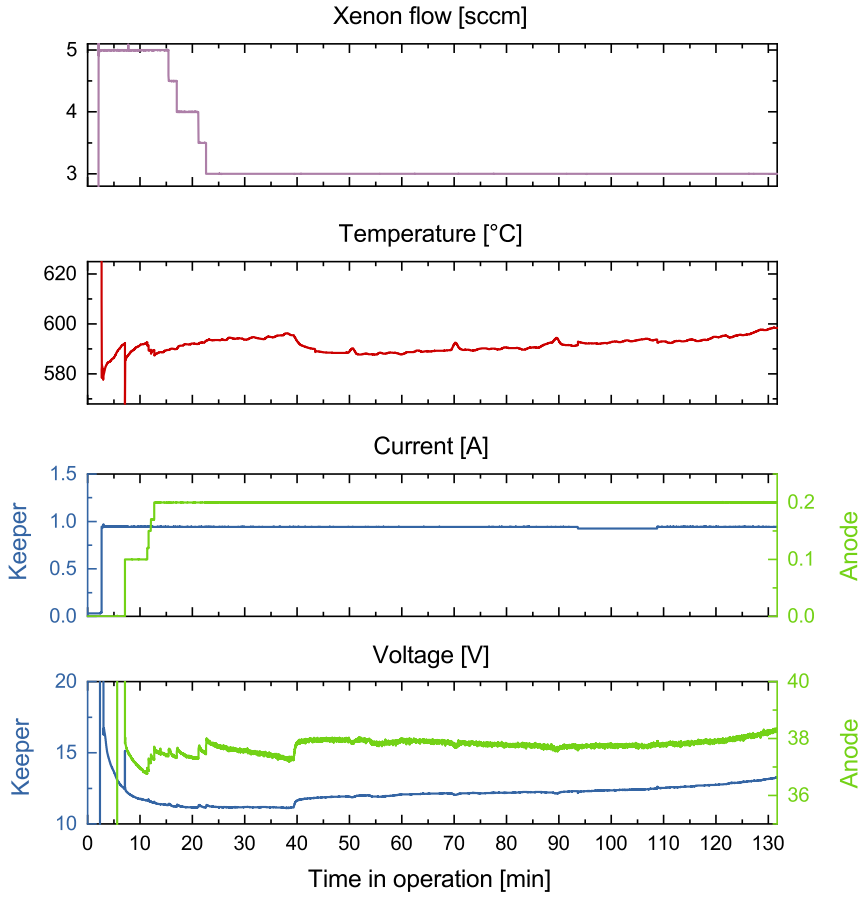

Figure 3.15: Cathode operation in triode mode no. 1. A pristine insert was used. The cathode was first ignited in diode mode, before switching to triode mode. After ignition, the keeper voltage decreased steadily until, 40 minutes into operation, the power of the external heater was slightly decreased. It is believed that this reduction in thermal input disturbed the thermal equilibrium of the device, resulting in a slow rise of the keeper voltage at about 8 mV/min. After 20 minutes, the gas flow was lowered to decrease the overall gas consumption. This only slightly affected the other parameters, although the anode voltage increased slightly, especially during the last reduction steps. In general, the test demonstrated high stability and was intentionally terminated.

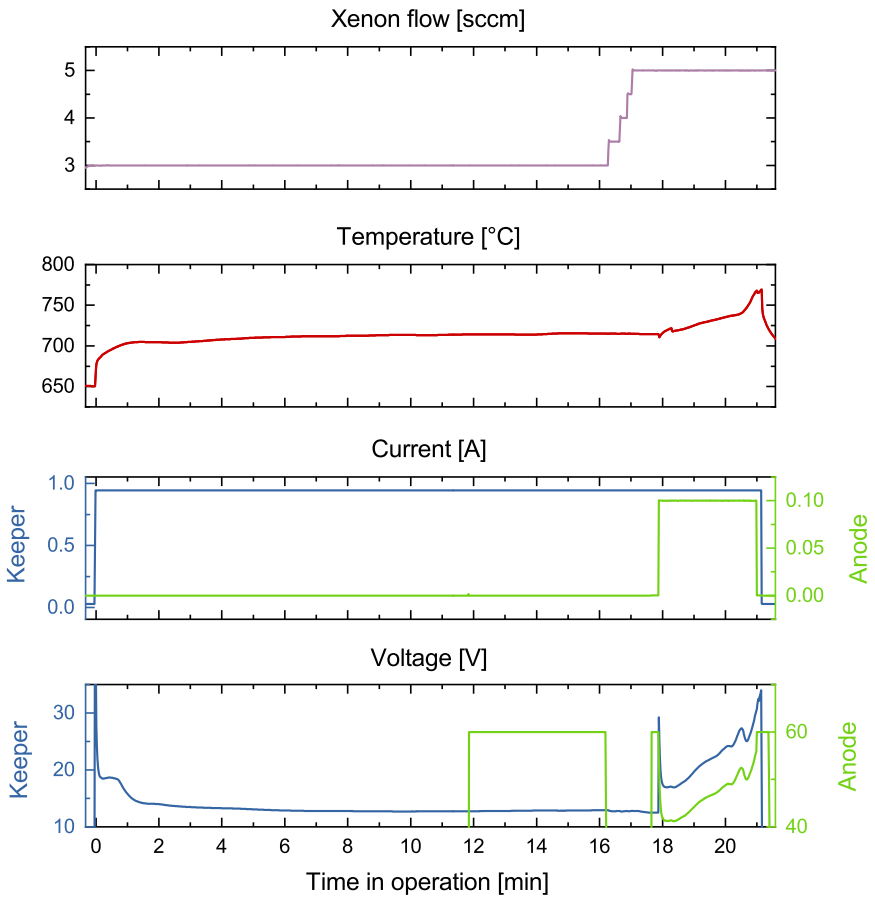

Figure 3.16: Cathode operation in triode mode no. 2. This test run followed run no.1 (i.e the same insert was used). An insert temperature of 460 °C was maintained in between. The cathode was first ignited in diode mode. The cathode operates very stable with a slight decrease in keeper voltage and a constant insert temperature. The first attempt to switch to triode mode (at 12 min) failed due to a to low gas flow, but after the gas flow was increased to 5 sccm the second attempt proved successful. However, both the keeper and the anode voltage and the insert temperature showed a steep increase and the discharge was terminated.

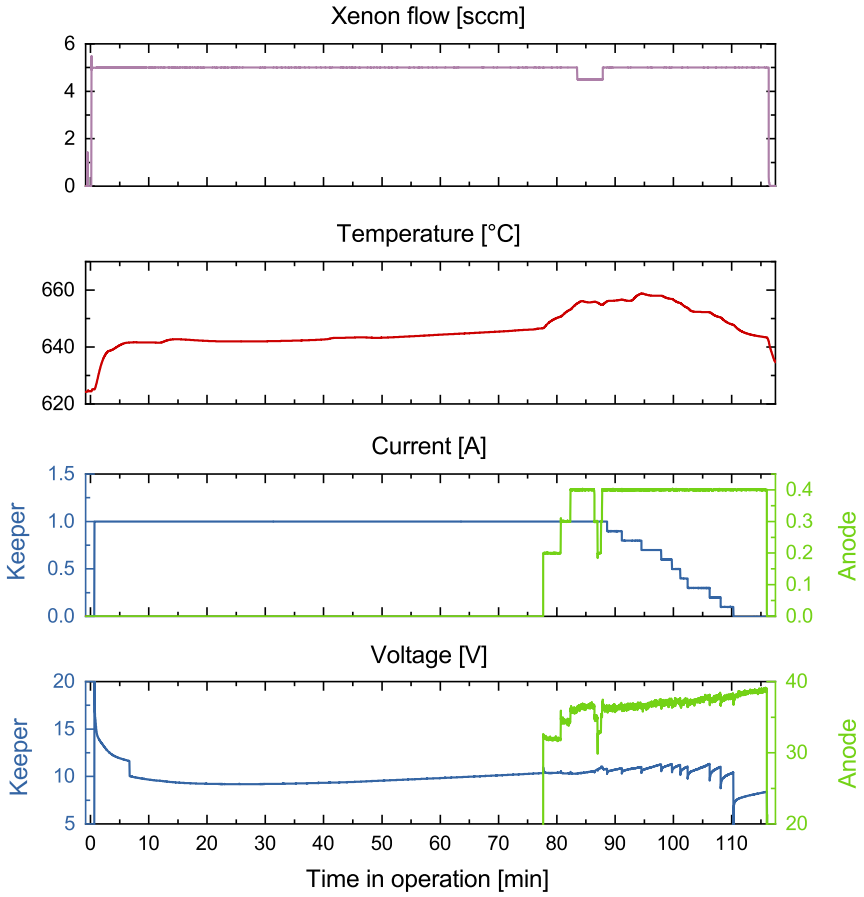

Figure 3.17: Cathode operation in triode mode no. 3. A pristine insert was used. The cathode was first ignited in diode mode. The cathode operates very stable with a slightly increasing keeper voltage and a constant insert temperature. The operation was then successfully switched to triode mode and the anode current could be increased to 0.4 A. At 80 min a performance mapping was done for 5 sccm and 4.5 sccm. Subsequently the keeper current was reduced continuously to investigate the possibility of an anode diode mode operation. The cathode runs stable in this mode, but the insert temperature decreases continuously. The anode voltage exhibits significantly higher oscillations compared to other tests.

3.2.5 Results

The insert is the key element of any thermionic plasma cathode. The tests presented in this work have shown the importance of the insert's condition for successful ignition and operation. Two processes alter the condition of the insert during cathode operation. First, a bulk deteriorative process leads to a low rate decrease in the insert's emission capability. This is noticeable as an increase in keeper voltage during operation, which persists after re-ignition and also after sanding the surface. However, no signs of a permanent alteration of the C12A7 crystal structure after nominal operation have been found above the instruments sensitivity[5]. Only strong oscillations during the test and the associated excessive heat input led to the formation of secondary calcium aluminate phases in the inserts. Ignition was still possible in these cases, but stable operation was detained by the damaged insert.

Second, during the intermittent cooling between test runs, a surface layer of low electrical conductivity forms on the insert's surface. During ignition, this process reduces the current available for a given applied voltage. Ignition may therefore fail. This insulating layer also inhibits the supply of electrons from the bulk. If more electrons are emitted into the plasma than can be replenished from the bulk, a positive charge accumulates on the surface. This potential inhibits the emission of additional electrons. Consequently, operation requires an increasingly higher keeper voltage. Due to the low conductivity of the surface layer, the aforementioned regeneration phase without current extraction is required to allow the surface to return to a charge-balanced state. This process is therefore associated with the temporary increase observed for previously operated inserts. Such a charge-up can be mitigated by contacting the surface of a C12A7:2e- sample, for example with a sputter-deposited platinum grid, as demonstrated in this work. Damage to the unique crystalline structure of the C12A7:2e- insert at the surface can be excluded as the cause of the behaviour described above. Such damage would also affect the material's electron emission ability. Regenerating the broken cages at elevated temperature would restore the C12A7 specific cages. However, according to Ref. 117, restoration of a distorted surface requires temperatures above 900 °C, which are not reached during this annealing process. This hypothesis also fails to account for the favourable performance of the platinum coating. Besides the condensation of insulating material, also micro-cracks

[5]Initial measurements with a XRD device of higher sensitivity show signs of a C3A phase. However, as the respective sample was not measured before operation, a contamination from the production process has to be excluded first, before further conclusions are drawn. Additional test campaigns are required to further study this finding.

in the surface, as reported by Ref. 127, could cause a layer of low electrical conductivity. In this context, it is evident that performance similar to that of a pristine insert can be regained by removing the altered surface layer, for example through sanding, as the insert's bulk is only mildly affected by the first process. Utilising the former back side of the insert that was previously facing the heater also eliminates the impact of the surface layer.

C12A7:2e- inserts can therefore be categorised as pristine, where only the first process applies, and non-pristine, where the second process dominates the operating behaviour. Pristine inserts can be reliably ignited at low keeper voltages and exhibit low voltage rise rates. Non-pristine inserts require considerably higher voltages for ignition. During operation, a temporary surface charge leads to a rapid increase in keeper voltage. Further investigation of these processes is of great importance, particularly with regard to the evaluation of different cathode geometries. Not for every cathode configuration a new insert can be used due to its limited availability and high price. The systematic error due to the ageing of the insert needs to be distinguished from other effects.

3.3 NACES Cathode

The NACES cathode is a C12A7:2e- based cathode, developed by Advanced Thermal Devices. Cathodes of this particular design operate at temperatures of about 300 °C, signifincantly below the electride's melting point of 1415°C [74]. The ability to ignite the cathode at room temperature is a significant advantage. In this work, the NACES cathode is used for investigating the impact of several alternative propellants on the performance of a neutralising cathode as well as their compatibility with the insert material C12A7:2e-. The long-term stability of operation with the alternative propellant krypton is also studied. Accompanying characterisation of the inserts with Raman spectroscopy allows one a close monitoring of the insert's degradation throughout operation.

3.3.1 Design

The NACES cathode uses a disk-shaped 1" (25.4 mm) in diameter and 2 mm thick C12A7:2e- electride insert as the electron emitter to take advantage of the benefits of planar cathode geometries. The design employs no heating element as the device can be ignited at room temperature and is subsequently heated by plasma heating. The cathode is composed of a body and a cap, which serve to electrically contact the insert. The cathode body is made of copper to enhance heat dissipation from the insert in order to mitigate insert melting. Similar issues with insert fragmentation as described in Section 3.2.1 occurred during initial testing. The same strategy of implementing a graphite foil between the electride and the metal cathode also reduces this issue in the case of the NACES cathode. The keeper is located a few millimetres above the insert's surface. The propellant is injected through a 1/16" tube, later a 1/8" tube, into the alumina plasma chamber. A 5 mm orifice allows the generated electrons to be collected by the anode, which mimics the plume potential of an electric thruster. It is located 30.75 mm downstream of the orifice, which is 10.6 mm away from the keeper. The lower operating temperature eliminates the need for expensive refractory materials. Stainless steel for the keeper, aluminium for the cathode cap, and mica for insulation can be used without restriction. The design is shown in Figure 3.18.

To enhance propellant ionisation, a configuration similar to that used in magnetron sputtering devices is used: A magnet configuration inside the cathode creates an rotationally symmetric magnetic field above the insert. The radial magnetic field component (i.e., parallel to the surface of the insert) is in the range of 10^{-3} T [13]. In addition, the perpendicular com-

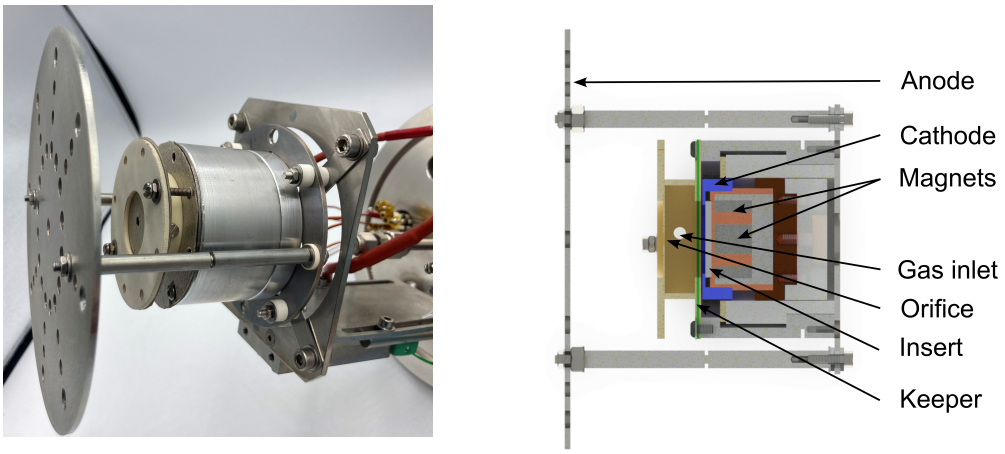

(a) (b)

Figure 3.18: a) Image of the integrated laboratory model b) Cut view of a CAD model of the NACES cathode.

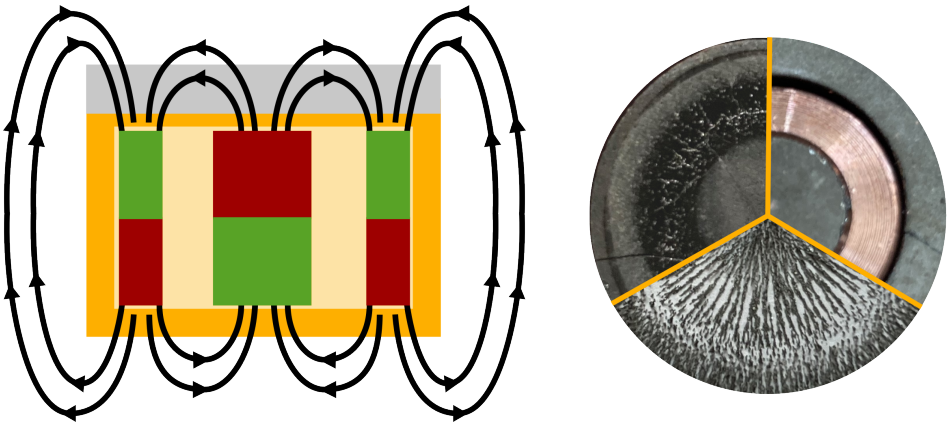

(a) (b)

Figure 3.19: a) Schematic image of the magnetic field of the NACES cathode. A cylindrical magnet and a ring magnet are oriented opposite to each other. This representation is derived from the measurement results described in the text and verification with a bar magnet. b) Side-by-side view of a typical sputtering pattern on an insert (upper left), the magnets employed in the NACES cathode (upper right) and the magnetic field lines made visible by iron powder (bottom). A copper spacer is placed between the two magnets. All images have the same scale. It can be seen, that the sputter pattern on the insert coincides with the space between the two magnets, where the field line are oriented parallel to the insert's surface.

ponent, which is in the range of 10^{-2} T, exhibits a gradient from the axis of symmetry towards the edge of the sample. The magnetic field lines change direction at a radial distance of about 6 mm to 7.5 mm from the axis of symmetry [13][6]. A schematic illustration of the resulting magnetic field is shown in Figure 3.19a. The magnetic field forces the electrons in the plasma onto circular trajectories. The gyration extends the electron's path, resulting in a higher electron-ion collision rate and thus an increased plasma density. The gradient in the perpendicular component of the magnetic field creates a magnetic trap for the electrons: The so-called *gradient drift* creates a force towards regions of a lower field line density. Applied to the NACES cathode, this corresponds to the space between the inner and the outer magnet. As the magnetic field density is higher in both inward and outward direction, the electrons are confined in this region. The increased electron density results in a significantly higher ionisation rate in this region. Indeed, optical inspections of inserts subsequent to operation show a pronounced sputtering pattern on the insert's surface in this region, as shown in Figure 3.19b.

The NACES cathode testing circuit is illustrated in Figure 3.20. The anode is powered by a *TTI CPX200* power supply (maximum 60 V and 10 A). An anode voltage of 20 V has been used for the tests presented in this work, unless otherwise stated. The keeper is separated from the common ground potential by a 1 MΩ resistor, which helps to stabilize the ignition, as explained in Ref. 21. The cathode is biased negatively with respect to ground and is powered by a specialized circuit comprising a power supply (a *FUG MCP 350-2000* 2000 V, 150 mA) and two supplementary units, namely, the *Ignition Box* and the *Pulse Box*. Figure 3.21 presents a circuit diagram of these components. The ignition box employs a pair of capacitors charged with a voltage of -500 V to supply a short high voltage pulse of the order of -750 V to the cathode. The ignition box presents two advantages over high DC voltage ignition. Firstly, ignition with the box is more reliable. Secondly, the high voltage is applied for a short duration and the total charge stored in the capacitors is small, protecting the device from excessive sputtering. Due to the presence of two resistors between the cathode power supply and the device output, the actual cathode voltage differs from the power supply output. Therefore, it is measured separately with a multimeter. Leakage currents in the pulse box also require separate measurement of the actual cathode current. The pulse box stabilises the operation of the cathode by converting the constant voltage input from the power supply into a pulsed voltage using a high-speed MOSFET gate

[6]The corresponding figure in the given reference erroneously states that the parallel field component is depicted.

driver fed by a 50 kHz square wave signal with a 50% duty cycle. A diagram of the resulting voltage signal is presented in Ref. 94. This pulsed voltage is designed to improve the thermionic emission ability of the C12A7:2e-electride by circumventing the limitations of an electron-deficient dielectric surface layer. A systematic study is presented in Section 3.3.2. The voltages given hereinafter for operation in pulse mode are peak voltages.

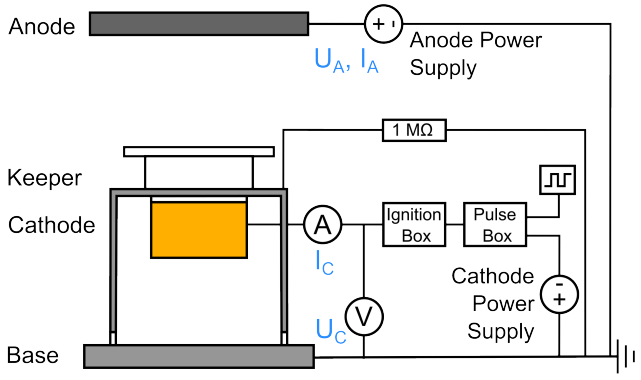

Figure 3.20: Overview of the circuit used for NACES cathode operation. Relevant cathode components are depicted on the left. Measured currents and voltages are indicated in blue. Detailed views of the ignition box and pulse box are featured in Figure 3.21.

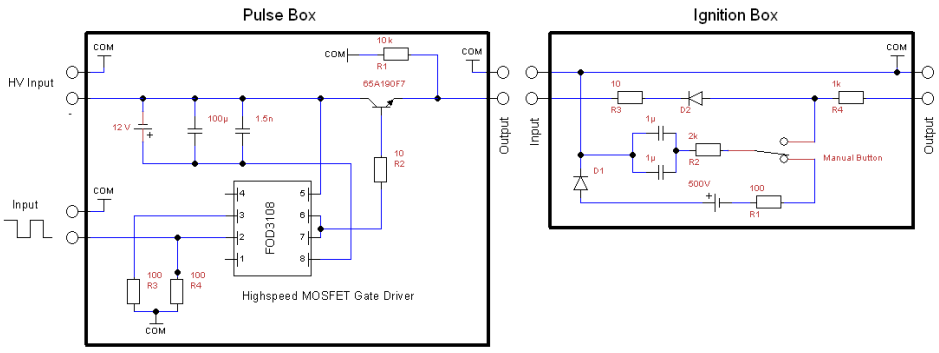

Figure 3.21: Detailed view of the electrical circuit diagrams of the ignition box *and the* pulse box*. In the course of this work, the R1 resistor in the pulse box was replaced by a 33 kΩ resistor to reduce the leakage current to common ground and allow higher input voltages.*

3.3.2 Operation

Ignition of the NACES cathode is typically achieved by applying a moderate voltage between 200 V and 400 V. The specific value and necessary gas flows vary significantly based on the propellant type, which will be further described in Section 3.3.3. Also, the temperature required for ignition depends on the propellant used. While argon allows ignition from room temperature, preheating is necessary when using xenon or krypton. This can be achieved either by using an argon plasma or an external heater. The stability during operation is also highly dependent on the propellant and will be discussed later.

Two parameters characterize the performance of the NACES cathode during operation: the emission efficiency, which is described by the $U_C(I_C)$ relation, and the extraction efficiency, which is influenced by the $I_A(I_C)$ and the $I_A(U_A, Q)$ relation. The emission efficiency describes the required voltage to release a given number of electrons from the cathode, i.e. the insert. The behaviour of the $U_C(I_C)$ curve depends on the operating mode used. In the normal mode, there is a positive slope where a higher cathode current demands a higher bias voltage. Figure 3.29a provides an example of this behaviour. In the pulsed operation mode, however, there is a negative slope, which can be seen in Figure 3.34. Apparently the plasma environment also changes with the mode change, but the detailed processes remain to be investigated. Smaller propellant flows necessitate a higher bias voltage to obtain the same cathode current levels, due to the lower plasma density. The anode voltage applied also affects the relationship. On long time scales, different effects influence the $U_C(I_C)$ relation, which will be discussed in Section 3.3.4.

The anode current is determined by two factors: the cathode current available (which in turn is dependent on the cathode voltage) and the fraction of this current that reaches the cathode. The latter is influenced by the overall plasma optics (such as orifice diameters), the plasma density, i.e. gas flow, and most importantly the anode voltage. The anode current for a given device configuration can therefore be described by

$$I_A(I_C) = \epsilon(U_A, Q) \cdot I_C + b \tag{3.3}$$

where the parameter ϵ refers to the ratio of electrons released by the cathode to those collected by the anode. The parameter b is introduced to account for any possible losses of cathode current. Additionally, there are indications that the absolute magnitude of the cathode current has an impact on ϵ. An analysis of the data published by Ref. 118 for the identical

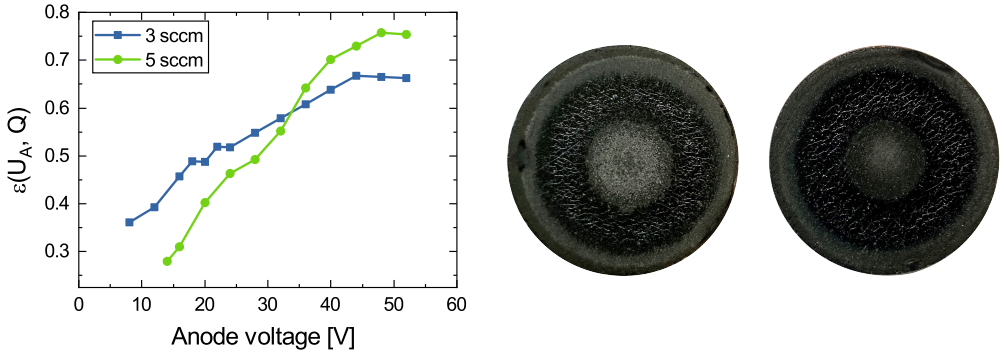

(a) *(b)* *(c)*

Figure 3.22: a) The ϵ value as a function of the anode voltage for 3 sccm and 5 sccm. ϵ describes the ratio of electrons reaching the anode to the number of electrons emitted by the insert. $I_C = 31\,mA$ for 3 sccm and $I_C = 33\,mA$ for 5 sccm. Data taken at Ch7 (keyword according to Table 3.1). b) Inserts employed for comparing pulsed mode to non-pulsed mode: Insert after 16 hours of operation in non pulsed mode and c) in pulsed mode.

device supports this finding. The parameter ϵ as a function of the anode voltage U_A and the gas flow Q is shown in Figure 3.22a. It increases with the anode voltage and reaches a saturation value. The slope of this factor scales with the amount of propellant injected. This leads to higher absolute values of ϵ for higher gas flows on the high voltage side of the relation, but also to lower values on the low voltage side. To maximise ϵ, both the gas flow and the voltage range must be considered. Optimal parameters can yield ϵ values close to 1. For instance, this is the case for the comparison of the three noble gases, as illustrated in Figure 3.28b ($U_A = 20\,\mathrm{V}$). In this case, the $I_A(I_C)$ relation is very well described by

$$I_A(I_C) = I_C - (7\,\mathrm{mA} \pm 1\,\mathrm{mA}). \tag{3.4}$$

The I_A/I_C ratio is a useful quantity for describing the overall performance or changes in a specific setup. It should be noted, however, that this ratio is not constant with the cathode current. This is due to the y-intercept b in the $I_A(I_C)$ relationship, which instead leads to a relation of $I_A/I_C(I_C) = \epsilon + \frac{b}{I_C}$. As a result, I_A/I_C ratios obtained from different I_C ranges, i.e., from different U_C ranges, cannot be compared. Similar to the emission efficiency, the extraction efficiency is also influenced by sputtering deposits from operation, both in the slope and the y-intercept of the relationship. Further details are given in Section 3.3.4.

To examine the impact of pulsed input voltage on the NACES cathode, a

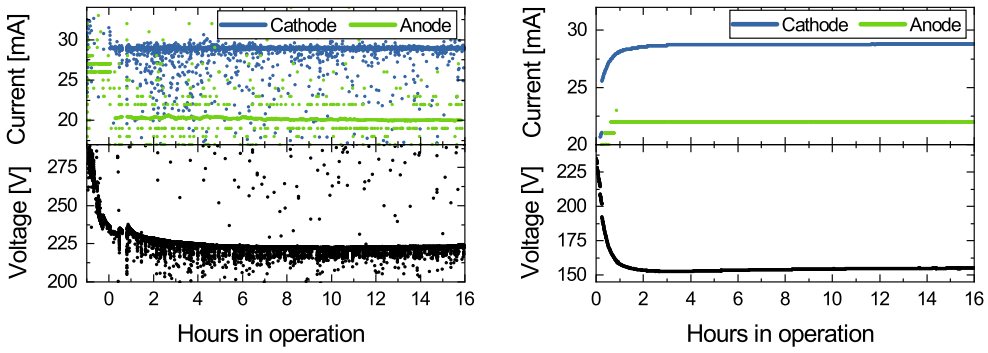

Figure 3.23: Operation of the NACES cathode in a) normal mode b) pulsed mode. In both modes the cathode is operated in constant current mode. The cathode current is adjusted to maintain a constant anode current of 20 mA (normal mode) and 22 mA (pulsed mode) throughout the test while using 5 sccm of krypton.

pristine insert is used for each test and the cathode is operated for 16 hours with and without pulsed voltage using krypton as propellant. Ignition, discharge stability, performance and insert wear are analysed. In both modes, ignition requires only a few high voltage pulses from the ignition box. However, initial discrepancies in operational stability appear in the immediate post-ignition phase: While the discharge can be sustained without any further issues in pulse mode, in non-pulsed mode it extinguishes after just a few minutes. In such cases, reignition is possible, but it requires repeated reignition for about 30 minutes before stabilisation of the operation is achieved. It is likely that this instability emerges from the cathode's initial 'cold ignition'. Due to the (unstable) nature of the operation, the insert temperature rises, and operation stabilises. Despite this, the difference in stability remained during operation: Specifically, pulsed mode operation necessitated no reignition within the 16-hour operation period; on the other hand, non-pulsed operation required a total of 172 automated reignitions within the same timeframe. Also aside from plasma extinctions, the non-pulsed operation exhibited more instabilities and current peaks, as evident in Figure 3.23. A further test run of 100 hours confirmed the high operational stability of the pulsed mode. The system sustained no plasma-induced extinction during the entire 100 hours, with the exception of a single restart caused by a software issue. Moreover, the pulsed mode achieved equilibrium state of the cathode voltage within a shorter period (2.5 hours) than the non-pulsed mode (7 hours) after ignition. For a given anode current of 20 mA in normal mode and 22 mA in pulsed mode, the required cathode voltage U_C is considerably lower in pulsed mode (155 V

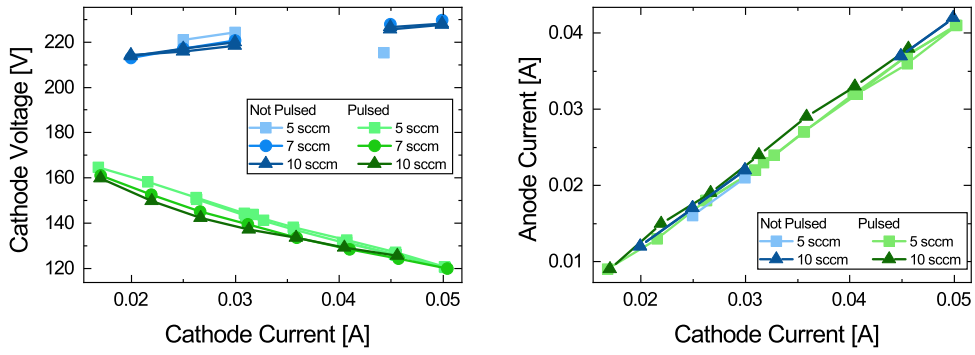

(a) *(b)*

Figure 3.24: Performance characteristics of the NACES cathode a) cathode voltage U_C to cathode current I_C b) anode current I_A to cathode current I_C.

compared to 223 V). Two factors contribute to this difference. Firstly, a higher voltage U_C is required in normal mode for a given cathode current I_C, i.e. electrons released by the cathode. The U_C/I_C ratio can be used to express this relationship, which is 5.3 V/mA in pulsed mode and 7.7 V/mA in normal mode. An important issue, elaborated in Section 3.3.4, concerns the rise in the U_C/I_C ratio. This means that increased cathode voltage is required during the test in order to maintain a constant cathode current. The increase did not vary significantly according to the operational mode (0.43% increase in pulsed mode versus 0.35% increase in normal mode over a 9-hour operation). The main difference between normal and pulsed mode is the global trend of the $U_C(I_C)$ relationship. In normal mode, the voltage needed increases linearly with the current, whereas in pulsed mode an increasing current requires a decreasing voltage, see Figure 3.24a. Secondly, the I_A/I_C ratio displays a marginally better value in pulsed mode, with 0.77 compared to 0.69 in normal mode at 5 sccm. The characterization for both the normal and pulsed modes is shown in Figure 3.24b. In particular, the I_A/I_C ratio is significantly better maintained in pulsed mode over long periods of operation. In normal mode, the I_A/I_C ratio decreases considerably after approximately 70 hours, whereas no such behavior was observed in pulsed mode. These two factors together lead to the previously mentioned noteworthy improvement in performance. Detailed performance mappings for both modes are shown in Figure 3.25a. When using the same input power, the pulsed operation mode provides twice the anode current. This is particularly advantageous for high extraction currents. Visual inspection of the two inserts after operation, see Figure 3.22b and Figure 3.22c, shows more pronounced sputter deposits on the insert operated in normal mode. This suggests a reduced degree of sputtering

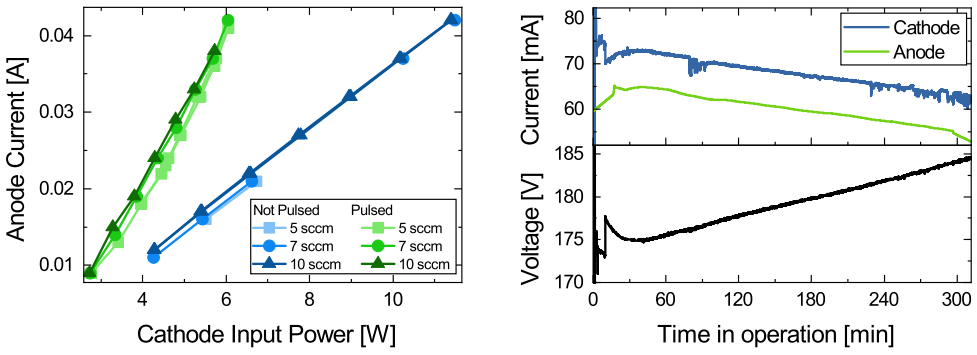

(a) *(b)*

Figure 3.25: a) Performance characteristics of the NACES cathode (obtained anode current I_A per input power $P = U_C \cdot I_C$). b) Evolution of cathode voltage and cathode and anode current for the NACES cathode over 5 hours of operation with 15 sccm argon as propellant. The drift noticed in both the cathode voltage and anode and cathode current is caused by a degradation of the insert, which reduces the resulting cathode current for a given bias voltage. Since the cathode power supply was operated in constant voltage mode, the cathode current decreases. Additionally, the real cathode voltage is linked to the current flow due to two resistors in the ignition box, thus also the cathode voltage increases over time.

for operation in pulsed mode. Both higher operational stability and lower cathode voltage are responsible for this. Despite this observation, the Raman spectra of the bulk material (taken in the circular regions exposed by sputtering) show no difference between the constant input voltage operation and the pulsed input voltage operation. This shows that the bulk electride material is not affected by the mode chosen.

In summary, pulsed mode operation shows significantly improved performance and stability compared to non-pulsed operation. The improved performance originates mainly from a lower cathode voltage per cathode current and to a lesser extent from a slightly improved I_A/I_C ratio. Both the improved stability and the lower cathode voltage also have a positive effect on insert sputtering, which in turn reduces insert depletion and the deposition of insulating sputter residues. As sputter residues are the main contributor to reduced extraction efficiency (lower I_A/I_C ratio), reduced sputtering also reduces the degradation of extraction efficiency during continuous operation.

3.3.3 Alternative Propellants

Alternatives to xenon are being sought due to several disadvantages exhibited by its use as propellant, in particular its price, as discussed in Section 3.1. Other more abundant noble gases, such as argon and krypton, require only minor changes in design and operating parameters. In addition, iodine is a promising but challenging alternative. For iodine testing, equipment must be adapted to meet the requirements of this propellant. A particular issue is the compatibility of the insert material with the high chemical reactivity of iodine. The objective of this study is to examine the impact of various propellants on the operation of the NACES cathode. Specifically, the experiments conducted in this thesis will offer initial guidance on the suitability of C12A7:2e- electride with iodine as propellant. The tests presented in this section were carried out before the pulse box was installed in the circuit. Accordingly, the findings displayed here indicate greater instability and an accelerated degradation of the delivered current per input power.

Argon

Operating the NACES cathode with argon as propellant results in reliable ignition and comparable stable behaviour. To ignite the device, cathode voltages ranging from 150 V to 200 V in combination with a pressure surge are required. Figure 3.28a illustrates a detailed performance mapping. Extraction currents of up to 67 mA can be achieved depending on the voltage and propellant flow applied. The resulting anode current scales in a linear manner with the applied cathode bias voltage. In general, a higher propellant flow rate improves performance. It is possible to operate with a propellant flow of 7 sccm or larger; however, below this threshold, the plasma extinguishes. When argon is used as propellant, the NACES cathode exhibits stable operation without any voltage peaks or oscillations. No instabilities were observed. The plasma ignites and extinguishes after several hours, on average, using this propellant. An accumulated operating time of 20 hours was achieved. Figure 3.25b shows an example of continuous operation for 5 hours. The observed continuous drift is caused by an increase in the U_C/I_C ratio, due to a degradation of the insert. Sputtering seems to be negligible as reason for this drift, as the I_A/I_C ratio remains nearly constant during the test (0.89 at the beginning with a pristine insert compared to 0.87 after 5 hours operation). These findings are confirmed by results from project partners [100].

Krypton

Using krypton as propellant for the NACES cathode without the previously presented pulse box installed results in unreliable ignition behaviour and low operational stability. Ignition can be improved by preheating the device with an external 10 W heater to approximately 100 °C. Cathode voltages of approximately 220V and a gas flow of 5 sccm are then required. A detailed performance mapping is shown in Figure 3.28a. An extraction current of up to 23 mA is achieved, depending on the applied voltage and propellant flow. The resulting anode current increases linearly with the applied cathode bias voltage. Generally, better performance can be obtained with higher propellant flow rates. The operational limit is 3 sccm for propellant flow, below which the plasma extinguishes. When using krypton as propellant, voltage peaks occur and the average operating time between two restarts is only 30 minutes. To achieve prolonged operation, a reignition algorithm had to be implemented to automatically reignite the discharge to achieve (near) continuous operation over longer time scales. Despite this, an elevated degree of sputtering during krypton operation produces an amorphous and insulating layer on nearby parts. The deposits had a severe impact on both the keeper and anode potentials. Over 100 hours, the cathode current achieved for a given cathode voltage decreased from 0.18 mA/V to 0.13 mA/V. Moreover, the anode current per cathode current decreased from 0.75 to 0.35. Consequently, this degradation significantly impairs overall performance, as indicated in Figure 3.26a. To achieve an equivalent extraction current, an input power of 1.6 to 2.3 times to that of the power used originally is necessary, depending on the gas flow. Given the limitations of the electrical infrastructure, this continuously increasing power also limits the maximum operating time. As outlined in Section 3.3.1, incorporating the pulse box significantly enhances stability and maintains the device's performance. Endurance tests with this unit and krypton as propellant are presented in Section 3.3.4.

Xenon

The operational behavior of the NACES cathode with xenon as propellant is comparable to operation with krypton; it has an unreliable ignition behaviour and low operational stability. Preheating, either through plasma heating with argon as the propellant, or with an external heater, facilitates ignition. A gas flow of 3 sccm and cathode voltages around 240 V are then required. Figure 3.28a presents a detailed performance mapping. Depending on the applied voltage and propellant flow, the device can reach an extraction current of up to 16 mA. The resulting anode current scales linearly with the applied cathode bias voltage. In general, a higher propellant

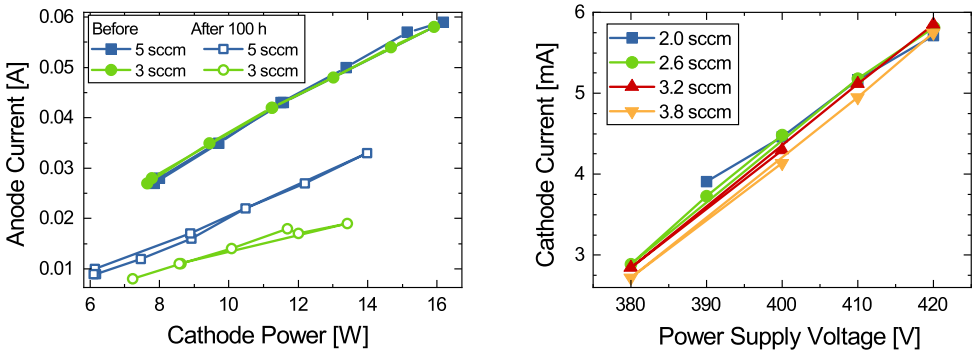

(a) *(b)*

Figure 3.26: a) Performance of the NACES cathode with krypton before and after 100 hours of operation for 5 sccm and 3 sccm propellant flow. b) Performance of the NACES cathode with iodine. Due to a data processing malfunction of the multimeter, the cathode voltage was not recorded and the output voltage of the power supply is given instead.

flow rate improves performance, viable with a propellant flow of 1.5 sccm or greater. Below 1.5 sccm propellant flow the plasma extinguishes. The device operated for approximately 35 hours using xenon as its propellant.

Iodine

To operate the NACES cathode with iodine as propellant, it must comply with iodine-specific design aspects. First, the materials used in the cathode must exhibit low reactivity with iodine. The anode, the keeper, and the propellant feed system are made of stainless steel, which is rather iodine compatible. Although copper, which is used for the cathode body, reacts heavily with iodine, it has a good thermal conductivity. Nevertheless, this material choice was kept, accepting the higher reactivity with iodine. However, the chemical reaction with iodine caused significant damage to the cathode, especially to the thread joining the cathode body and the cathode cap. Therefore, for future tests, alternative materials for the cathode body or a different type of connection between the cathode cap and body should be evaluated. Second, recondensation of iodine, which is solid at ambient conditions, in the gas supply system must be avoided. The gas supply system must be kept at an elevated temperature. To achieve this for the NACES cathode, the teflon gas supply tube is replaced by a stainless steel one. Two wire heaters are installed around the tube and the keeper as shown in Figure 3.27b. Additionally, it is advisable to avoid small pipe diameters to ensure optimal gas conductance and prevent the development of local pressure maxima. Instead of a 1/8” gas supply line as used for

noble gas operation, 1/4" tubes are used (and 1/8" for direct injection).

The NACES cathode operation using iodine as propellant requires bias voltages in the range of 400 V with gas flows around 3 sccm. Despite the high cathode voltage, cathode currents do not exceed 6 mA, see Figure 3.26b. Due to the low cathode current, no anode current can be extracted. Furthermore, the high cathode voltage causes significant sputtering. The insulating sputter deposits quickly decrease the device's performance by raising the U_C/I_C ratio by approximately 19% within 50 minutes. Thus, increasing the cathode current while decreasing the cathode voltage is highly desirable. Despite the high bias voltage, the NACES cathode operates stably with iodine as a propellant, and no sparking or other instabilities have been observed during a 2 hour and 45 minute period of operation. A visual inspection after eight hours of operation shows a sputtered ring-like structure on the insert, see Figure 3.27a, which is observed independently of the propellant (for comparison, an insert operated with xenon as propellant is shown in the same figure). There was no other evidence of deterioration of the insert apart from this device-specific sputtering. This indicates that iodine plasma exposure does not alter C12A7:2e- in a different way to noble gases, i.e. physical sputtering is the dominant process and no chemical enhancement occurs.

Comparison

In this work, the operational stability and performance of the four propellants argon, krypton, xenon and iodine have been investigated. The voltage necessary for ignition in addition to the high voltage pulse from the ignition box with the various propellants is determined by the *Paschen curve* for the respective gas (the actual voltage is slightly lower due to the magnet used). The necessary breakdown voltage for a given pressure and electrode spacing increases from argon to krypton to xenon [128] to iodine. Anode current extraction is achieved for all three noble gases with up to 80 mA depending on operating parameters. However, with iodine only small cathode currents can be drawn from the insert. The best stability was achieved with argon and iodine, both running for several hours without major instabilities or plasma extinction. In contrast, krypton and xenon exhibit lower stability and experience frequent plasma extinction. Nonetheless, the introduction of a pulsed bias signal via the pulse box eliminates this disadvantage and also gives high operational stability with krypton. The minimum gas flow required for operation depends on the propellant chosen. Argon requires a minimum flow of 7 sccm, whereas krypton can be operated at 3 sccm and xenon at only 1.5 sccm. For a particular

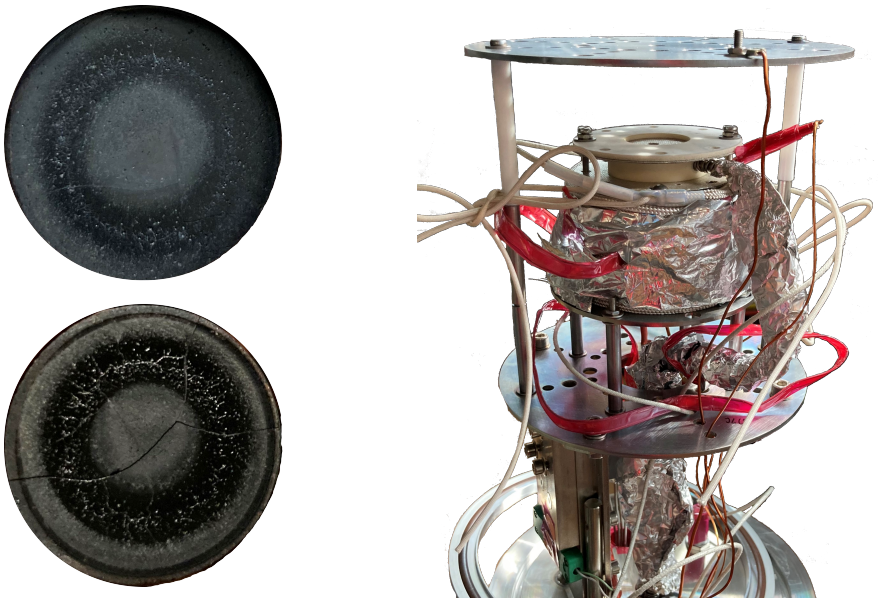

(a) (b)

Figure 3.27: a) Images of inserts after 8 hours of iodine operation (upper image) and 22 hours of xenon operation (lower image), respectively. b) Image of the NACES cathode with the modified propellant supply system and the heaters for the device itself and the gas lines.

propellant, the performance increases with the flow rate used, but is not the determining factor.

A comparison of noble gases reveals that the overall performance depends mainly on the type of propellant. Argon displays the highest performance, ranging from 4 mA/W to 5 mA/W, while krypton falls below these values with a range of 2.8 mA/W to 3.5 mA/W. Contrary to expectations, xenon exhibits the poorest performance of all three noble gases analysed, with a range of 2.1 mA/W to 2.6 mA/W. This finding is particularly unexpected as xenon has the lowest ionisation potential of all three noble gases. Moreover, previous research has indicated a higher performance of xenon compared to krypton, see Section 3.1. However, these investigations were obtained for thermionic plasma cathodes and may not apply to plasma cathodes that employ a magnetic field. As previously discussed, the performance of the system is determined by two operational parameters. The first parameter is the I_A/I_C ratio, which represents the extraction efficiency, i.e. how many electrons provided by the cathode are available to the coupled thruster. There is no discernible difference in this relation for the three noble gases examined or the gas flow used, as shown in

Figure 3.28b. A reduced I_A/I_C ratio will be noticed only, if the particle density fails to support the maximum attainable electron current, such as during the operation with 2 sccm xenon. The second difference is the cathode voltage U_C required to obtain a given cathode current I_C. Significant differences are seen between the propellants for this parameter. While the cathode can be operated with argon at cathode voltages below 200 V over a wide range of cathode currents, krypton requires 210 V to 240 V and xenon even 260 V to 285 V, as shown in Figure 3.29a. The gas flow slightly affects the cathode voltage (the impact is most pronounced with argon), but the choice of propellant determines the overall range of U_C. The necessary cathode voltage for a fixed cathode current scales linearly with the molecular mass of the propellant used, i.e., heavier molecules require a higher bias voltage to obtain the same cathode current, see Figure 3.29b. Given the high molecular mass of I_2, this trend explains the excessively high cathode voltages required for iodine operation. A direct comparison is not possible because neither 30 mA as cathode current nor 7 sccm as gas flow could be realised with iodine as propellant. The cause of this phenomenon probably stems from the specific plasma environment preferring the creation of electrons for low ion masses. The ionisation energy rises with the atomic mass for the noble gases, which is inverse to the trend observed here and thus does not explain the phenomenon. Instead, a change in the plasma sheath between the insert and the plasma may be responsible for the observed trend. An altered ion saturation current (which scales with $\sqrt{1/m_i}$ [106]) provokes a change in the potential difference between insert and plasma, which also affects the thermionic and the plasma electron current. Further studies therefore have to verify the origin of this behaviour.

The differences in cathode voltage are also the main reason for the different sputtering rates observed for the different propellants. The lowest sputtering rate is observed when argon is used as propellant due to the low cathode voltage. However, when iodine is used, a very high sputtering rate is observed due to the high voltage used during operation. As discussed above, the sputter deposits on the relevant cathode parts are the main cause of performance degradation over time. The conservation or deterioration of performance is therefore also influenced by the choice of propellant, with argon showing the lowest deterioration of performance over time, whereas significant rates of deterioration are observed for krypton and especially iodine. No further propellant-specific wear effects were found in this work. These findings are particularly promising for the compatibility of iodine and C12A7:2e-.

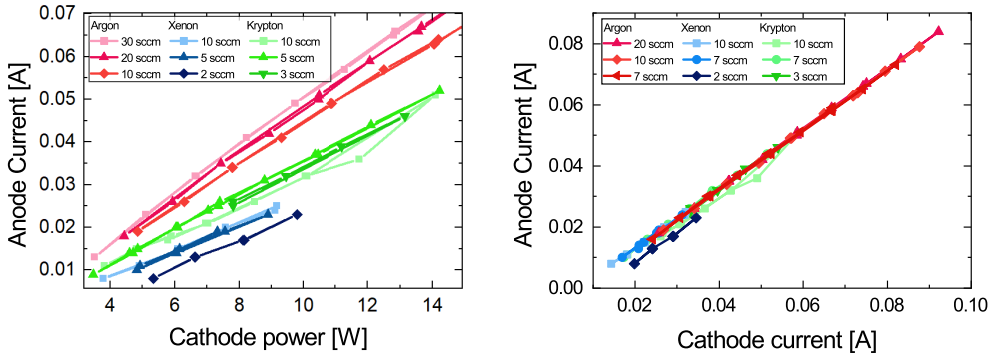

(a) *(b)*

Figure 3.28: Performance parameters for various gas flows and propellants: a) A detailed performance characterisation for the propellants argon, krypton and xenon for various mass flows. b) The I_A/I_C ratio, which describes the extraction efficiency.

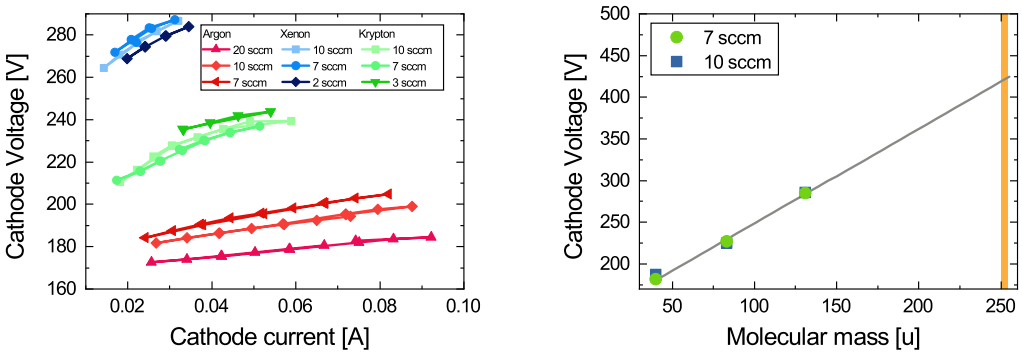

(a) *(b)*

Figure 3.29: NACES performance with the propellants argon, krypton, xenon and iodine: a) the U_C/I_C ratio b) the relationship between the cathode voltage required and the molecular mass of the propellant used. Values are obtained for I_C =30 mA and two different gas flows. A linear trend can be seen. The molecular mass of iodine is indicated in yellow.

3.3.4 Long term operation effects

The prolonged operation of a cathode is crucial for its use in a propulsion system. Identifying the degradation mechanisms of the device and insert and their effects on the operating parameters is therefore of great interest. Specifically, the effects of the degradation mechanisms on the $U_C(I_C)$ and $I_A(I_C)$ relations introduced earlier in this chapter are essential in this context. To address the above research questions, a 300 hour endurance test was performed with the NACES cathode. The test procedure is briefly outlined in the subsequent paragraph before the results are presented in the following paragraphs.

During the test, an anode extraction current of 20 mA was maintained, and the other operating parameters were adjusted accordingly. Krypton was used as propellant. Every 100 hours of operation, the test was interrupted and the device and the insert underwent inspection, and a material characterization of the insert was conducted. Table 3.1 displays the events and milestones of the endurance test and introduces key words for easy reference later in this thesis.

During the test a degradation of the device performance was observed, which will be discussed in detail later. The test campaign was therefore continued with an increased anode voltage (60 V instead of 20 V) and a reduced mass flow (3 sccm instead of 5 sccm). Despite these measures, the deterioration in performance continued during the subsequent test run. It was therefore decided to remove the insulating sputter layers after 200 hours of operation, which significantly improved the performance but did not stop the ongoing degradation. The test campaign was terminated after 300 hours of operation.

Visual inspection of the disk-shaped C12A7:2e- insert shows its degradation with increasing operating time, see Figure 3.30. White sputter deposits appear in the inner region and at the edge of the insert. Additionally, the typical circular sputtering pattern of the device above the embedded magnet is visible. The recess significantly deepens with operation time. After 300 hours of operation, a depth of up to 0.7 mm is measured (with 2 mm insert thickness) as shown in Figure 3.30e. The significant sputtering considerably limits the device's total lifetime.

As explained in Section 2.4.4, Raman spectroscopy is a simple and non-intrusive method to assess the quality of a C12A7:2e- sample. The peak area ratio Λ, determined from the spectrum, can be linked to the degree

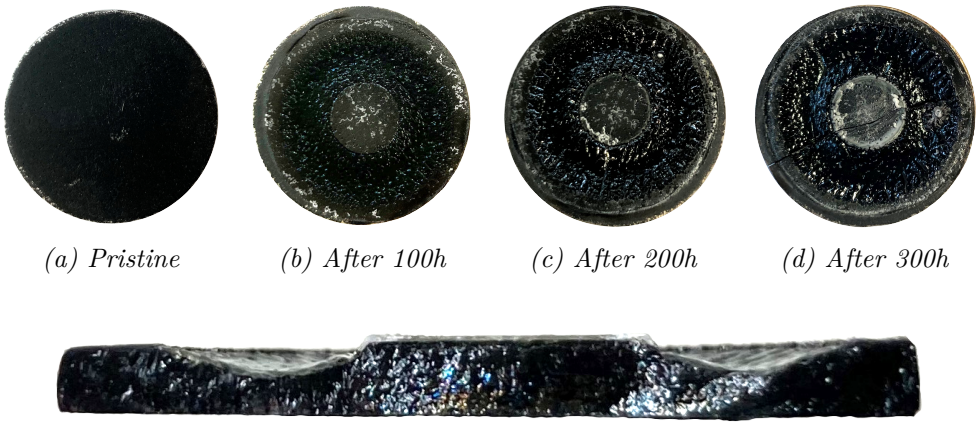

(a) Pristine *(b) After 100h* *(c) After 200h* *(d) After 300h*

(e) Side view after 300 hours

Figure 3.30: Insert degradation with operating time from (a) a uniform black pristine state to (d) a significant recess after 300 hours of operation. An increase in white sputter deposits is also visible. During Ins3 (keyword according to Table 3.1) the insert fractured along its diameter. A side view of the fractured edge is shown in e).

of reduction of the electride. Furthermore, based on the spectra it can be distinguished between (poly-)crystalline and amorphous, i.e. sputtered, phases of C12A7:2e- electride, as shown in Figure 3.31a. By employing Raman spectroscopy alongside cathode operation, the degradation process of the insert can be studied. Additionally, a series of spectra is collected along the disk radius to obtain a spatially resolved surface characterisation. An example is shown in Figure 3.31b. The different C12A7:2e- phases, i.e., amorphous or polycrystalline can be observed along the insert's radius. Also the development of the double peak around $600\,\mathrm{cm}^{-1}$ with respect to the single peak around $520\,\mathrm{cm}^{-1}$, characterised by the peak area ratio Λ can be studied. Figure 3.32 depicts the development of the spatially resolved peak area ratio Λ over the operating time. A pristine insert has a high peak area ratio with little deviation and no systematic drift along its radius. From the results presented in Section 2.4.5 a mean F^+ centre density of $7.8{\cdot}10^{20}\mathrm{cm}^{-3}$ can be calculated for this insert. Two distinct regions of the insert can be identified as the operation time increases, based on the Raman spectra. First, an amorphous region around the disk centre. Sputtered electride material re-condenses in its amorphous phase here. This region continues to expand with operating time as shown in Figure 3.32. The second region is composed of a polycrystalline electrode phase of high electride quality. This region roughly matches the observed

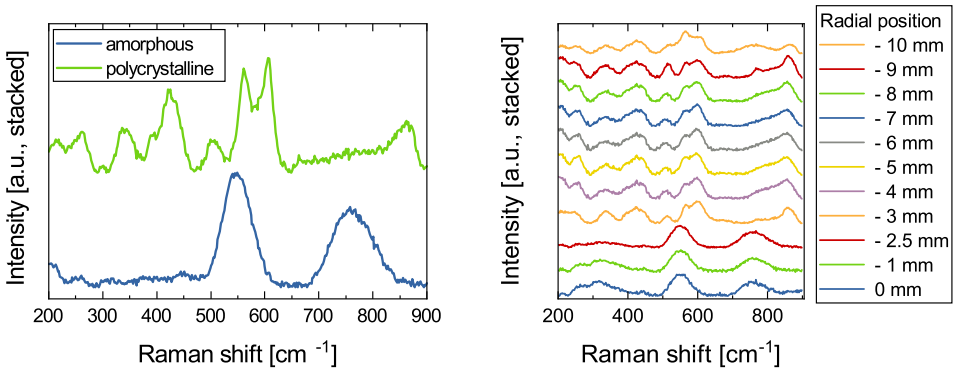

(a) *(b)*

Figure 3.31: a) Comparison of the Raman spectra of amorphous C12A7:2e- and polycrystalline C12A7:2e- of high quality. Two broad bands exist around 550 cm^{-1} and 750 cm^{-1} in the amorphous spectrum. The polycrystalline spectrum is dominated by a sharp double peak around 600 cm^{-1}. b) Raman spectra along the insert disk radius, exemplary after 200 hours of operation. Close to the center, Raman spectra indicative on amorphous C12A7:2e- are observed. Starting at 3 mm distance, polycrystalline phases are observed. The the intensity of the double peak around 600 cm^{-1} with respect to the single peak around 520 cm^{-1}, decreases with increasing radial position.

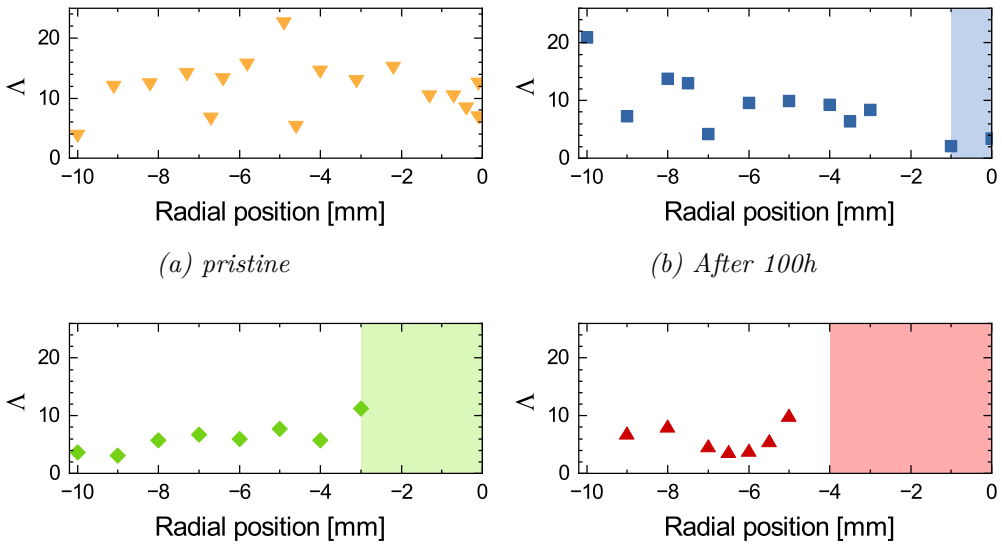

(a) pristine *(b) After 100h*

(c) After 200h *(d) After 300h*

Figure 3.32: Evolution of the peak area ratio Λ from Raman spectra with operating time. Raman spectra are taken at several points along the insert radius (radial position is given from the centre of the insert disk). The peak area ratio is then determined from the spectra as described in Section 2.4.4. The shaded areas indicate the amorphous region which spreads with the operating time.

(a) (b) (c)

Figure 3.33: Sputtered insert material on a) cathode cap (with insert in picture), b) keeper and c) anode at Ins1 (keyword according to Table 3.1).

sputtered structure[7]. With prolonged operation time, the peak area ratio in this region decreases, indicating a decrease in the degree of reduction of the electride. After 100 hours, a degree of reduction of $6.0{\cdot}10^{20}\mathrm{cm}^{-3}$, after 200 hours of $4.2{\cdot}10^{20}\mathrm{cm}^{-3}$, and after 300 hours of $3.8{\cdot}10^{20}\mathrm{cm}^{-3}$ is calculated. While a slight saturation in this value is noted, it is expected to further decrease with increasing time of operation. Notably, even after the extended operation time of 300 hours, the bulk material of the insert (exposed by continuous sputtering) is still of good quality and could still provide electrons in further test runs.

The key criterion for a cathode is its performance, usually characterised by its output current per power consumed. In Section 3.3.2 the general behaviour of the NACES cathode is described. In the following, the evolution of the three parameters contributing to the performance of the device, $U_C(I_C)$, $I_A(I_C)$ and $I_A(U_A)$ with operating time will be discussed.

The change in the $I_C(U_C)$ characteristics with operating time can be divided into three distinct contributions: a non-permanent effect, the insulating effect of the sputter deposits, and the degradation of the insert. First, the $I_C(U_C)$ relationship shows a non-permanent change with operating time, i.e., this effect disappears when the device is reignited after the inspection intervals. This effect significantly reduces the slope of the characteristics, see Figure 3.34a. The exact origin of this effect remains unclear. However, as this behaviour is similar to the observations in Section 3.2, a surface charge-up may also be responsible in this case. Second, the insulating effect of the sputtered electride layer. Visual inspection after prolonged operation shows significant deposition of sputtered material

[7]The centre of the insert used for the relative position was determined by hand for each characterisation interval. Deviations of approximately 1-2 mm appear plausible.

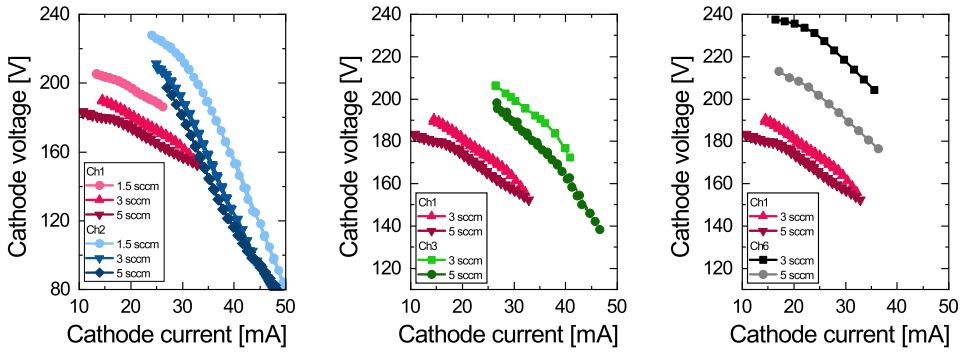

(a) *(b)* *(c)*

Figure 3.34: Cathode current-voltage characteristics showing the different influences on them during the endurance test: a) non-permanent effects, b) sputter deposits, c) insert wear. The corresponding keywords in the legends refer to Table 3.1.

on relevant parts such as the anode, keeper and cathode cap. Examples of the layers on these parts after 100 hours of operation are shown in Figure 3.33. Raman spectroscopy confirms the amorphous electride nature of these deposits. Amorphous electride is insulating, so the sputtered layer shields the potentials applied to these cathode parts. The lower effective potential must be counteracted by an increased input from the power supply to maintain a constant cathode current, see Figure 3.34b. Third, the wear of the electride insert. This wear is likely to be related to the preferential sputtering of aluminium in C12A7:2e-. Rutherford backscattering analysis of the sputtered deposits and the corresponding target material, carried out by a project partner, revealed a slight excess of Ca in the target material and additional Al in the complementary sputtered deposits. This imbalance of constituents in the target material will distort or even destroy the unique C12A7 crystal structure and impede the incorporation of electrons into the cages. The electron-deficient surface layer is measured by Raman spectroscopy as a reduced peak area ratio with operating time, see Figure 3.32. Due to the reduced electron emission capability of the surface, higher bias voltages are required to extract a continuous amount of electrons. After 200 hours of operation (and after cleaning all relevant parts from sputter deposits to distinguish between the effects of insert degradation and sputter deposits: Ev4 keyword according to Table 3.1) the cathode voltage required for a given cathode current is 20%-30% higher than in the initial configuration, see Figure 3.34c. Larger differences are also observed in the cathode voltage versus cathode current characteristics for different propellant mass flows.

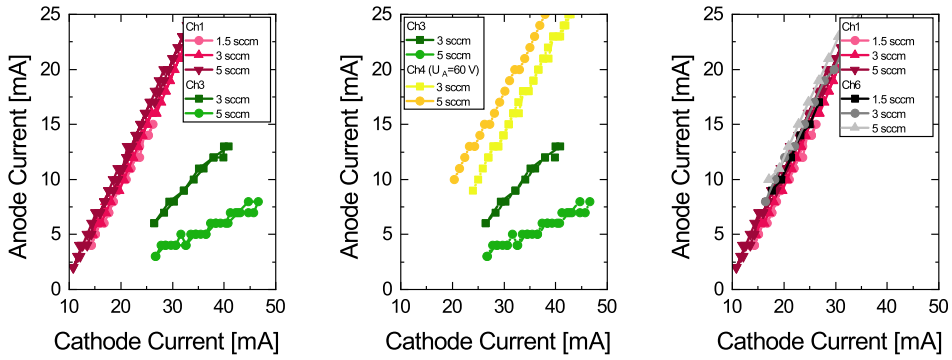

Figure 3.35: a) Change in $I_A(I_C)$ characteristics over 100 hours of operation for different gas flows. The key words in the legend are defined in Table 3.1 b) Effect of increasing the anode voltage from 20 V to 60 V: The anode current increases for a given cathode current, and the performance preference for higher/lower gas flows changes. c) Comparison of the $I_A(I_C)$ characteristics at the start (Ch1) and after removing sputter deposits (Ch6). The performance is recovered by cleaning.

The $I_A(I_C)$ characteristics are less affected by operational effects. Both the non-permanent increase and insert degradation observed for the $I_C(U_C)$ characteristics do not affect the $I_A(I_C)$ characteristics. Nevertheless, sputter deposits have a significant effect on the anode current obtained for a given cathode current. The shielding effect of sputter deposits can be seen in the ϵ factor introduced in Section 3.3.2 to describe the influence of anode voltage and gas flow on the $I_A(U_A)$ relationship. As discussed in the respective section, the value of ϵ depends on the anode voltage. The reduction of the effective anode potential by sputtering therefore reduces ϵ and thus the anode current for a given cathode current. The magnitude of the reduction is determined by the gas flow applied and will be discussed in the next paragraph. The b value of the $I_A(I_C)$ relationship decreases within the first 100 hours of operation, particularly at high gas flows it reaches a value close to 0. Expressing the deterioration in terms of the I_A/I_C ratio, it decreases from 0.69 to 0.24 during the first 100 hours of operation, see Figure 3.35a. Consequently, removal of the sputter deposits completely restores the original performance, as shown in Figure 3.35c. Increasing the anode voltage, in this case to 60 V, also increases the anode current as it counteracts the effects insulating sputtered layer, see Figure 3.35b.

In addition to the anode voltage, the gas flow also influences ϵ. Due to the different slopes of the $\epsilon(U_A)$ relation for different gas flows, the optimum gas flow depends on the voltage range. In the initial configuration,

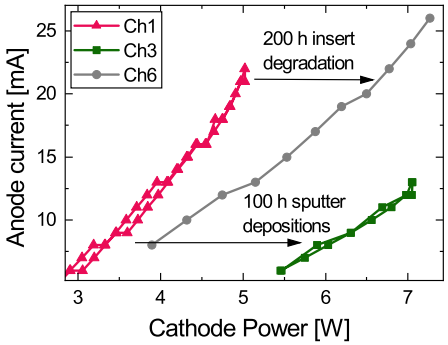

Figure 3.36: Influence of various long-term operating effects on the performance of the anode extraction current per cathode input power. Data taken for 3 sccm and 20 V anode voltage. Key words in the legend are defined in Table 3.1.

the effect of a change in gas flow is negligible, with a small preference for higher propellant flows. The system operates just above the intersection of the $\epsilon(U_A)$ curves of different gas flows. As the sputter deposits reduce the effective anode potential, the system shifts into the low voltage range of the $\epsilon(U_A)$ relationship with operating time. In this region, a reduced gas flow results in a higher ϵ value and thus a higher I_A/I_C ratio, as shown in Figure 3.35a. Increasing the anode voltage so that the effective anode potential is above the intersection point again favours a higher gas flow, see Figure 3.35b. After removal of the sputter deposits, the I_A/I_C ratio increases again slightly with the gas flow, see Figure 3.35c. It can therefore be concluded that the decrease in the I_A/I_C ratio and the changing behaviour with the gas flow are due to the reduction of the effective potentials in the device and not related to insert wear or operational effects such as surface charge-up.

In summary, several factors influence the performance of the NACES cathode on long time scales. The choice of operating parameters such as gas flow, cathode current and anode voltage results in different emission and extraction efficiencies. A non-permanent effect, probably a surface charge-up, was also observed. However, the key process to be considered is the sputtering of the C12A7:2e- insert, which results in two major effects: First, the degradation of the insert due to imbalanced sputtering of the different constituents. This particularly degrades the electron emission from the insert, leading to higher cathode voltage requirements. Insert degradation over 200 hours of operation increases the input power for a given anode current by 18% ($I_A = 10\,\mathrm{mA}$, Q=3 sccm) to 32% ($I_A = 20\,\mathrm{mA}$, Q=3 sccm), see Figure 3.36. The second is the deposition of the insulat-

ing electride material on relevant components. On the one hand, this reduces the potential enhancing electron emission from the insert, i.e. fewer electrons are generated. On the other hand, the electron extraction towards the anode is reduced. In total, accumulated sputter depositions of 100 hours operation increase the input power for a given anode current by 80% (I_A = 10 mA, Q=3 sccm), see Figure 3.36. The parameters for maximising performance also change with these increasing sputter deposits. Mitigation of insert sputtering is therefore imperative to maintain operability and performance over long time scales.

Key	Event Type	Time [h]	Remark
Ign1	Ignition	0	Initial ignition, start of endurance test
Ch1	Characterisation	2	
Ign2	Ignition	30	Re-ignition due to device extinction
Ch2	Characterisation	99	
Ins1	Inspection	101	Device inspection and insert characterisation after first test set
Ign3	Ignition	101.5	Re-ignition for second test set
Ch3	Characterisation	102.5	
Ev1		104	Increasing anode voltage to 60 V, and decrease propellant flow to 3 sccm
Ev2		133	Unplanned PC update, device probably still running, but no data-logging
Ev3		142	Restart software terminates discharge
Ign4	Ignition	142	Re-ignition due to device extinction
Ch4	Characterisation	144	
Ch5	Characterisation	214	
Ins2	Inspection	216	Device inspection and insert characterisation after second test set
Ev4		216	Removal of sputter deposits from cathode cap, keeper and anode
Ign5	Ignition	216	Re-ignition for third test set
Ch6	Characterisation	216	
Ign6	Ignition	228	Unstable operation with often extinctions and reignitions in the next 40 hours
Ch7	Characterisation	317	
Ins3	Inspection		Device inspection and insert characterisation after final test. Insert broke during extraction from device

Table 3.1: Events and milestones of the krypton endurance test of the NACES cathode. The keywords from the first column are used in this thesis to refer to specific events of the endurance test.

Chapter 4

Discussion and Conclusions

C12A7 possesses an exceptional crystal structure, featuring nano-sized cages that can serve as binding sites for anions. Incorporation of electrons results in the versatile C12A7:2e- electride, which has been investigated in this work. A common need for all applications of C12A7:2e- is a method-independent assessment of the material's reduction degree, which influences numerous application-relevant parameters.

In this work, four different characterization techniques were employed for studying a series of C12A7:2e- samples. Hall effect measurements allow one a detailed assessment of a sample's charge carrier density. However, the samples have to obey a certain height to diameter ratio and have to be contacted by sputter coating. This analysis cannot detect spatial inhomogeneities and averages over the entire sample. The oxidation technique is an easy way to determine the reduction degree of C12A7:2e-. As this technique relies directly on the incorporated electrons and no secondary property, few further assumptions have to be made during the subsequent analysis. However, this technique is destructive and can be applied only once per sample. Also a minimum sample volume is necessary to detect the minor weight gain. Attention has to be paid upon incorporation of oxygen species other than O^{2-}, which would influence the estimate for the reduction degree. The low oxygen partial pressure, which was used in this work, successfully inhibited incorporation of such other species and yielded a homogeneous oxidation of the specimen. The partial oxidation of a sample of known reduction degree allows one to synthesise a whole sample series in the intermediate reduction degree range which can then be used for further systematic analysis. Electron spin resonance spectroscopy measures the spin density of C12A7:2e-. Except in cases of spin-coupling, this quantity is also directly linked to encaged electrons in C12A7. As highly conductive samples, which are the ones relevant for application, shield in-

cident radiation, the samples have to be grinded, which makes this analysis also a destructive one. In the Raman spectra of C12A7 several bands were identified, that change in intensity gradually with the reduction degree. Furthermore, a shift in peak position was found for the band at $521\,\mathrm{cm}^{-1}$. This change was assigned to the relaxation of the surrounding cage when an electron replaces an anion. In this context, doped material would be of special interest. When aluminium is replaced by other species, this would also modify the vibration in the AlO_4 tetrahedron, which would confirm the assignment of the $521\,\mathrm{cm}^{-1}$ band. Raman spectroscopy is a non-destructive technique, which also allows for spatially resolved measurements. This makes it a versatile tool, in particular for accompanying measurements, like those presented in Chapter 3. A summary of the different characterization techniques with their properties, advantages and disadvantages in C12A7:2e- characterisation is given in Table 4.1.

The parameters determined by the four characterization techniques were correlated among another, whereby the charge carrier density obtained from Hall effect measurements and the reduction degree calculated from the weight gain during controlled oxidation were used as reference techniques. Both the spin density, determined by ESR spectroscopy, and the peak area ratio, calculated from Raman spectra, correlate to a high degree with the reference techniques. This proves, that also these material parameters allow an assessment of the reduction degree of C12A7:2e-. The analysis performed within this work allows one a method-independent assessment of the quality of a C12A7:2e- sample. By the correlations found here, results can be compared across different methods and the actual reduction degree can be derived. Thanks to the variety of methods presented, application specific choices for the preferred characterization technique can be made.

	Hall effect	Weight gain	ESR	Raman spectr.
Measured parameter	Charge carrier density	cage electrons	spin density	cage vibrations, peak area ratio
Relation to F+ density	power of 2	unknown	linear	linear
Sample preparation	contacting by sputter platinum	-	grind to powder	-
Sample usable after	no (platinum contacts)	no (oxidized)	no (powder)	yes
Spatially resolved	no	no	no	yes
Reference required	no	no	yes	yes
Advantages	• combined with mobility meas. gives insight on actual F+ centers	• sample series with various n_e can be synthesised	• small sample volume required	• Detection of secondary CA phases • spatial n_e mapping
Disadvantages	• constraints to sample geometry • strong magn. field required	• Other oxygen species cause systematic error	• conductive samples show Dyson effect • potential spin coupling at high n_e	• very sensitive to spatial inhomogeneities • assignment of bands difficult

Table 4.1: Comparison of characterisation techniques for C12A7:2e- electride samples.

When C12A7:2e- is used as insert in a thermionic plasma cathode, devices profit of the low work function of the material, which enables lower operating temperatures than state of the art materials. Two different designs were studied in this work to assess the operational behaviour and the performance of cathodes with C12A7:2e- inserts. The first design is a thermionic planar cathode, which, as the name states, uses thermionic emission from a heated, planar, i.e., disk-shaped insert to emit electrons. Over two iterations, a design was developed and improved based on experience from corresponding test campaigns. The effect of different orifice diameters on the performance of the device was analysed. Numerous tests performed with the second design version show the capability of reliable ignition and stable operation when pristine C12A7:2e- electride inserts are used. However, the insert condition strongly influences the stability of the required keeper voltage for a fixed current. A bulk related, permanent increase and a surface related non-permanent increase are identified. Further studies would be advantageous to verify the presented hypotheses. These experiments should include first test runs without an intermittent cool-down and subsequent test runs with a cool-down in between, to verify, that the observed non-permanent increase indeed originates from a surface layer, establishing due to cooling or reheating in between the tests. Mechanically cleaning the surface and performing another test would further verify the presented hypothesis. Accompanying Raman spectroscopy of the insert's surface and XRD spectroscopy with an instrument of higher sensitivity can identify the origins of these effects. However, additional experiments in the scope of this work were limited, due to the lack of additional pristine electride inserts. Identifying the origin of insert degradation mechanisms is key to develop mitigation strategies and adapt the device accordingly, so that the effect of design modifications can be studied or the performance optimised. Nonetheless, also in the context presented in this work, long term operation over several hours was demonstrated. In particular, a plasma bridge to the external anode was successfully established and current up to 0.4 A are provided by the cathode.

The second design studied in this work is the NACES cathode, also featuring a C12A7:2e- insert for electron emission. A major advantage of this design is its ability to ignite at room temperature, negating the need for an external heating element. The use of magnets significantly enhances ionisation, but also produces a characteristic sputtering pattern. Key performance indicators for the cathode are identified as the emission efficiency $U_C(I_C)$ and the extraction efficiency $I_A(I_C, U_A)$. These characteristics are

successfully used to study the effect of different input modes, propellants and long term performance. Four different propellants have been evaluated in this work for performance and operational stability. Argon exhibits the highest stability and performance of all the propellants studied, but also has the highest gas consumption. Both xenon and krypton have significant stability problems when no pulse box is in place and show poorer performance. Iodine requires even higher cathode voltages and no current extraction is possible due to low emission efficiency. However, apart from high voltage-related sputtering, no propellant-specific degradation effects were observed, especially not for iodine. The NACES cathode's stability was significantly enhanced with the use of a pulsed cathode voltage. For krypton, the average operational time increased from 30 minutes to tens of hours. A systematic study also indicated a significant improvement in emission efficiency. For extended operation times, a non-permanent surface charge-up and sputtering of the insert material were identified as degradation mechanisms. This sputtering caused both degradation of the insert and deposition of insulating layers on the anode, keeper and cathode, which severely degrade device performance. Similar results are also reported from project partners. Reducing sputtering is crucial to extend the operating time of the NACES cathode beyond 300 hours. A first mitigation strategy can be the use of a cylindrical anode instead of a planar one. Nonetheless, the persisting issue of sputter depositions on the keeper necessitates additional measures. Key to solve this problem is a reduction of the cathode voltage. This can be achieved by improving the emission capabilities of the insert, by increasing the operating temperature or by adjusting the cathode orifice. Omitting the magnet employed in order to achieve a more homogeneous plasma distribution could also be a possibility.

The high interest in C12A7:2e- as cathode material has also led to multiple development projects by other institutions. Both the Shanghai School of Mechanical Engineering and Exotrail reported of hollow cathode designs with electride inserts. Despite initial reports of insert melting by Exotrail, the recent results are promising. Extraction currents of several amperes can be obtained with a few hours of operation time for both designs. Operation durations longer than a few hours are pending. Dresden University of Technology and Airbus Defence and Space developed prototypes with a heaterless planar geometry. Operation with extraction currents up to 2 A is achieved. In particular the demonstrated operation time of almost 1000 hours of the design by Dresden University of Technology is an important milestone, regarding the typical lifetime requirements of space cathodes. Still, this design has a high propellant consumption and in both designs the insert (without added molybdenum, see below) was serious damaged by

melting after operation. Despite the higher sputtering yield of C12A7:2e- compared to the state of the art material LaB6, excessive sputtering was not reported elsewhere and seems to be an exclusive problem to NEMESIS project partners. Future studies have to show, whether this originates from disadvantageous operating parameters or material specific properties of the electride material supplied by ATD. The insulating nature of electride sputter deposits is in this context disadvantageous. However, the temperature induced damage to the insert still seems to be the major challenge for cathodes employing C12A7:2e-. Material optimisation offers huge potential to solve this problem. Already during the course of this work, the electride material has shown significant improvement, which is expected to continue in the future. Higher electrons densities lower the work function and enhance the electrical conductivity. The addition of molybdenum to the electride inserts as used at Dresden University of Technology significantly reduced melting during operation due to a higher thermal conductivity. Another approach is the use of single crystals where resistances (thermal and electrical) arising from grain boundaries are omitted. For the application in flight hardware the material also has show reproducible performance. With its complex crystal structure and the wide range of production techniques, a reliable quality assurance is required. This can be reached with the characterisation techniques presented above, in particular the non-intrusive Raman spectroscopy.

In summary, C12A7:2e- proves itself as a promising additional insert candidate, as it offers advantages to both state of the art materials. With its reported work function of 2.4 eV it lies between BaO-W and LaB6. The work function is the key criterion for the cathode's operating temperature, which determines power consumption and lifetime. The doping of the material is of particular interest in this regard. It could further reduce the work function, allowing it to compete with BaO-W. Also the ease of use seems to lie between that of BaO-W and LaB6 as it can be judged from the research performed so far: Electride has a significantly lower oxygen susceptibility than BaO-W, which facilitates test procedures and propellant requirements. Contrary, compared to LaB6 more caution has to be taken when using electride in cathodes due to its low melting point. In this intermediate region electride may establish itself as alternative to state of the art materials.

Appendix

A.1 Charge transport model

The properties of C12A7:2e- change drastically with the material's reduction degree, i.e., the number of F^+ centres where an electron replaces an oxygen anion. However, the most common material characterization techniques do not determine the reduction degree directly but measure related properties. Therefore, Dinter et. al used a combination of charge transport studies and EPR spectroscopy to model the actual F^+ centre density [18]. The following analysis is based on this work. It was found that three different transport mechanisms contribute to charge transport: Hopping transport with a temperature dependent mobility, delocalised transport with a constant mobility and surface transport. Hopping and delocalised transport is performed by electrons, that previously need to be excited to a higher state by E_{exc}. The charge carrier densities for these transports are described by the authors by the following formula:

$$n_{\mathrm{Hop}}(n_F) = \gamma \cdot n_F \exp\left(-\frac{E_{\mathrm{exc}}}{k_B T}\right) \tag{A.1}$$

$$n_{\mathrm{Del}}(n_F) = (1-\gamma) \cdot n_F \exp\left(-\frac{E_{\mathrm{exc}}}{k_B T}\right). \tag{A.2}$$

The key property, the F^+ centre density was determined by the authors from their measurements and their model. For the following analysis, the F^+ centre density of 8 samples presented in that report is extracted from Figure S2d). To obtain an expression for the charge carrier densities, that depends solely on n_F, also the excitation energy needs to be expressed in dependence of n_F. For this the publication was used again, in this case Figure 7a). However, in difference to the mentioned report, the excitation energy was not correlated with the effective charge carrier density n_{eff} but the F^+ centre density n_F. With a linear fit the following relation was extracted

$$E_{\mathrm{exc}}[\mathrm{eV}] = 1.09\,\mathrm{eV} - 0.052\,\mathrm{eV}\log\left(\frac{n_F}{\mathrm{cm}^{-3}}\right) \tag{A.3}$$

Internal name	Name in reference	n_F [cm^{-3}]
B1		$7.76938 \cdot 10^{19}$
B4	E1	$9.84749 \cdot 10^{19}$
B5		$1.04964 \cdot 10^{20}$
B8		$1.68624 \cdot 10^{20}$
B2	E2	$1.88117 \cdot 10^{20}$
B3		$1.92454 \cdot 10^{20}$
B7	E5	$2.90062 \cdot 10^{20}$
B6	E350	$9.70698 \cdot 10^{20}$

Table A.1: F^+ centre densities of the eight samples used for the approximations of E_{exc} and γ presented in this section. The sample names used in Ref. 18 are given for reference.

The same procedure was used to express γ, the ratio between hopping and delocalised conduction, in dependency of n_F. It also follows a linear relation with $\log(n_F)$

$$\gamma = -9.72 + 0.5 \log\left(\frac{n_F}{\text{cm}^{-3}}\right) \tag{A.4}$$

This yields the following expressions for n_{Hop} and n_{Del}

$$n_{\text{Hop}}(n_F) = \left(-9.72 + 0.5 \log\left(\frac{n_F}{\text{cm}^{-3}}\right)\right) n_F \exp\left(-\frac{\left(1.09\,\text{eV} - 0.052\,\text{eV} \log\left(\frac{n_F}{\text{cm}^{-3}}\right)\right) \cdot e}{k_B T}\right) \tag{A.5}$$

$$n_{\text{Del}}(n_F) = \left(10.72 - 0.5 \log\left(\frac{n_F}{\text{cm}^{-3}}\right)\right) n_F \exp\left(-\frac{\left(1.09\,\text{eV} - 0.052\,\text{eV} \log\left(\frac{n_F}{\text{cm}^{-3}}\right)\right) \cdot e}{k_B T}\right) \tag{A.6}$$

With these expressions the charge carrier densities for the two processes were calculated over a wide range of F^+ centre densities. The results are shown in section 2.4.5.

A.2 Data processing for ESR measurements

```
SetDirectory[NotebookDirectory[]];
BinaryType = "Integer32";
NumberFormEXP[x_] = NumberForm[DecimalForm[x], {40, 2}];

Lorentizan[A0_, s_, w0_, w_] =   A0/((w^2 - w0^2)^2 +
 ↪  s^2*w0^2);
DLorentizan[A0_, s_, w0_, w_] =   A0*D[1/((w^2 -
 ↪  w0^2)^2+s^2*w0^2), w];
SpectrolystFitFunction[A0_, s_, d_, w0_, w_] = A0*s^3*((-2*a
 ↪  + d*(s^2 - a^2)/s)/(s^2 + a^2)^2 + (-2*b - d (s^2 -
 ↪  b^2)/s)/(s^2 + b^2)^2) /. {a -> (w - w0), b -> (w +w0)}
 ↪  // FullSimplify;
Dysonian[A0_, s_, P_, w0_, w_] =  A0*(Cos[P]/s^2)*(-2 y + (1
 ↪  - y^2)*Tan[P])/(1 + y^2)^2 /. {y -> (w - w0)/s}(* See
 ↪  Rice et al. "Spin relaxation times of single-wall carbon
 ↪  nanotubes", DOI:10.1103/PhysRevB.88.041401 *);

RSpinRef = 5*10^(19)(* Spins / gramm - Weichpesche *);

Calculator2[directory_, {dataRef_, MassReff_},
 ↪  {dataSample_,MassSample_}, FilterValue_, RoundValue_,
 ↪  {{lSpec_, lConductive_}, lLorentz_, lDysonian_, w0x_}] :=
  Block[{dataRefSPC, dataRefPAR, DataPoints, i, Hmin, Hsweep,
   ↪  Hcenter, RecGainRef, Hvals, nlmfRef, IntNumericRef,
   ↪  TotalPowerNumericRef, TotalPowerAnalyticRef,
   ↪  dataSampleSPC, dataSamplePAR, RecGainSample,
   ↪  nlmfSample, IntNumericSample,
    TotalPowerNumericSample, TotalPowerAnalyticSample,
     ↪  solAnalytic,
    solNumeric, exp},

   dataRefSPC = BinaryReadList[StringJoin[directory, dataRef,
    ↪  ".SPC"], BinaryType, ByteOrdering -> +1];
   dataRefSPC = GaussianFilter[dataRefSPC, FilterValue];
   DataPoints = Length[dataRefSPC];
   dataRefPAR = Import[StringJoin[directory, dataRef,
    ↪  ".PAR"]];

   For[i = 1, i <= Length[dataRefPAR], i++,
    If[dataRefPAR[[i, 1]] == "GST", {
```

```
    Hmin = dataRefPAR[[i, 2]]
    }];
  If[(dataRefPAR[[i, 1]] == "HSW") \[Or] (dataRefPAR[[i,
  ↪  1]] ==        "HCF"), {
    If[(dataRefPAR[[i, 1]] == "HSW"), {
       Hsweep = dataRefPAR[[i, 2]]
       }, {
       If[(dataRefPAR[[i, 1]] == "HCF"), {
          Hcenter = dataRefPAR[[i, 2]]
          }];
       }];
    }];
  If[dataRefPAR[[i, 1]] == "RRG", {
    RecGainRef = dataRefPAR[[i, 2]]
    }];
  ];
 If[ValueQ[Hsweep], {
   Hvals = Table[Hmin + Hsweep/DataPoints*i, {i, 0,
   ↪  DataPoints}];
   }, {
   Hvals = Table[Hmin + (Hcenter - Hmin)*2/DataPoints*i,
   ↪  {i, 0, DataPoints}];
   }];

 dataRefSPC = Table[{Hvals[[j]], dataRefSPC[[j]]}, {j, 1,
 ↪  DataPoints}];
 If[lSpec, {
   If[lConductive, {
     nlmfRef = NonlinearModelFit[dataRefSPC,
      ↪  SpectrolystFitFunction[A0, s, d, w0, w] +
      ↪  SpectrolystFitFunction[14777.060207550643`,
      ↪  3.5092629357643834`, 0.08665895438054212`,
      ↪  3391.10916414116`, w], {{A0, 10^4}, {s, 50}, d,
      ↪  {w0, w0x}}, w];
     }, {
     nlmfRef = NonlinearModelFit[dataRefSPC,
      ↪  SpectrolystFitFunction[A0, s, 0, w0, w] +
      ↪  SpectrolystFitFunction[14777.060207550643`,
      ↪  3.5092629357643834`, 0.08665895438054212`,
      ↪  3391.10916414116`, w], {{A0, 10^4}, {s,
      ↪  50},(*d,*){w0, w0x}}, w];
     }]
```

```
  }
 ];
If[lLorentz, {
  nlmfRef = NonlinearModelFit[dataRefSPC,
     DLorentizan[A0, s, w0, w], {{A0, 10^4}, {s,100}, {w0,
      ↪  w0x}}, w];
  }
 ];
If[lDysonian, {
  nlmfRef = NonlinearModelFit[dataRefSPC, Dysonian[A0, s,
   ↪  P, w0, w], {{A0, 10^8}, {s,50}, P, {w0, w0x}}, w];
  }
 ];

Print[Show[ListLinePlot[dataRefSPC, PlotRange -> All,
↪  AspectRatio -> 1, Frame -> True, Axes -> False,
↪  GridLines -> Automatic, PlotStyle -> Thickness[0.01],
↪  FrameLabel -> {"\!\(\*SubscriptBox[\(B\),
↪  \(ext\)]\)[G]", "Intensity [a.u.]"}],
  Plot[nlmfRef[x], {x, Min[Hvals], Max[Hvals]}, PlotRange
   ↪  -> All, PlotStyle -> Orange], Epilog ->
   ↪  {Inset[Style["reference", GrayLevel[0.5], Bold,
   ↪  Italic, 20], {Min[Hvals] + (Max[Hvals] -
   ↪  Min[Hvals])/5, Max[dataRefSPC[[All, 2]]]*0.9}]}]];

IntNumericRef = Table[{Hvals[[i]], Sum[dataRefSPC[[j,
↪  2]]*Hsweep/DataPoints, {j, 1, i}]}, {i, 1,
↪  DataPoints}];

TotalPowerNumericRef = Sum[IntNumericRef[[j,
↪  2]]*Hsweep/DataPoints, {j, 1, DataPoints}];
TotalPowerAnalyticRef = Integrate[Integrate[nlmfRef[x],
↪  x], {x, Min[Hvals], Max[Hvals]}];

dataSampleSPC = BinaryReadList[StringJoin[directory,
↪  dataSample, ".SPC"], BinaryType, ByteOrdering -> +1];
dataSampleSPC = GaussianFilter[dataSampleSPC,
↪  FilterValue];
DataPoints = Length[dataSampleSPC];
dataSamplePAR = Import[StringJoin[directory, dataSample,
↪  ".PAR"]];
```

```
For[i = 1, i <= Length[dataSamplePAR], i++,
 If[dataSamplePAR[[i, 1]] == "GST", {
   Hmin = dataSamplePAR[[i, 2]]
   }];
 If[(dataSamplePAR[[i, 1]] == "HSW") \[Or]
  ↪  (dataSamplePAR[[i, 1]] == "HCF"), {
   If[(dataSamplePAR[[i, 1]] == "HSW"), {
      Hsweep = dataSamplePAR[[i, 2]]
      }, {
      If[(dataSamplePAR[[i, 1]] == "HCF"), {
         Hcenter = dataSamplePAR[[i, 2]]
         }];
      }];
   }];
 If[dataSamplePAR[[i, 1]] == "RRG", {
   RecGainSample = dataSamplePAR[[i, 2]]
   }];
 ];
If[ValueQ[Hsweep], {
  Hvals = Table[Hmin + Hsweep/DataPoints*i, {i, 0,
   ↪  DataPoints}];
  }, {
  Hvals =
    Table[Hmin + (Hcenter - Hmin)*2/DataPoints*i, {i, 0,
     ↪  DataPoints}];
  }];

dataSampleSPC = Table[{Hvals[[j]], dataSampleSPC[[j]]},
 ↪  {j, 1, DataPoints}];
If[lSpec, {
  If[lConductive, {
    nlmfSample = NonlinearModelFit[dataSampleSPC,
     ↪  SpectrolystFitFunction[A0, s, d, w0, w], {{A0,
     ↪  10^5}, {s, 100}, {d, 0.1}, {w0, w0x}}, w];
    }, {
    nlmfSample = NonlinearModelFit[dataSampleSPC,
     ↪  SpectrolystFitFunction[A0, s, 0, w0, w], {{A0,
     ↪  10^5}, {s, 100}(*,{d, 0.1}*), {w0, w0x}}, w];
    }]
  }
 ];
If[lLorentz, {
```

```
  nlmfSample = NonlinearModelFit[dataSampleSPC,
   ↪  DLorentizan[A0, s, w0, w], {{A0, 10^4}, {s, 100},
   ↪  {w0, w0x}}, w];
  }
 ];
If[lDysonian, {
  nlmfSample = NonlinearModelFit[dataSampleSPC,
   ↪  Dysonian[A0, s, P, w0, w], {{A0, 10^5}, {s, 50}, {P,
   ↪  -0.1}, {w0, w0x}}, w];
  }
 ];

Print[Show[ListLinePlot[dataSampleSPC, PlotRange -> All,
↪  AspectRatio -> 1, Frame -> True, Axes -> False,
↪  GridLines -> Automatic, PlotStyle -> Thickness[0.01],
↪  FrameLabel -> {"\!\(\*SubscriptBox[\(B\),
↪  \(ext\)]\)[G]", "Intensity [a.u.]"}],
  Plot[nlmfSample[x], {x, Min[Hvals], Max[Hvals]},
   ↪  PlotRange -> All, PlotStyle -> Orange], Epilog ->
   ↪  {Inset[Style["Sample", GrayLevel[0.5], Bold, Italic,
   ↪  20], {Min[Hvals] + (Max[Hvals] - Min[Hvals])/5,
   ↪  Max[dataSampleSPC[[All, 2]]]*0.9}]}]];

Print[nlmfSample["ParameterTable"]];

IntNumericSample = Table[{Hvals[[i]],
↪  Sum[dataSampleSPC[[j,2]]*Hsweep/DataPoints, {j, 1,
↪  i}]}, {i, 1, DataPoints}];

TotalPowerNumericSample = Sum[IntNumericSample[[j,
↪  2]]*Hsweep/DataPoints, {j, 1, DataPoints}];
TotalPowerAnalyticSample =
↪  Integrate[Integrate[nlmfSample[x], x], {x, Min[Hvals],
↪  Max[Hvals]}];

solNumeric = Solve[(TotalPowerNumericSample/
↪  RecGainSample)/ (TotalPowerNumericRef/RecGainRef) ==
↪  a, a];
exp = Floor[Log10[(a*RSpinRef*MassReff/MassSample) /.
↪  solNumeric[[1, 1]]]];
```

```
   Print[Style[StringJoin["From numeric calculation:   ",
    ↪  ToString[
    ↪  Round[(a*RSpinRef*MassReff/MassSample)*10^(-exp) /.
    ↪  solNumeric[[1, 1]], RoundValue]], "*10^(",
    ↪  ToString[exp], ") spins/g"], Bold, 20]];

   solAnalytic = Solve[(TotalPowerAnalyticSample/
    ↪  RecGainSample)/(TotalPowerAnalyticRef/RecGainRef) ==
    ↪  a, a];
   exp = Floor[Log10[(a*RSpinRef*MassReff/MassSample) /.
    ↪  solAnalytic[[1, 1]]]];
   Print[Style[StringJoin["From analytic calculation:  ",
    ↪  ToString[Round[(a*RSpinRef*MassReff/MassSample)*10^(-exp)
    ↪  /. solAnalytic[[1, 1]], RoundValue]], "*10^(",
    ↪  ToString[exp], ") spins/g"], Bold, 20]];

   ];

(*Example for execution of code with sample "14" with a
 ↪  weight of 0.0184 g and "WP" with a weight of 0.0107 g as
 ↪  reference. The Spectrolyst function is used for fitting
 ↪  and a peak center at a magnetic field of 3400 G is
 ↪  assumed.*)
Calculator["", {"WP", 0.0107}, {"14", 0.0184}, 0, 0.001,
 ↪  {{True, False}, False, False, 3400}]
```

A.3 Background substraction of Raman spectra

Import

```
FolderPath =  "C:\\Users\\Muster\\Documents\\Data";
SetDirectory[FolderPath];
Files = FileNames[ "*" <> ".txt"]
NumberOfFiles = Length[Files]
Data = DataNames = Table[0, NumberOfFiles];

For[i = 1, i <= NumberOfFiles, i++,
 Data[[i]] =  Import[Files[[i]], "Table", IgnoreEmptyLines -> True,
      Numeric -> True, NumberPoint -> ".", HeaderLines -> 1];
 DataNames[[i]] =  StringTake[Files[[i]], {1, StringPosition[Files[[i]],
          ".txt"][[1, 1]] - 1}];
```

```
];

config = Import[StringJoin["config_ BGC", ".dat"], "Table"]
(* The config file contains the following information: LowerLimit,
UpperLimit (defining the range in cm-1 of the BGC), ScaleBGC
(how close the signal is fitted), RelevantLetter1 to RelevantLetter4
(describing where the relevant sample information is found in filename)*)
```

Background Correction

```
LowerLimit = config[[1, 2]];
UpperLimit = config[[2, 2]];
String1 = config[[4, 2]];
String2 = config[[5, 2]];
String3 = config[[6, 2]];
String4 = config[[7, 2]];

DataShort =  Table[Select[Data[[i]], LowerLimit < #[[1]]
     < UpperLimit &], {i, NumberOfFiles}];
ScaleBGC = config[[3, 2]];
     (*A value between 10 and 15 was used based on the dataset*)
BaseLine =  Table[EstimatedBackground[DataShort[[j, All, 2]], ScaleBGC],
     {j, 1,  NumberOfFiles}];
BGCIntensities =  Table[DataShort[[j, All, 2]] - BaseLine[[j]],
     {j, 1, NumberOfFiles}];
PlotBaseLine = Table[Partition[Riffle[DataShort[[i, All, 1]],
BaseLine[[i]]], 2], {i, 1, NumberOfFiles}];
BGCData = Table[Partition[Riffle[DataShort[[i, All, 1]],
       BGCIntensities[[i]]], 2], {i, 1, NumberOfFiles}];

ShowAll  = True;

ExportBGC =
  Table[ListLinePlot[{DataShort[[i]], PlotBaseLine[[i]],
     BGCData[[i]]}, Frame -> {True, True, True, True},
    FrameLabel -> {"Raman shift / \!\(\*SuperscriptBox[\(cm\),
    \\(-1\)]\)", "Intensity / arb. units", None, None}, PlotStyle ->
    Thick, PlotLabel ->   StyleForm [
      StringTake[DataNames[[i]], String1 ;; String2] <>
       StringTake[DataNames[[i]], String3 ;; String4], {"Times",
       10}], ImageSize -> Medium], {i, 1, NumberOfFiles}];
```

```
If[ShowAll ,
 ExportBGC,
 Manipulate[
  ListLinePlot[{DataShort[[i]], PlotBaseLine[[i]], BGCData[[i]]},
   Frame -> {True, True, True, True},
   FrameLabel -> {"Raman shift / \!\(\*SuperscriptBox[\(cm\), \(-1\)]\
\)", "Intensity / arb. units", None, None}, PlotStyle -> Thick,
   PlotLabel ->
    StyleForm [
     StringTake[DataNames[[i]], String1 ;; String2] <>
      StringTake[DataNames[[i]], String3 ;; String4], {"Times"}]], {i,
    1, NumberOfFiles, 1}
  ]
 ]
```

Export

```
NameExportFolder = FolderPath;
SetDirectory[NotebookDirectory[]];
DirExport = NameExportFolder;
If[DirectoryQ[DirExport], ,
  CreateDirectory[NotebookDirectory[] <> NameExportFolder]];
SetDirectory[DirExport];
Monitor[
 For [i = 1, i <= NumberOfFiles, i++ ,
  Export[DataNames[[i]] <> "_BGC" <> ".txt", BGCData[[i]], "Table"]
  ], ProgressIndicator[Dynamic[i], {1, NumberOfFiles}]]

ExportImages = False;
If[ExportImages,
 Monitor[
  For [i = 1, i <= NumberOfFiles, i++ ,
   Export[DataNames[[i]] <> "_BGC.png", ExportBGC[[i]],
    ImageResolution -> 200]
   ] , ProgressIndicator[Dynamic[i], {1, NumberOfFiles}]]
 ]
```

A.4 Technical drawings of the thermionic planar cathode

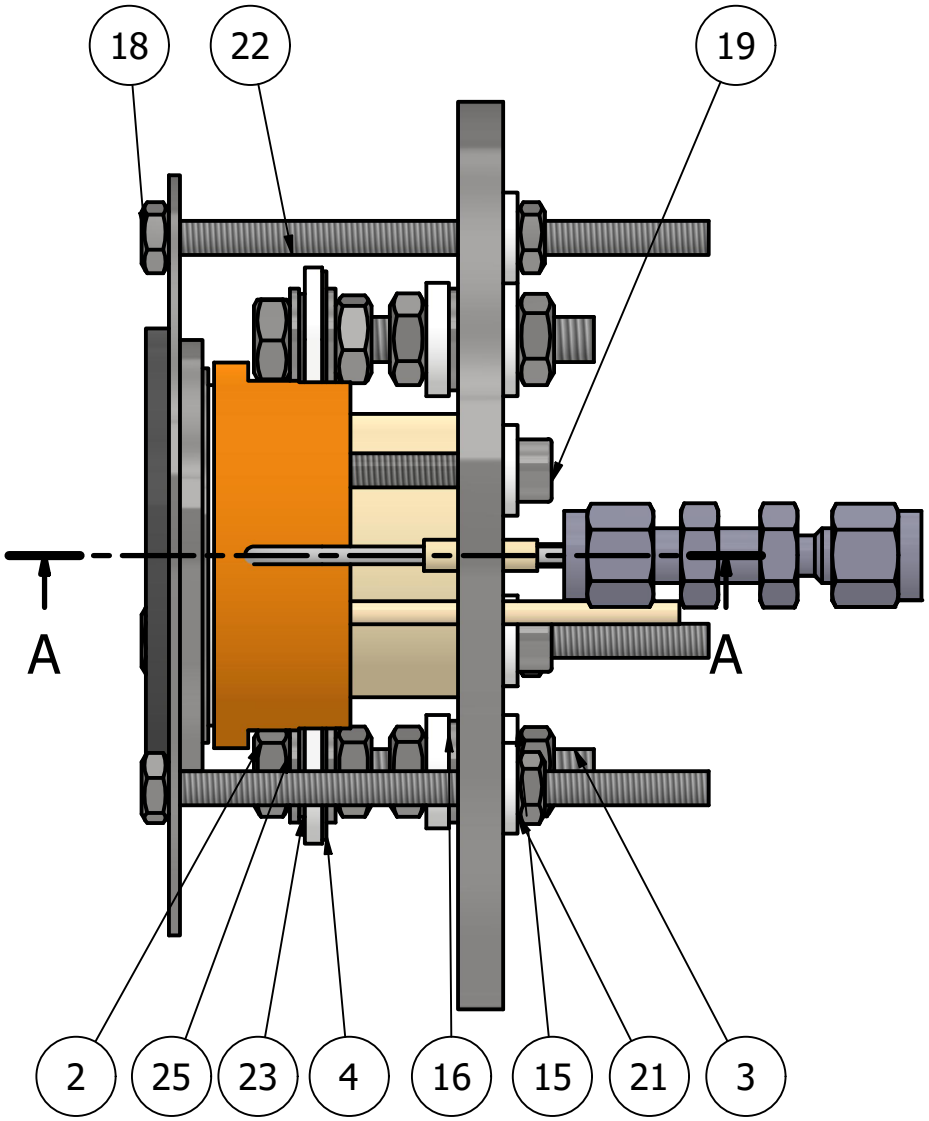

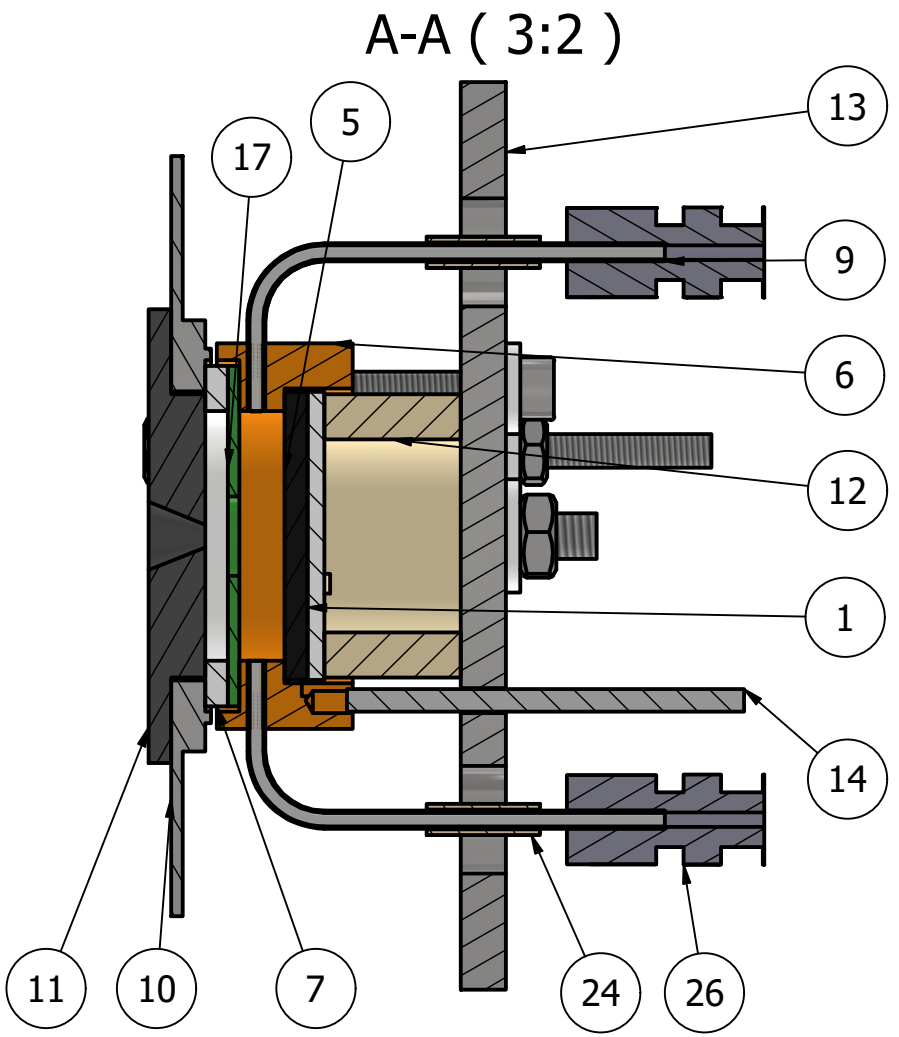

Designed by	Phone number	Allg. Toleranzen	Material	Date	
Malina	-33144	ISO 2768 -mK		24.08.2021	
		Projekt	Flachkathode V2		
		Flachkathode_v2-1	Scale 3:2	Sheet 1 / 2	

BAUTEILLISTE			
OBJEKT	ANZAHL	BAUTEILNUMMER	BESCHREIBUNG
1	1	Heizelement PCPBNP10	von ThermicEdge
2	8	ISO 4032 - M4(4)	Molybdän, vorhanden
3	2	Gewindestange M4	30 mm Länge, Molybdän, vorhanden
4	2	Unterlegscheibe Graphit M4x12	eigener Zuschnitt
5	1	C12A7:2e- Insert_flach	vorhanden
6	1	Kathode	
7	1	Keeper_Isolator	
9	2	Rohr 1/16"	vorhanden
10	1	Keeper	
11	1	Keeper_Einsatz	
12	1	Heizer_Unterbau	
13	1	Basisplatte	
14	2	Keramikröhrchen d=2mm	Röhrchen mit 2 Löchern
15	2	Isolator_Stufe_M4	
16	2	Isolator_Unterlegscheibe_M4	Al2O3, vorhanden
17	1	Kathode_orifice	
18	6	ISO 4032 - M3(4)	Sechskantmuttern, Typ 1 - Produktklasse A und B
19	2	ISO 4762 - M3 x 20(1)	Innensechskantschraube
20	3	ISO 2009 - M2 x 3(1)	Senkkopfschrauben mit Schlitz (Einheitskopf) - Produktklasse A
21	5	Isolator_Stufe_M3	vorhanden
22	3	Gewindestange M3	50 mm Länge
23	2	Unterlegscheibe Graphit M4x8	eigener Zuschnitt
24	2	Keramikröhrchen_einfach, d=2mm	Röhrchen mit einem Loch
25	6	ISO 7089 - 4	optional
26	2	Verschraubung_Gasleitung	vorhanden

Designed by	Phone number	Allg. Toleranzen	Material	Date	
Malina	-33144	ISO 2768 -mK		24.08.2021	
		Projekt	Flachkathode V2		
		Flachkathode_v2-1	Scale	Sheet	2 / 2

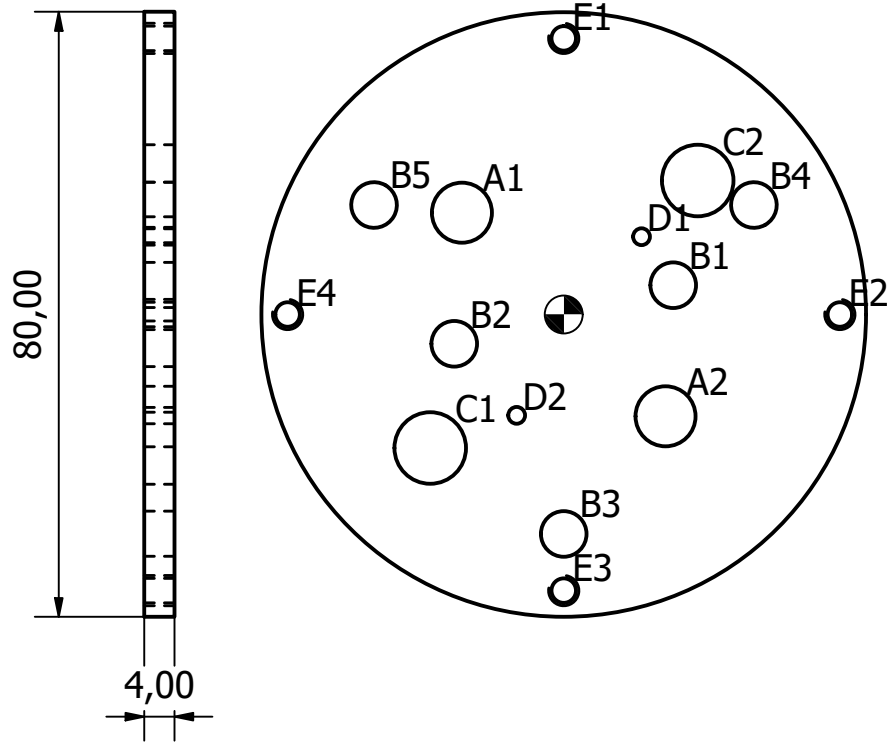

BOHRUNGSTABELLE			
BOHRUNG	XBEM	YBEM	BESCHREIBUNG
A1	-13,47	13,47	Ø8,00 DURCH
A2	13,47	-13,47	Ø8,00 DURCH
B1	14,49	3,88	Ø6,00 DURCH
B2	-14,49	-3,88	Ø6,00 DURCH
B3	0,00	-29,00	Ø6,00 DURCH
B4	25,11	14,50	Ø6,00 DURCH
B5	-25,11	14,50	Ø6,00 DURCH
C1	-17,68	-17,68	Ø9,50 DURCH
C2	17,68	17,68	Ø9,50 DURCH
D1	10,25	10,25	Ø2,20 DURCH
D2	-6,23	-13,37	Ø2,20 DURCH
E1	0,00	36,50	M4x0.7 - 6H
E2	36,50	0,00	M4x0.7 - 6H
E3	0,00	-36,50	M4x0.7 - 6H
E4	-36,50	0,00	M4x0.7 - 6H

Designed by	Phone number	Allg. Toleranzen	Material	Date	
Malina	-33144	ISO 2768 -mK	Edelstahl	25.08.2021	
		Projekt	Flachkathode V2		
		Basisplatte	Scale 1 : 1	Sheet 1 / 2	

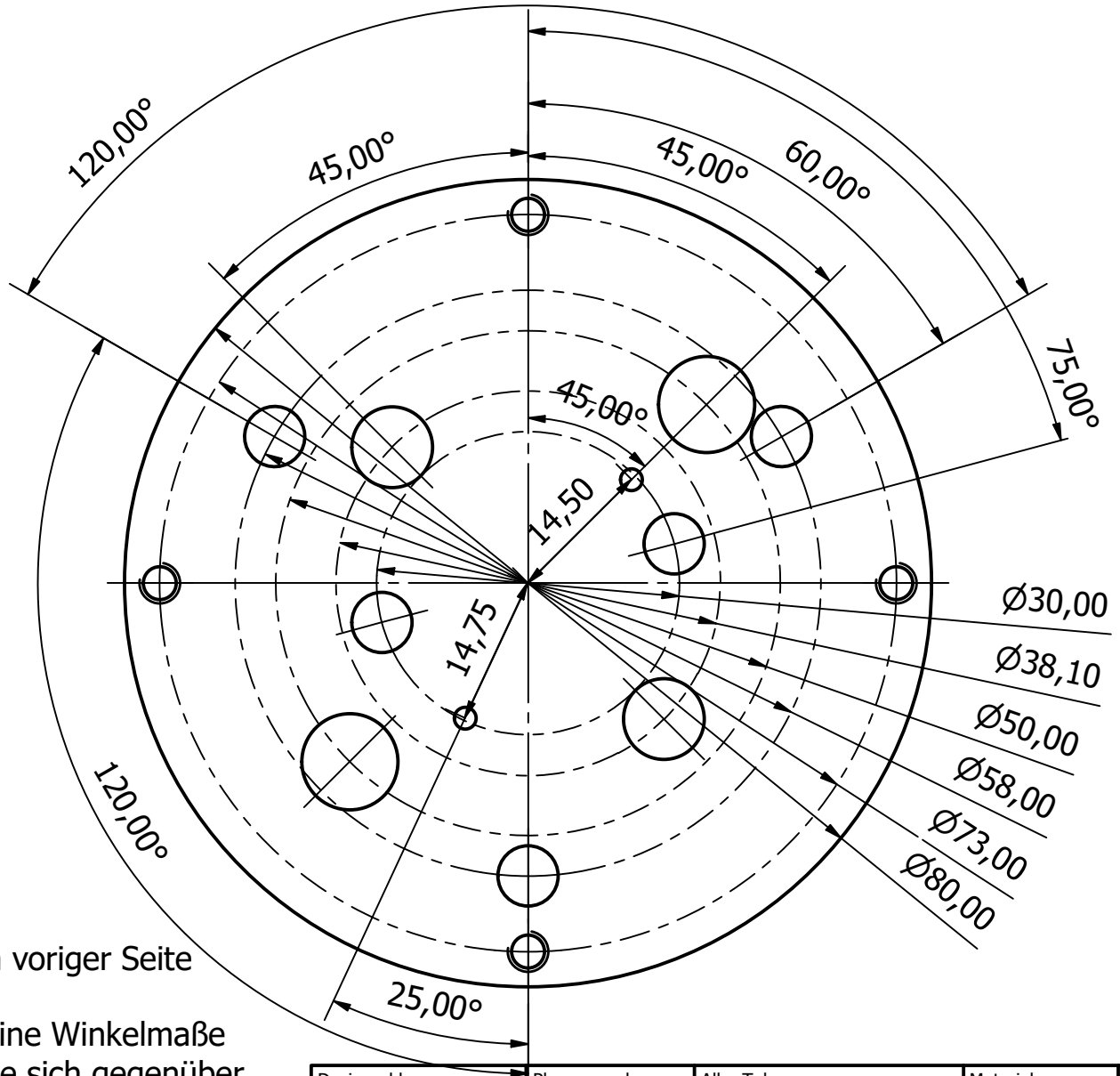

Lochdurchmesser nach voriger Seite

Sind bei Bohrungen keine Winkelmaße angegeben befinden sie sich gegenüber (180°) des anderen Loches auf dem Lochkreis

Designed by	Phone number	Allg. Toleranzen	Material	Date	
Malina	-33144	ISO 2768 -mK	Edelstahl	25.08.2021	
		Projekt: Flachkathode			
		Basisplatte	Scale: 3:2	Sheet: 2 / 2	

A-A (2 : 1)

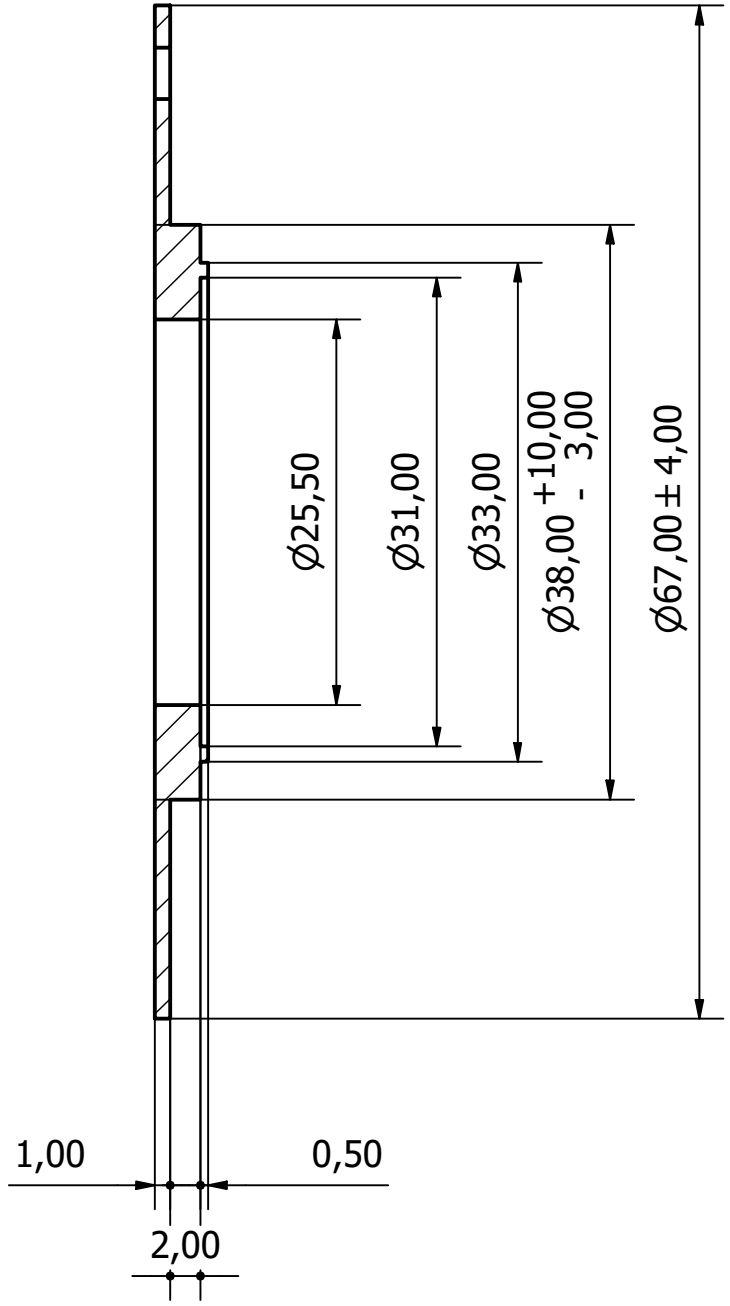

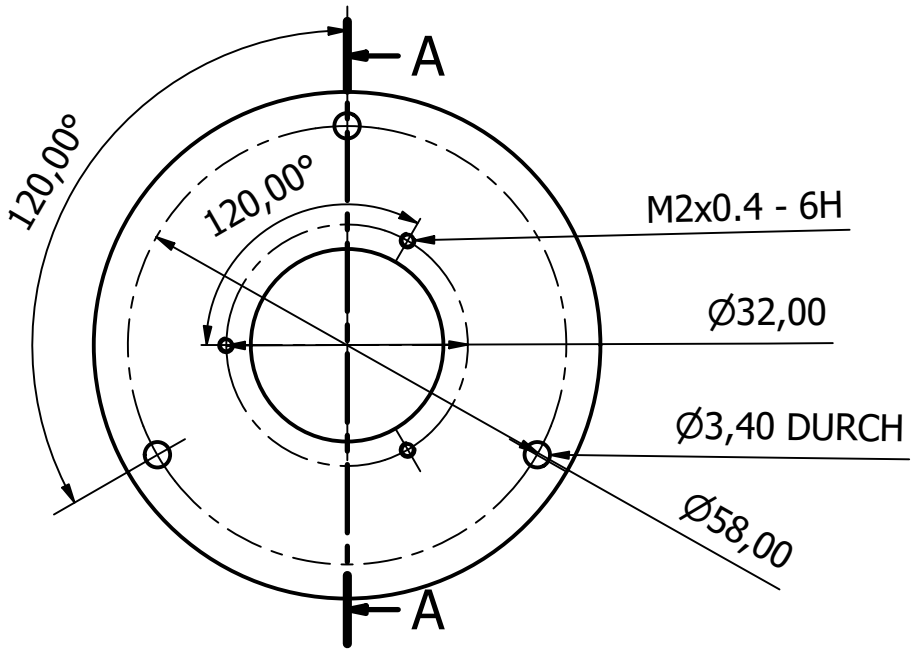

Winkel der M2 und M3 Bohrungen zueinander nicht relevant

Designed by	Phone number	Allg. Toleranzen	Material	Date	
Malina	-33136	ISO 2768 -mK	Edelstahl	25.08.2021	
JLU Gießen AG Ionentriebwerke		Projekt: Flachkathode V2			
		Keeper		Scale: 1 : 1	Sheet: 1 / 1

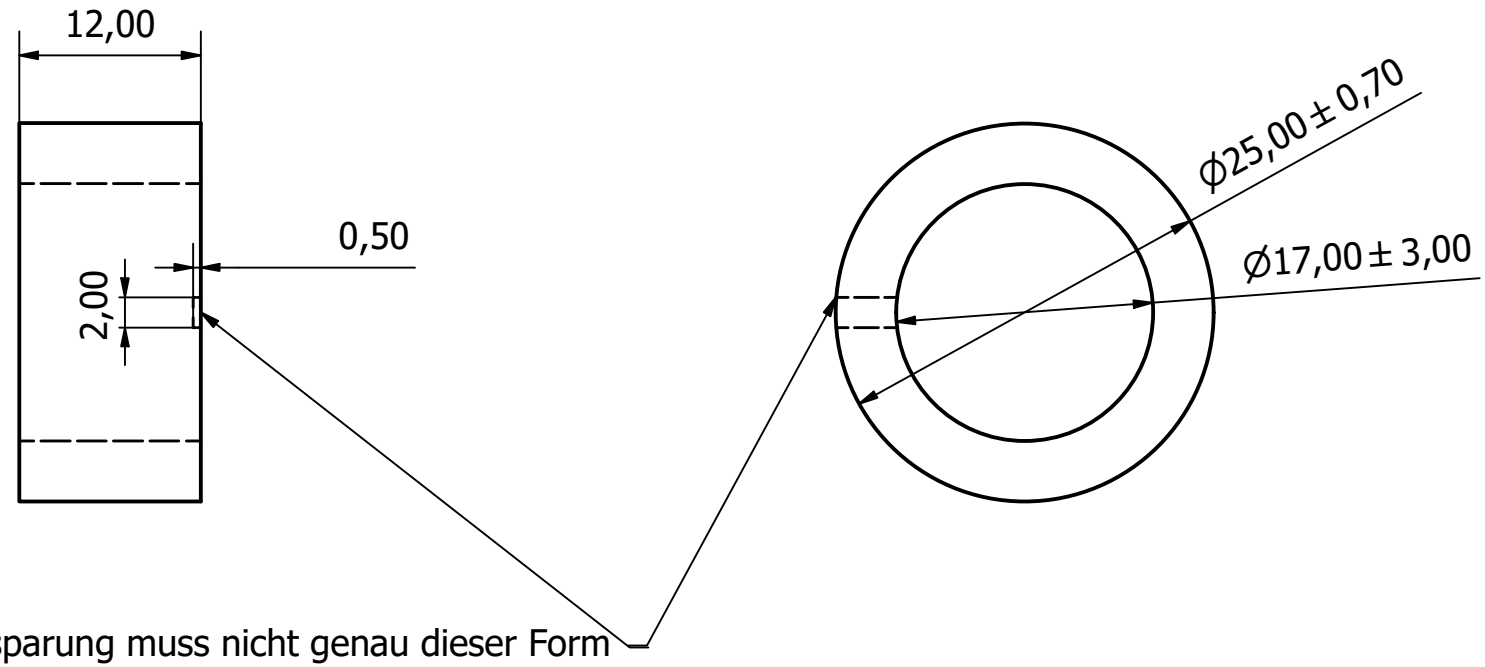

Aussparung muss nicht genau dieser Form entsprechen. Wichtig ist eine durchgehende Aussparung mit ca. 0,5 mm +- 0,1 mm Tiefe

Es sollten in der Feinmechanischen Werkstatt Keramikrohre mit einem Außendurchmesser von 25,0 mm +- 0,7mm vorhanden sein. Von diesen bitte ein entsprechendes Stück absägen

Designed by	Phone number	Allg. Toleranzen	Material	Date	
Malina	-33136	ISO 2768 -mK	Keramik	25.08.2021	
JLU Gießen AG Ionentriebwerke		Projekt: Flachkathode V2			
		Heizer_Unterbau	Scale: 2 : 1	Sheet: 1 / 1	

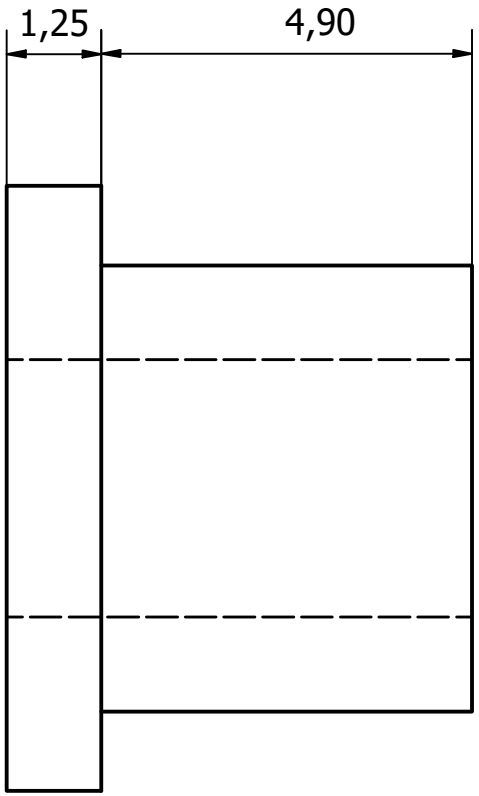

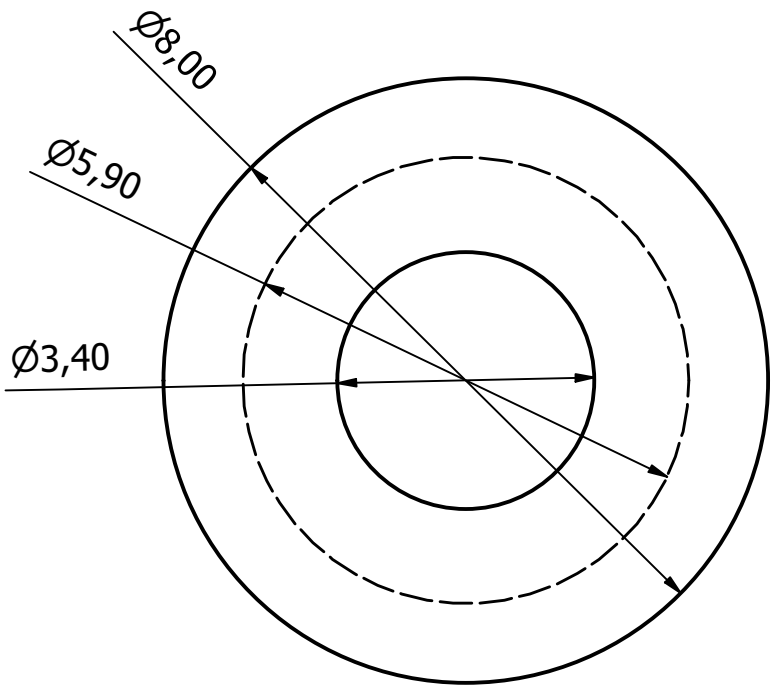

Stückzahl nach Stückliste

Designed by	Phone number	Allg. Toleranzen	Material	Date	
Malina	-33144	ISO 2768 -mK	Macor	06.08.2020	
		Projekt: Flachkathode			
		BN-Isolator_Stufe_M3	Scale: 10 : 1	Sheet: 1 / 1	

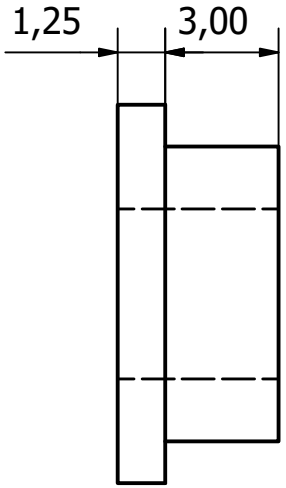

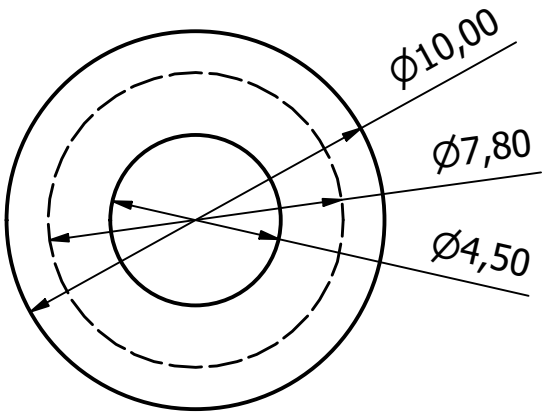

Designed by	Phone number	Allg. Toleranzen	Material	Date	
Malina	-33136	ISO 2768 -mK	Macor	25.08.2021	

JLU Gießen AG Ionentriebwerke	Projekt: Flachkathode V2		
	Isolator_Stufe_M4	Scale: 5 : 1	Sheet: 1 / 1

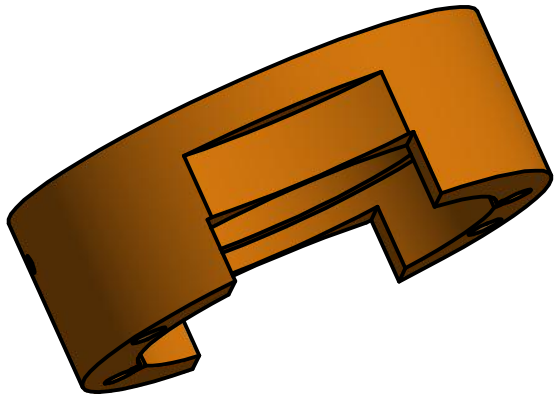

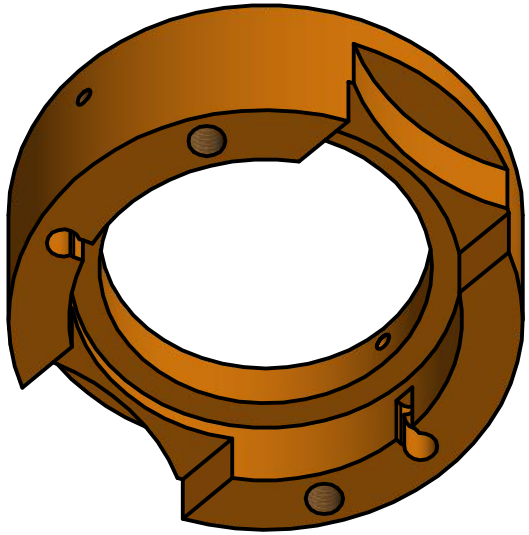

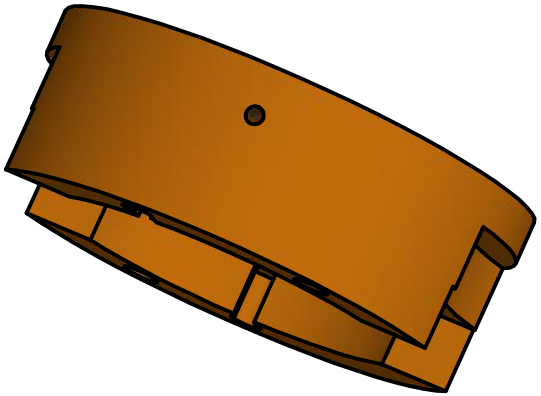

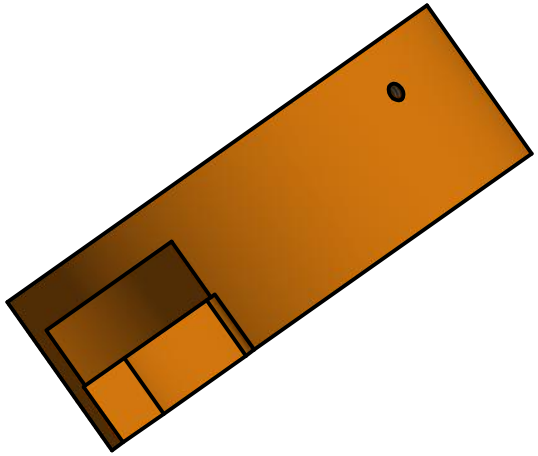

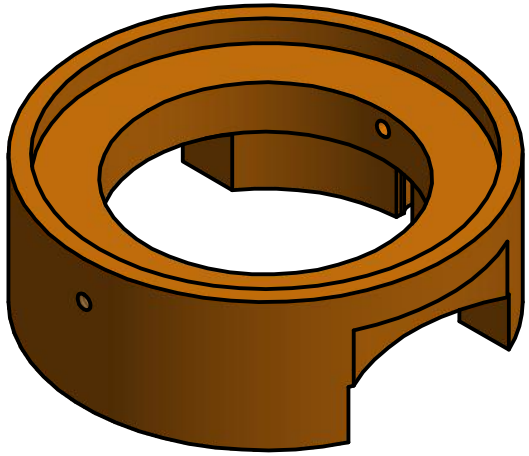

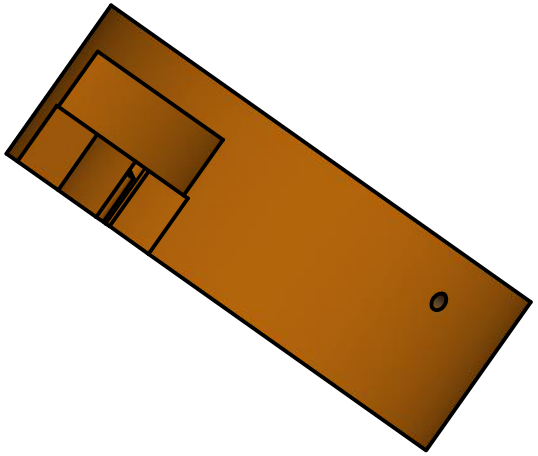

CAD-Datei per E-Mail übermittelt,
35mm Rundmaterial bestellt, wenn
benötigt bitte kurz anrufen

Designed by	Phone number	Allg. Toleranzen	Material	Date	
Malina	-33144	ISO 2768 -mK	Molybdän	24.08.2021	
		Projekt	Flachkathode V2		
		Kathode	Scale 2 : 1	Sheet 1 / 5	

Bereinigte Ansicht

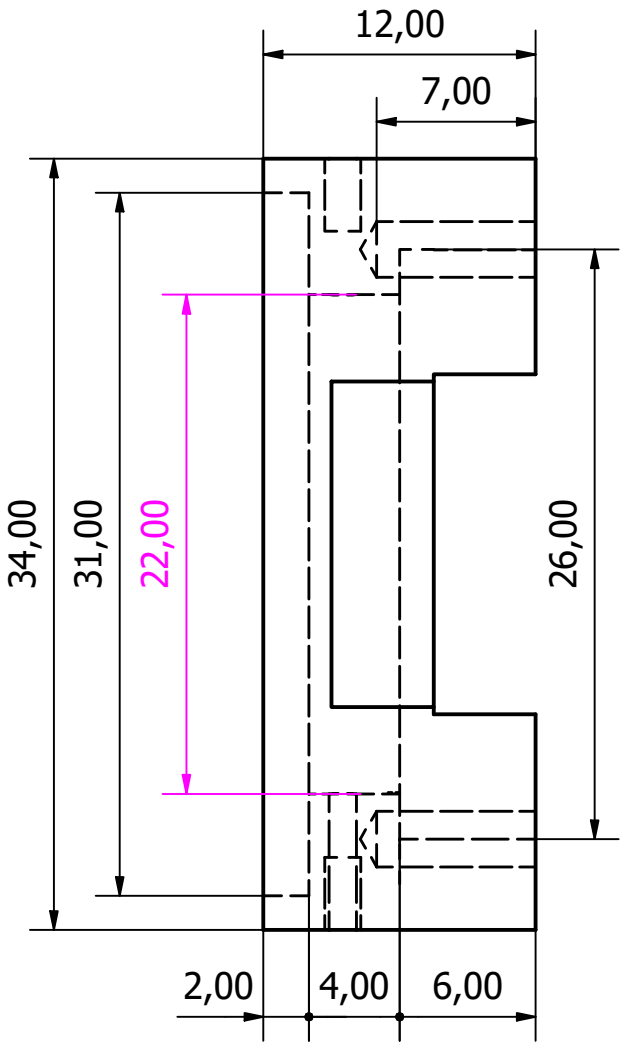

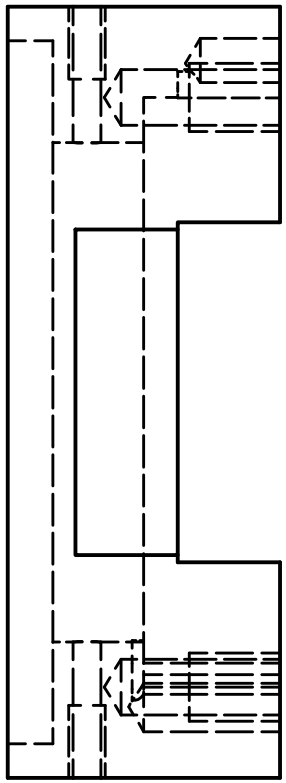

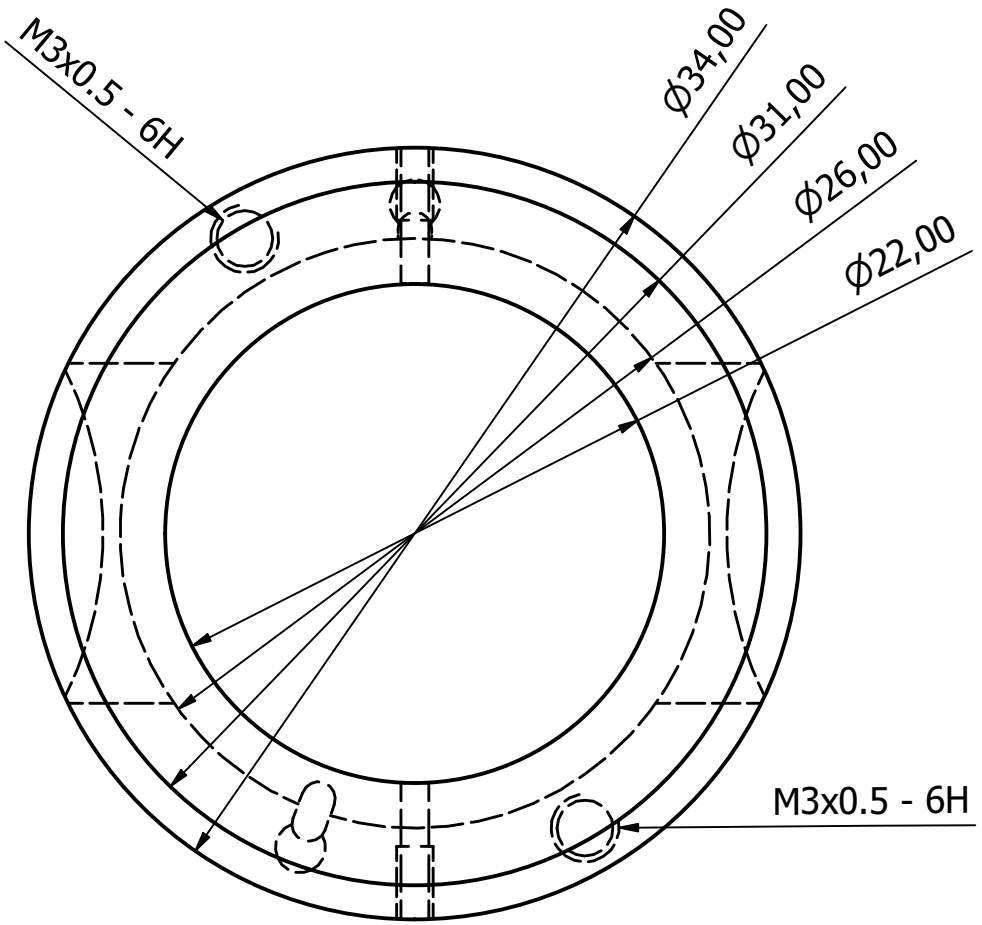

Designed by	Phone number	Allg. Toleranzen	Material	Date	
Malina	-33144	ISO 2768 -mK	Molybdän	24.08.2021	
		Projekt	Flachkathode V2		
		Kathode	Scale 3 : 1	Sheet 2 / 5	

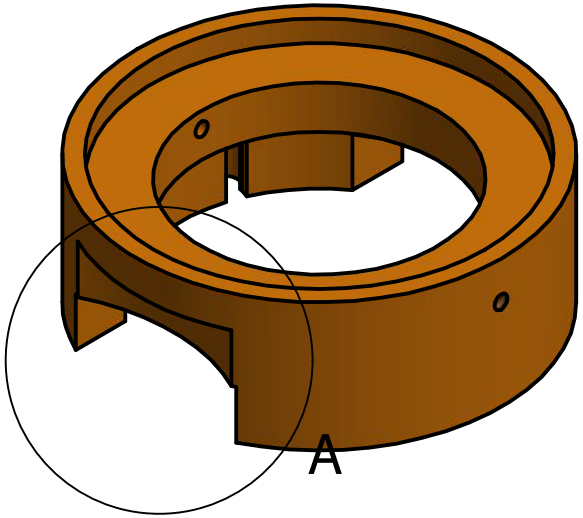

Ansicht von unten

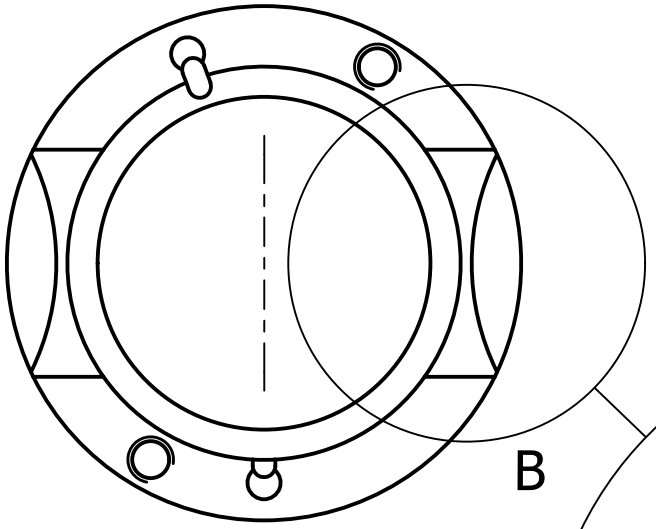

B (4 : 1)

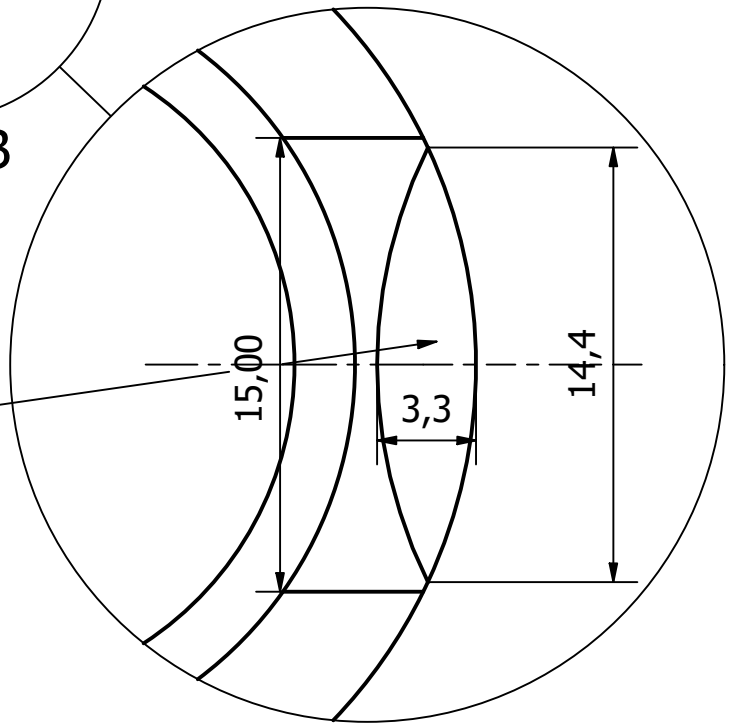

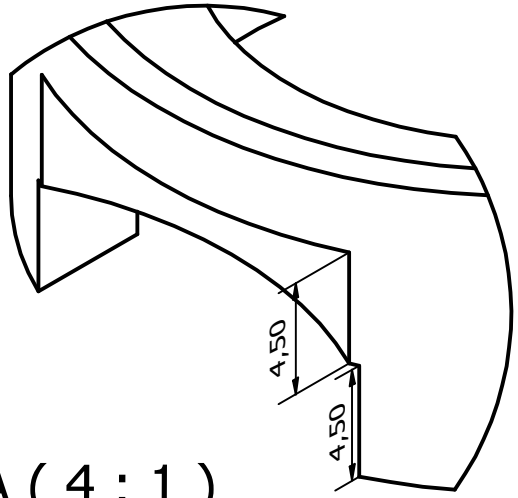

A (4 : 1)

Genaue Form der Aussparung nicht relevant, nur die angegebenen Maße sollten +- 0,2mm beachtet werden
Auch ein "Durchbruch" zur Aussparung mit 26mm Durchmesser ist nicht schlimm

Designed by	Phone number	Allg. Toleranzen	Material	Date	
Malina	-33144	ISO 2768 -mK	Molybdän	24.08.2021	
		Projekt	Flachkathode V2		
		Kathode	Scale 2 : 1	Sheet 3 / 5	

Ansicht von unten

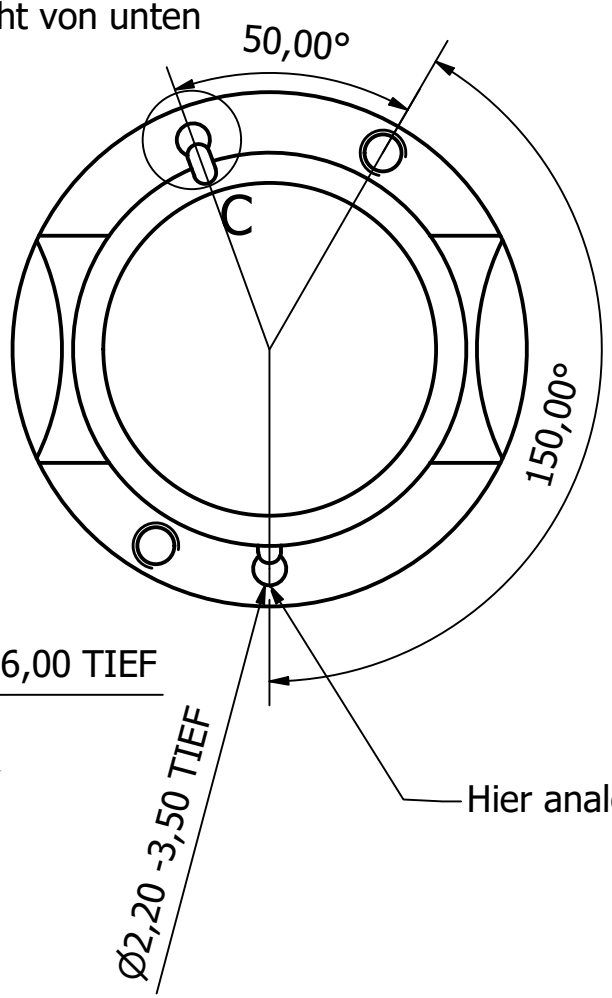

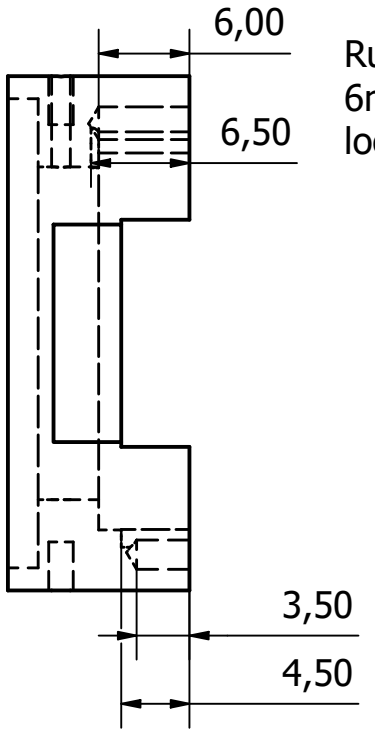

Runde Bohrung 6mm tief, Langloch 6,5mm tief

C (10 : 1)

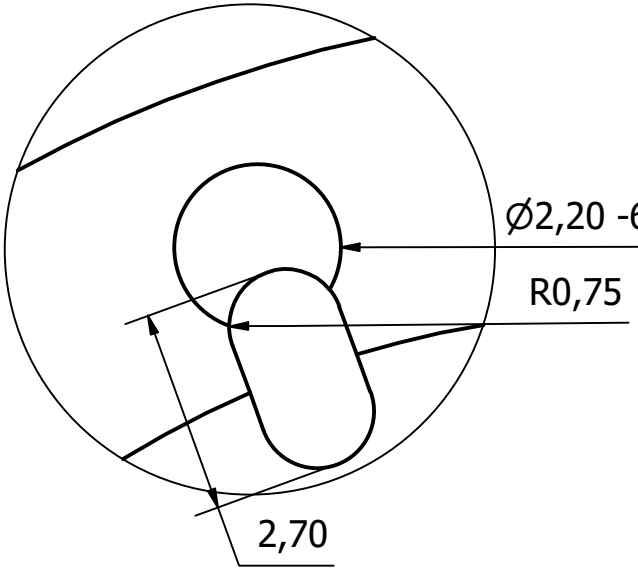

Hier analog zu Detailansicht C, nur weniger tief

Die Form hier muss nicht exakt rechteckig sein.
Es geht nur um eine längliche Aussparung, die bis zur Bohrung reicht

Designed by	Phone number	Allg. Toleranzen	Material	Date	
Malina	-33144	ISO 2768 -mK	Molybdän	24.08.2021	
		Projekt	Flachkathode V2		
		Kathode	Scale 2 : 1	Sheet 4 / 5	

Ansicht von oben

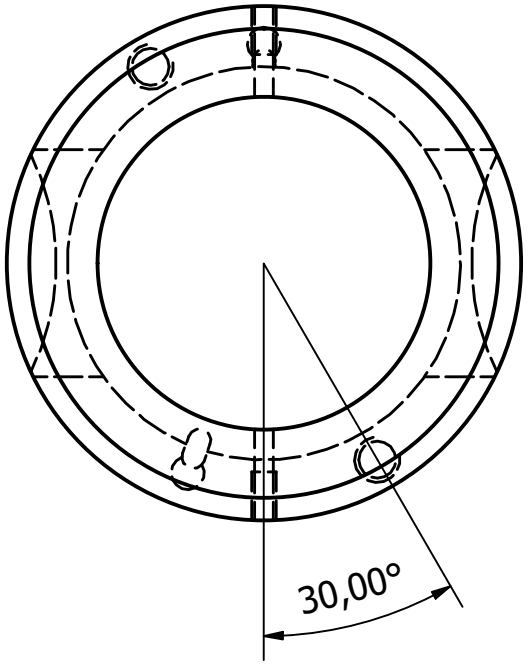

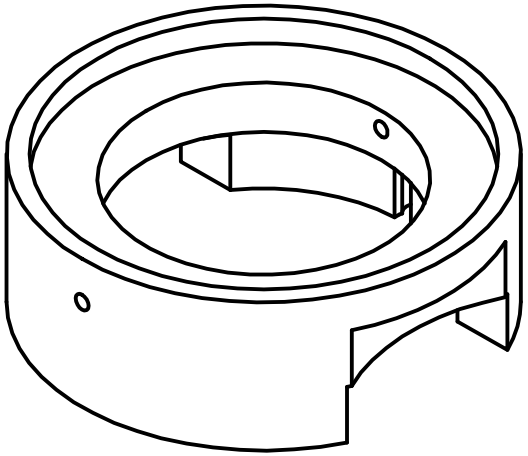

Bohrung auf der gegenüberliegenden Seite identisch

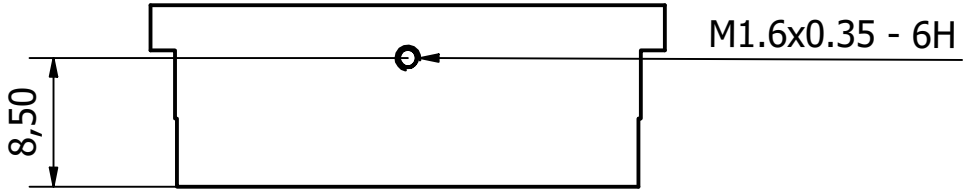

Designed by	Phone number	Allg. Toleranzen	Material	Date	
Malina	-33144	ISO 2768 -mK	Molybdän	24.08.2021	
		Projekt	Flachkathode V2		
		Kathode	Scale 2 : 1	Sheet 5 / 5	

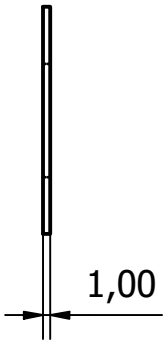

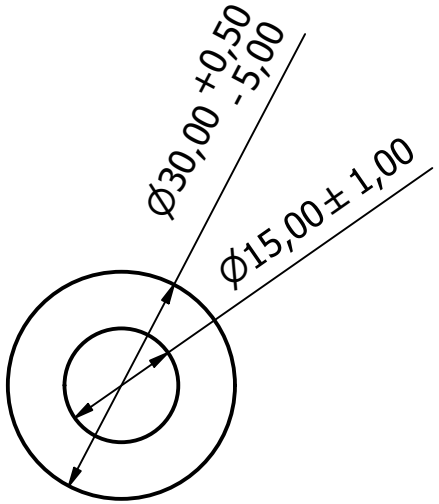

Dicke kann abhängig von der Materialverfügbarkeit auch bis zu 2mm betragen

Designed by	Phone number	Allg. Toleranzen	Material	Date	
Malina	-33136	ISO 2768 -mK	Molybdän	25.08.2021	
JLU Gießen AG Ionentriebwerke		Projekt: Flachkathode V2			
		Kathode_orifice	Scale: 1 : 1	Sheet: 1 / 1	

A-A (2 : 1)

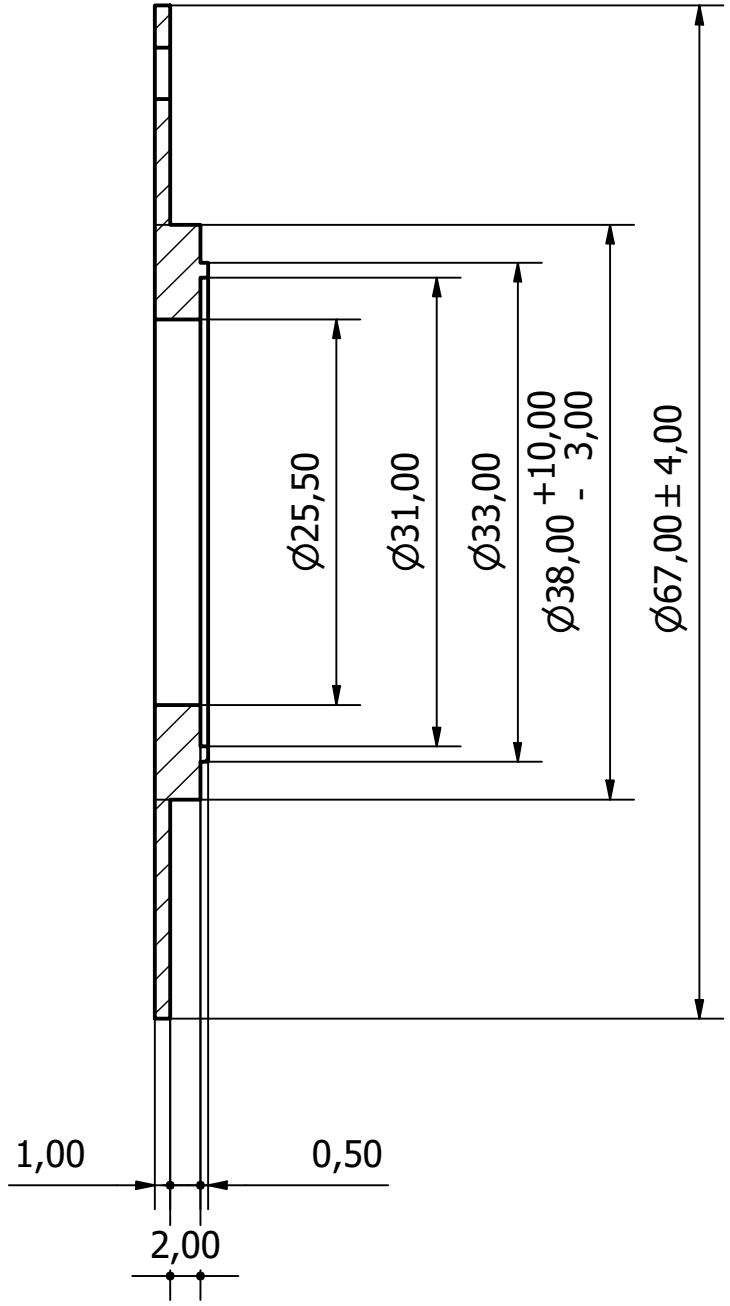

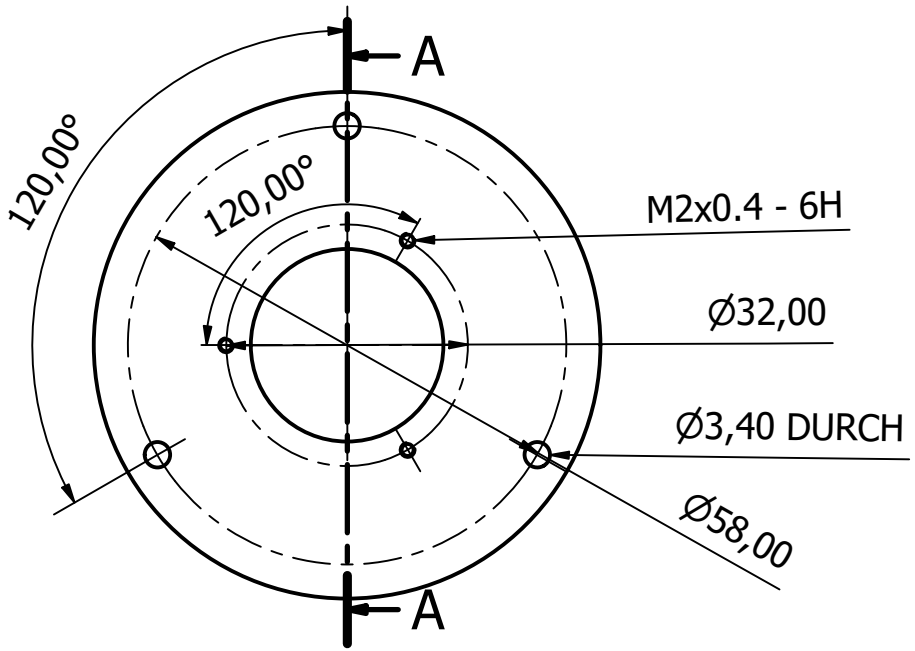

Winkel der M2 und M3 Bohrungen zueinander nicht relevant

Designed by	Phone number	Allg. Toleranzen	Material	Date	
Malina	-33136	ISO 2768 -mK	Edelstahl	25.08.2021	
JLU Gießen AG Ionentriebwerke		Projekt: Flachkathode V2			
		Keeper		Scale: 1 : 1	Sheet: 1 / 1

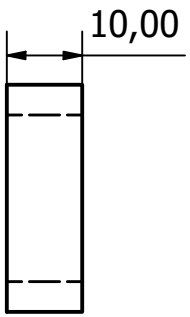

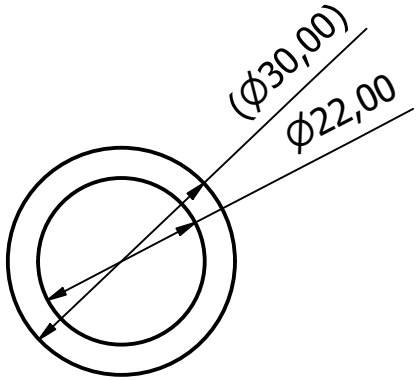

30mm Rundmaterial in AG Ionentriebwerke vorhanden, bitte unter Telefonnumer anrufen

Designed by	Phone number	Allg. Toleranzen	Material	Date	
Malina	-33136	ISO 2768 -mK	Bornitrid	25.08.2021	
JLU Gießen AG Ionentriebwerke		Projekt: Flachkathode V2			
		Keeper_Isolator		Scale: 1 : 1	Sheet: 1 / 1

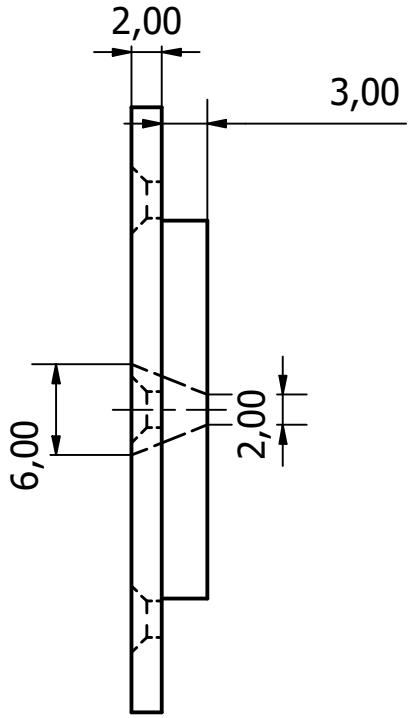

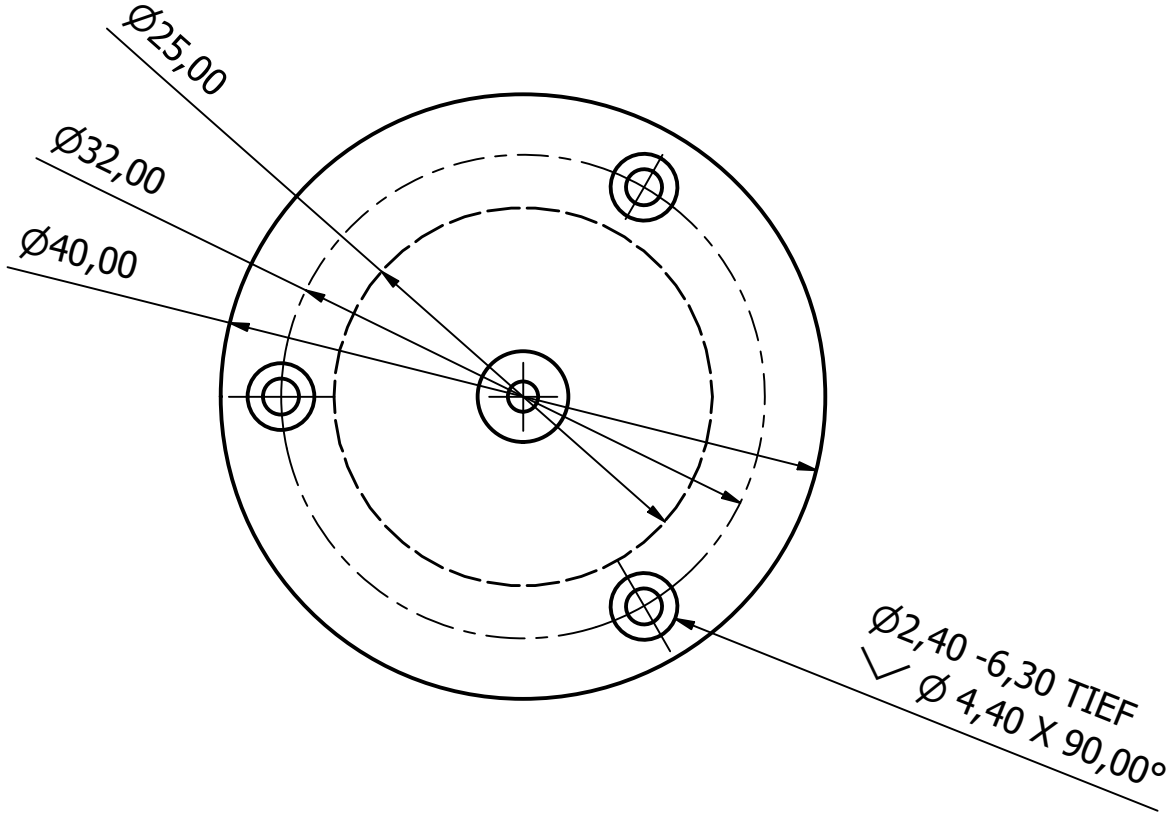

Designed by	Phone number	Allg. Toleranzen	Material	Date	
Malina	-33144	ISO 2768 -mK	Graphit	06.08.2020	
		Projekt	Flachkathode		
		Keeper_Einsatz	Scale 2 : 1	Sheet 1 / 1	

References

[1] I. F. M. Ahmed Rudwan and Steven Gabriel. "Investigation of the Discharge Characteristics of the T6 Hollow Cathode Operating on Several Inert Gases and a Kr/Xe Mixture". In: *AIP Conference Proceedings*. AIP, 2002, pp. 294–297. DOI: 10.1063/1.1593923.

[2] M. A. Ali and Yong-Ki Kim. "Ionization cross sections by electron impact on halogen atoms, diatomic halogen and hydrogen halide molecules". In: *Journal of Physics B: Atomic, Molecular and Optical Physics* 41.14 (2008), p. 145202. ISSN: 0953-4075. DOI: 10.1088/0953-4075/41/14/145202.

[3] M. Mozahar Ali et al. "Floating Zone Growth and Characterization of (Ca1-x Nd x)12Al14O33+6x (x $\sim$ 0.001) Single Crystals". In: *ACS omega* 1.6 (2016), pp. 1157–1163. DOI: 10.1021/acsomega.6b00409.

[4] Gabriel F. Benavides et al. "Iodine Hall-Effect Electric Propulsion System Research, Development, and System Durability Demonstration". In: *Joint Propulsion Conference*. [S.l.]: American Institute of Aeronautics and Astronautics, 2018. ISBN: 978-1-62410-570-8. DOI: 10.2514/6.2018-4422.

[5] Roland Benedix. *Bauchemie*. 3rd ed. Wiesbaden: Teubner, 2006. ISBN: 3519202263.

[6] Mariana I. Bertoni et al. "Tunable conductivity and conduction mechanism in an ultraviolet light activated electronic conductor". In: *Journal of Applied Physics* 97.10 (2005). ISSN: 0039-6028. DOI: 10.1063/1.1899246.

[7] Karl Wolfgang Böer. *Electronic transport in semiconductors*. 2. ed. Vol. Vol. 2. Survey of semiconductor physics / Karl W. Böer. New York, NY: Wiley, 2002. ISBN: 0471202789.

[8] H. Boysen et al. "Structure and oxygen mobility in mayenite (Ca12Al14O33): a high-temperature neutron powder diffraction study". In: *Acta crystallographica. Section B, Structural science* 63.Pt 5 (2007), pp. 675–682. ISSN: 0108-7681. DOI: 10.1107/S0108768107030005.

[9] John R. Brophy. “NASA’s Deep Space 1 ion engine (plenary)”. In: *Review of Scientific Instruments* 73.2 (2002), pp. 1071–1078. ISSN: 0034-6748. DOI: 10.1063/1.1432470.

[10] Manuel Cardona, ed. *Light scattering in solids*. Vol. 54. Topics in applied physics. Berlin: Springer, 1984. ISBN: 3540119426.

[11] F. Cervantes Lee and F. P. Glasser. “Powder diffraction data for compounds in the series Na x (Ca 3± x Na x)Al 2 O 6”. In: *Journal of Applied Crystallography* 12.4 (1979), pp. 407–410. ISSN: 0021-8898. DOI: 10.1107/S0021889879012826.

[12] A. Nørlund Christensen et al. “Neutron Powder Diffraction Profile Refinement Studies on Ca11.3Al14O32.3 and CaClO(D0.88H0.12)”. In: *Acta Chemica Scandinavica* 41a (1987), pp. 110–112. ISSN: 0904-213X. DOI: 10.3891/acta.chem.scand.41a-0110.

[13] Luis Conde. *D2.5 Report of NACES cathode report on endurance tests: Internal report of NEMESIS project*. URL: https://ec.europa.eu/research/participants/documents/downloadPublic?documentIds=080166e5f1ef39a0&appId=PPGMS.

[14] J.L Cronin. “Modern dispenser cathodes”. In: *IEE Proceedings I Solid State and Electron Devices* 128.1 (1981), p. 19. ISSN: 01437100. DOI: 10.1049/ip-i-1.1981.0012.

[15] John Dankanich et al. “The Iodine Satellite (iSat) Project Development through Critical Design Review (CDR)”. In: *Propulsion and Energy Forum*. [Place of publication not identified]: [publisher not identified], 2016. ISBN: 978-1-62410-406-0. DOI: 10.2514/6.2016-4540.

[16] Wolfgang Demtröder. *Experimentalphysik 3*. 4. überarb. Aufl. Springer-Lehrbuch. Berlin: Springer, 2010. ISBN: 978-3-642-03910-2.

[17] Wolfgang Demtröder. *Experimentalphysik 3: Atome, Moleküle und Festkörper*. 5. Aufl. 2016. Springer-Lehrbuch. Berlin, Heidelberg: Springer Berlin Heidelberg, 2016. ISBN: 9783662490945.

[18] Julius K. Dinter et al. “Identifying different electronic transport mechanisms in nanoporous inorganic electrides – a combined study using Hall measurements and electron paramagnetic resonance spectroscopy”. In: *Journal of Materials Chemistry C* (2023). ISSN: 2050-7526. DOI: 10.1039/d2tc05254g.

[19] Yingchao Dong, Hideo Hosono, and Katsuro Hayashi. “Formation and quantification of peroxide anions in nanocages of 12CaO · 7Al2O3”. In: *RSC Advances* 3.40 (2013), p. 18311. DOI: 10.1039/c3ra42521e.

[20] Christan Drobny, Jan-Philipp Wulfkühler, and Martin Tajmar. “Development of a C12A7 Electride Hollow Cathode and Joint Operation with a Plasma Thruster: IEPC-2019-629”. In: *36th International Electric Propulsion Conference IEPC*. 2019.

[21] Christan Drobny et al. “Detailed work function measurements and development of a hollow cathode using the emitter material C12A7 electride: SP2018_92”. In: *6th International Conference on Space Propulsion*. 2018.

[22] Christian Drobny, Martin Tajmar, and R. E. Wirz. “Development of a C12A7 Electride Hollow Cathode: IEPC-2017-373”. In: *35th International Electric Propulsion Conference IEPC*. 2017.

[23] D. V. Dukhopelnikov, S. O. Shilov, and D. K. Alekseev. “Comparison of the characteristics of the laboratory model of a anode layer thruster operating with krypton and xenon”. In: *XLIV ACADEMIC SPACE CONFERENCE: dedicated to the memory of academician S.P. Korolev and other outstanding Russian scientists – Pioneers of space exploration*. AIP Conference Proceedings. AIP Publishing, 2021, p. 040005. DOI: 10.1063/5.0036334.

[24] James L. Dye. “Chemistry. Electrons as anions”. In: *Science (New York, N.Y.)* 301.5633 (2003), pp. 607–608. DOI: 10.1126/science.1088103.

[25] Jose Fabian-Plaza et al. “Trade-off analysis of C12A7:e− deposition techniques applied to Low Work Function Tethers”. In: *Acta Astronautica* (2020). ISSN: 00945765. DOI: 10.1016/j.actaastro.2020.03.038.

[26] Nazareno Fazio et al. “Mission Cost for Gridded Ion Engines using Alternative Propellants: IEPC-2019-831”. In: *36th International Electric Propulsion Conference IEPC*. 2019.

[27] David Fearn and Stephen Patterson. “The Hollow Cathode - A Versatile Component of Electric Thrusters”. In: *ESA Journal* 465 (2000).

[28] W. Beall Fowler, ed. *Physics of color centers*. New York u.a.: Academic Press, 1968.

[29] Steven Gabriel. “Two-dimensional modelling of hollow cathodes with Krypton propellant: IEPC-2022- 148”. In: *37th International Electric Propulsion Conference IEPC*. 2022.

[30] Marcel P. Georgin, Benjamin A. Jorns, and Alec D. Gallimore. “An Experimental and Theoretical Study of Hollow Cathode Plume Mode Oscillations”. In: *35th International Electric Propulsion Conference IEPC*. 2017.

[31] Dan Goebel et al. “Hollow Cathode and Keeper-Region Plasma Measurements Using Ultra-Fast Miniature Scanning Probes”. In: *40th AIAA/ASME/SAE/ASEE Joint Propulsion Conference and Exhibit*. Joint Propulsion Conferences. Reston, Virigina: American Institute of Aeronautics and Astronautics, 2004. ISBN: 978-1-62410-037-6. DOI: 10.2514/6.2004-3430.

[32] Dan M. Goebel and Giulia Becatti. “High Current Hollow Cathodes for High Power Electric Thrusters: IEPC-2022-101”. In: *37th International Electric Propulsion Conference IEPC*. 2022.

[33] Dan M. Goebel and Ira Katz. *Fundamentals of electric propulsion: Ion and Hall thrusters*. Vol. 1. JPL space science and technology series. Hoboken, N.J: Wiley, 2008. ISBN: 978-0-470-42927-3. DOI: 10.1002/9780470436448.

[34] Dan M. Goebel, Ron M. Watkins, and Kristina K. Jameson. “LaB6 Hollow Cathodes for Ion and Hall Thrusters”. In: *Journal of Propulsion and Power* 23.3 (2007), pp. 552–558. ISSN: 0748-4658. DOI: 10.2514/1.25475.

[35] Dan M. Goebel and Ronald M. Watkins. “Compact lanthanum hexaboride hollow cathode”. In: *The Review of scientific instruments* 81.8 (2010), p. 083504. DOI: 10.1063/1.3474921.

[36] Dan M. Goebel et al. “Hollow cathode theory and experiment. I. Plasma characterization using fast miniature scanning probes”. In: *Journal of Applied Physics* 98.11 (2005), p. 113302. ISSN: 0039-6028. DOI: 10.1063/1.2135417.

[37] Norman Gondol and Martin Tajmar. “A volume-averaged plasma model for heaterless C12A7 electride hollow cathodes”. In: *CEAS Space Journal* (2022). ISSN: 1868-2502. DOI: 10.1007/s12567-022-00449-w.

[38] E. H. Hall. “XXIX. On a new action of the magnet on electric currents”. In: *The London, Edinburgh, and Dublin Philosophical Magazine and Journal of Science* 9.55 (1880), pp. 225–230. ISSN: 1941-5982. DOI: 10.1080/14786448008626828.

[39] Katsuro Hayashi et al. “Light-induced conversion of an insulating refractory oxide into a persistent electronic conductor”. In: *Nature* 419.6906 (2002), pp. 462–465. ISSN: 1476-4687. DOI: 10.1038/nature01053.

[40] Martin Henzler and Wolfgang Göpel. *Oberflächenphysik des Festkörpers*. Teubner Studienbücher Physik. Wiesbaden: Vieweg+Teubner Verlag, 1991. ISBN: 3-519-03047-0. DOI: 10.1007/978-3-322-96696-4.

[41] Klaus H. Herrmann. *Der Photoeffekt: Grundlagen der Strahlungsmessung*. Vieweg Lehrbuch praktische Physik. Braunschweig: Vieweg, 1994. ISBN: 3528064595.

[42] Kristof Holste et al. “Performance of an iodine-fueled radio-frequency ion-thruster”. In: *The European Physical Journal D* 72.1 (2018), pp. 1–7. ISSN: 1434-6079. DOI: 10.1140/epjd/e2017-80498-5.

[43] Hideo Hosono and Yoshihiro Abe. “Occurrence of superoxide radical ion in crystalline calcium aluminate 12CaO.7Al2O3 prepared via solid-state reactions”. In: *Inorganic Chemistry* 26.8 (1987), pp. 1192–1195. ISSN: 0020-1669. DOI: 10.1021/ic00255a003.

[44] Hideo Hosono et al. “Thin film and bulk fabrication of room-temperature-stable electride C12A7:e− utilizing reduced amorphous 12CaO · 7Al2O3(C12A7)”. In: *Journal of Non-Crystalline Solids* 354.19 (2008), pp. 2772–2776. ISSN: 0022-3093. DOI: 10.1016/j.jnoncrysol.2007.09.090.

[45] Qiao Hu et al. “Preparation and X-ray photoelectron spectroscopic characterization of Sn-doped C12A7:e− electride nanoparticles”. In: *Applied Surface Science* 508 (2020), p. 145244. ISSN: 01694332. DOI: 10.1016/j.apsusc.2019.145244.

[46] Zhiwei Hua et al. “Early experimental investigation of the C12A7 hollow cathode fed on iodine”. In: *Plasma Science and Technology* 24.7 (2022), p. 074004. ISSN: 1009-0630. DOI: 10.1088/2058-6272/ac4fb4.

[47] Jian Huang, Loredana Valenzano, and Gaurav Sant. “Framework and Channel Modifications in Mayenite (12CaO · 7Al 2 O 3) Nanocages By Cationic Doping”. In: *Chemistry of Materials* 27.13 (2015), pp. 4731–4741. ISSN: 0897-4756. DOI: 10.1021/acs.chemmater.5b01360.

[48] Siegfried Hunklinger. *Festkörperphysik*. 5. Auflage. De Gruyter Studium. Berlin and Boston: De Gruyter, 2018. ISBN: 9783110567748.

[49] Alexander L. Jehle. *Iodine Small Satellite Propulsion Demonstration - iSAT*. 2017. URL: https://digitalcommons.usu.edu/cgi/viewcontent.cgi?referer=&httpsredir=1&article=3696&context=smallsat.

[50] Dong Jiang et al. “Simple and Efficient Fabrication of Mayenite Electrides from a Solution-Derived Precursor”. In: *Inorganic chemistry* 56.19 (2017), pp. 11702–11709. DOI: 10.1021/acs.inorgchem.7b01655.

[51] Romain Joussot, Lou Grimaud, and Stéphane Mazouffre. “Examination of a 5 A-class cathode with a LaB 6 flat disk emitter in the 2 A–20 A current range”. In: *Vacuum* 146 (2017), pp. 52–62. ISSN: 0042207X. DOI: 10.1016/j.vacuum.2017.09.021.

[52] Romain Joussot et al. “Experimental and numerical investigations of a5A-class cathode with a LaB6flat disk emitter in the2A-20A current range: IEPC-2017-486”. In: *35th International Electric Propulsion Conference IEPC*. 2017.

[53] Koichi Kajihara et al. “Vibrational Dynamics and Oxygen Diffusion in a Nanoporous Oxide Ion Conductor 12CaO · 7Al 2 O 3 Studied by 18 O Labeling and Micro-Raman Spectroscopy”. In: *The Journal of Physical Chemistry C* 111.40 (2007), pp. 14855–14861. ISSN: 1932-7447. DOI: 10.1021/jp074248n.

[54] Sung Wng Kim and Hideo Hosono. “Synthesis and properties of 12CaO · 7Al 2 O 3 electride: review of single crystal and thin film growth”. In: *Philosophical Magazine* 92.19-21 (2012), pp. 2596–2628. ISSN: 1478-6435. DOI: 10.1080/14786435.2012.685770.

[55] Sung Wng Kim, Terumasa Shimoyama, and Hideo Hosono. “Solvated electrons in high-temperature melts and glasses of the room-temperature stable electride $Ca_{24}Al_{28}O_{64}{}^{4+} \cdot 4e^{-}$”. In: *Science (New York, N.Y.)* 333.6038 (2011), pp. 71–74. DOI: 10.1126/science.1204394.

[56] Sung Wng Kim et al. “Simple and efficient fabrication of room temperature stable electride: melt-solidification and glass ceramics”. In: *Journal of the American Chemical Society* 127.5 (2005), pp. 1370–1371. ISSN: 0002-7863. DOI: 10.1021/ja043990n.

[57] Sung Wng Kim et al. “Electron Carrier Generation in a Refractory Oxide 12CaO · 7Al 2 O 3 by Heating in Reducing Atmosphere: Conversion from an Insulator to a Persistent Conductor”. In: *Journal of the American Ceramic Society* 89.10 (2006), pp. 3294–3298. ISSN: 00027820. DOI: 10.1111/j.1551-2916.2006.01213.x.

[58] Sung Wng Kim et al. “Synthesis of a Room Temperature Stable 12CaO · 7Al 2 O 3 Electride from the Melt and Its Application as an Electron Field Emitter”. In: *Chemistry of Materials* 18.7 (2006), pp. 1938–1944. ISSN: 0897-4756. DOI: 10.1021/cm052367e.

[59] Sung Wng Kim et al. “Fabrication of room temperature-stable 12CaO · 7Al2O3 electride: a review”. In: *Journal of Materials Science: Materials in Electronics* 18.S1 (2007), pp. 5–14. ISSN: 0957-4522. DOI: 10.1007/s10854-007-9183-y.

[60] Sung Wng Kim et al. “Metallic state in a lime-alumina compound with nanoporous structure”. In: *Nano letters* 7.5 (2007), pp. 1138–1143. ISSN: 1530-6984. DOI: 10.1021/nl062717b.

[61] Charles Kittel. *Einführung in die Festkörperphysik*. 14., überarb. und erw. Aufl. München: Oldenbourg, 2006. ISBN: 978-3-486-57723-5.

[62] Charles Kittel and Siegfried Hunklinger. *Einführung in die Festkörperphysik*. 15., unveränderte Auflage. München: Oldenbourg Verlag, 2013. ISBN: 9783486597554.

[63] Peter. Klaeboe. “The Raman spectra of some iodine, bromine, and iodine monochloride charge-transfer coomplexes in solution”. In: *Journal of the American Chemical Society* 89.15 (1967), pp. 3667–3676. ISSN: 0002-7863. DOI: 10.1021/ja00991a001.

[64] Nils Gerrit Kottke, Franz Georg Hey, and Martin Tajmar. “Iodine Hollow Cathode Development and Testing with Alternative Emitters: IEPC-2022-120”. In: *37th International Electric Propulsion Conference IEPC*. 2022.

[65] Dan R. Lev et al. “Recent progress in research and development of hollow cathodes for electric propulsion”. In: *Reviews of Modern Plasma Physics* 3.1 (2019), p. 1560. DOI: 10.1007/s41614-019-0026-0.

[66] Fan Li, Xin Zhang, and Hongliang Liu. “Insights into the direct formation of [Ca 24 Al 28 O 64] 4+ (4e −) and its electrical characterization”. In: *Journal of the American Ceramic Society* 103.1 (2020), pp. 35–42. ISSN: 00027820. DOI: 10.1111/jace.16769.

[67] Fan Li et al. “In situ synthesis of [Ca 24 Al 28 O 64] 4+ (4e −) electride ceramic from C12A7 + C3A mixture precursor”. In: *Journal of the American Ceramic Society* (2018). ISSN: 00027820. DOI: 10.1111/jace.16103.

[68] Fan Li et al. “Rapid synthesis of inorganic [Ca24Al28O64]4+(e−)4 electride and its performance as an electron thermal emitter”. In: *Vacuum* 158 (2018), pp. 152–157. ISSN: 0042207X. DOI: 10.1016/j.vacuum.2018.09.055.

[69] Zhenyu Li et al. “Is mayenite without clathrated oxygen an inorganic electride?” In: *Angewandte Chemie (International ed. in English)* 43.47 (2004), pp. 6479–6482. ISSN: 1433-7851. DOI: 10.1002/anie.200461200.

[70] Jesse A. Linnell and Alec D. Gallimore. “Efficiency Analysis of a Hall Thruster Operating with Krypton and Xenon”. In: *Journal of Propulsion and Power* 22.6 (2006), pp. 1402–1418. ISSN: 0748-4658. DOI: 10.2514/1.19613.

[71] Peter Linstrom. *NIST Chemistry WebBook, NIST Standard Reference Database 69*. 1997. DOI: 10.18434/T4D303.

[72] *Lunar Polar Hydrogen Mapper Press Kit*. 2022. URL: https://lunahmap.asu.edu/sites/default/files/asu_lunah-map_press-kit_final-090122-spread_highr.pdf.

[73] Jason M. Makela, Dean R. Massey, and Lyon B. King. “Bismuth Hollow Cathode for Hall Thrusters”. In: *Journal of Propulsion and Power* 24.1 (2008), pp. 142–146. ISSN: 0748-4658. DOI: 10.2514/1.29389.

[74] Satoru Matsuishi et al. “High-density electron anions in a nanoporous single crystal: Ca24Al28O644+(4e-)”. In: *Science (New York, N.Y.)* 301.5633 (2003), pp. 626–629. DOI: 10.1126/science.1083842.

[75] Satoru Matsuishi et al. “Localized and Delocalized Electrons in Room-Temperature Stable Electride [Ca 24 Al 28 O 64] 4+ (O 2-) 2-x (e-) 2x : Analysis of Optical Reflectance Spectra”. In: *The Journal of Physical Chemistry C* 112.12 (2008), pp. 4753–4760. ISSN: 1932-7447. DOI: 10.1021/jp711631j.

[76] Michael S. McDonald and Natalie Caruso. “Ignition and Early Operating Characteristics of a Low-Current C12A7 Hollow Cathode: IEPC-2017-253”. In: *35th International Electric Propulsion Conference IEPC*. 2017.

[77] Michael S. McDonald, Natalie Caruso, and Margaret M. Mooney. “Multiple Orifices and Integrated Radiation Shielding in the Hollow Cathode Keeper: IEPC-2019-929”. In: *36th International Electric Propulsion Conference IEPC*. 2019.

[78] Paul McMillan and Bernard Piriou. “Raman spectroscopy of calcium aluminate glasses and crystals”. In: *Journal of Non-Crystalline Solids* 55.2 (1983), pp. 221–242. ISSN: 0022-3093. DOI: 10.1016/0022-3093(83)90672-5.

[79] Ernst Messerschmid and Stefanos Fasoulas. *Raumfahrtsysteme: Eine Einführung mit Übungen und Lösungen*. 5., aktualisierte und ergänzte Auflage. Berlin, Heidelberg: Springer Vieweg, 2017. ISBN: 978-3-662-49637-4. DOI: 10.1007/978-3-662-49638-1.

[80] Ioannis G. Mikellides et al. “Hollow cathode theory and experiment. II. A two-dimensional theoretical model of the emitter region”. In: *Journal of Applied Physics* 98.11 (2005), p. 113303. ISSN: 0039-6028. DOI: 10.1063/1.2135409.

[81] Masashi Miyakawa. “Fabrication of high-density electron-doped 12CaO · 7Al2O3 thin films by physical and chemical processes”. In: *Journal of the Ceramic Society of Japan* 117.1363 (2009), pp. 395–401. ISSN: 1882-0743. DOI: 10.2109/jcersj2.117.395.

[82] Masashi Miyakawa, Kiyoshi Kobayashi, and Takashi Taniguchi. “High-pressure synthesis of a 12CaO · 7Al 2 O 3 -12SrO · 7Al 2 O 3 solid solution”. In: *Journal of the American Ceramic Society* 100.4 (2017), pp. 1285–1289. ISSN: 00027820. DOI: 10.1111/jace.14743.

[83] Masashi Miyakawa et al. “Formation of inorganic electride thin films via site-selective extrusion by energetic inert gas ions”. In: *Journal of Applied Physics* 97.2 (2005), p. 023510. ISSN: 0039-6028. DOI: 10.1063/1.1829151.

[84] Masashi Miyakawa et al. “Novel Room Temperature Stable Electride 12SrO • 7Al2O3 Thin Films: Fabrication, Optical and Electron Transport Properties”. In: *Journal of the Ceramic Society of Japan* 115.1345 (2007), pp. 567–570. ISSN: 1882-0743. DOI: 10.2109/jcersj2.115.567.

[85] Masashi Miyakawa et al. “Fabrication and electron transport properties of epitaxial films of electron-doped 12CaO · 7Al2O3 and 12SrO · 7Al2O3”. In: *Journal of Solid State Chemistry* 183.2 (2010), pp. 385–391. ISSN: 00224596. DOI: 10.1016/j.jssc.2009.11.031.

[86] Detlev Möller. *Luft: Chemie, Physik, Biologie, Reinhaltung, Recht*. Berlin: De Gruyter, 2003. ISBN: 978-3-11-016431-2. DOI: 10.1515/9783110200225.

[87] Phuong-Vu Ong, Hideo Hosono, and Peter V. Sushko. “Structure and Electronic Properties of [Ca 24 Al 28 O 64] 4+ · 4e – Surfaces: Opportunities for Termination-Controlled Electron Transfer”. In: *The Journal of Physical Chemistry C* 123.10 (2019), pp. 6030–6036. ISSN: 1932-7447. DOI: 10.1021/acs.jpcc.8b11866.

[88] Yuy Oshio, Hiroki Watanabe, and Ikkoh Funaki. “Temperature and plasma measurement around the emitter region of the hollow cathode: IEPC-2022-123”. In: *37th International Electric Propulsion Conference IEPC*. 2022.

[89] Luis Palacios et al. “Crystal structures and in-situ formation study of mayenite electrides”. In: *Inorganic Chemistry* 46.10 (2007), pp. 4167–4176. ISSN: 0020-1669. DOI: 10.1021/ic0700497.

[90] Luis Palacios et al. “Structure and electrons in mayenite electrides”. In: *Inorganic Chemistry* 47.7 (2008), pp. 2661–2667. ISSN: 0020-1669. DOI: 10.1021/ic7021193.

[91] MICHAEL PATTERSON and JR.GEORGE WILLIAMS. “Krypton ion thruster performance”. In: *28th Joint Propulsion Conference and Exhibit*. Reston, Virigina: American Institute of Aeronautics and Astronautics, 1992. DOI: 10.2514/6.1992-3144.

[92] Daniela Pedrini et al. “Development of Hollow Cathodes for 5 to 20 kW Hall Thrusters: IEPC-2017-364”. In: *35th International Electric Propulsion Conference IEPC*. 2017.

[93] Chaiwat Phrompet et al. “Effect of free oxygen radical anions and free electrons in a Ca12Al14O33 cement structure on its optical, electronic and antibacterial properties”. In: *Heliyon* 5.5 (2019), e01808. ISSN: 2405-8440. DOI: 10.1016/j.heliyon.2019.e01808.

[94] J. F. Plaza, J. Toledo, and A. Post. “Excellent performance of a C12A7:e-cold cathode based on charge coupling techniques: IEPC-2022-136”. In: *37th International Electric Propulsion Conference IEPC*. 2022.

[95] Dmytro Rafalskyi et al. “In-orbit demonstration of an iodine electric propulsion system”. In: *Nature* 599.7885 (2021), pp. 411–415. ISSN: 1476-4687. DOI: 10.1038/s41586-021-04015-y.

[96] Lauren P. Rand and John d. Williams. “A Calcium Aluminate Electride Hollow Cathode”. In: *IEEE Transactions on Plasma Science* 43.1 (2015), pp. 190–194. ISSN: 0093-3813. DOI: 10.1109/TPS.2014.2338737.

[97] W. D. Rice et al. “Spin relaxation times of single-wall carbon nanotubes”. In: *Physical Review B* 88.4 (2013), p. 041401. ISSN: 1098-0121. DOI: 10.1103/PhysRevB.88.041401.

[98] Gaétan Sary, Laurent Garrigues, and Jean-Pierre Boeuf. “Hollow cathode modeling: I. A coupled plasma thermal two-dimensional model”. In: *Plasma Sources Science and Technology* 26.5 (2017), p. 055007. DOI: 10.1088/1361-6595/aa6217.

[99] Dominique Beatrice Schüpfer. “Strukturelle Umwandlungsprozesse in Kohlenstoffmaterialien: Korrelation von Raman-Spektren und Strukturanalysedaten”. Dissertation. Gießen: Justus-Liebig-Universität, 2020. URL: http://geb.uni-giessen.de/geb/volltexte/2021/15964/pdf/SchuepferDominique_2021_02_03.pdf.

[100] Andreas Siegel. *D6.5 Final report with test results: Internal report for NEMESIS project.*

[101] Jenő Sólyom. *Fundamentals of the physics of solids.* Vol. 1. Berlin: Springer, 2007. ISBN: 9783540725992.

[102] Jenő Sólyom. *Fundamentals of the physics of solids.* Vol. 2. Berlin: Springer, 2009. ISBN: 9783540853152.

[103] Jason D. Sommerville and Lyon B. King. “Hall-Effect Thruster–Cathode Coupling, Part I: Efficiency Improvements from an Extended Outer Pole”. In: *Journal of Propulsion and Power* 27.4 (2011), pp. 744–753. ISSN: 0748-4658. DOI: 10.2514/1.50123.

[104] Seigo Souma et al. “Direct Evidence for Cage Conduction Band in Superconducting Cement 12CaO · 7Al 2 O 3 by Low-Energy High-Resolution Photoemission Spectroscopy”. In: *Journal of the Physical Society of Japan* 79.10 (2010), p. 103704. ISSN: 0031-9015. DOI: 10.1143/JPSJ.79.103704.

[105] H. Stammreich, R. Forneris, and Y. Tavares. “High-resolution Raman spectroscopy in the red and near infra-red—I: Vibrational Raman spectrum of natural liquid chlorine”. In: *Spectrochimica Acta Part A: Molecular and Biomolecular Spectroscopy* (1961).

[106] Ulrich Stroth. *Plasmaphysik: Phänomene, Grundlagen, Anwendungen.* 1. Aufl. Studium. Wiesbaden: Vieweg + Teubner, 2011. ISBN: 9783834816153.

[107] Peter V. Sushko et al. “Hopping and optical absorption of electrons in nano-porous crystal 12CaO · 7Al2O3”. In: *Thin Solid Films* 445.2 (2003), pp. 161–167. ISSN: 00406090. DOI: 10.1016/S0040-6090(03)01156-8.

[108] Peter V. Sushko et al. “Mechanisms of oxygen ion diffusion in a nanoporous complex oxide 12CaO•7Al2O3”. In: *Physical Review B* 73.1 (2006), p. 547. ISSN: 1098-0121. DOI: 10.1103/PhysRevB.73.014101.

[109] Peter V. Sushko et al. “From insulator to electride: a theoretical model of nanoporous oxide 12CaO.7Al2O3”. In: *Journal of the American Chemical Society* 129.4 (2007), pp. 942–951. ISSN: 0002-7863. DOI: 10.1021/ja066177w.

[110] Howard E. Swanson, Thelma Isaacs, and Eloise H. Evans. *Circular of the Bureau of Standards no. 539 volume 9*. Gaithersburg, MD, 1960. DOI: 10.6028/NBS.CIRC.539v9.

[111] James Szabo et al. “High Density Hall Thruster Propellant Investigations”. In: *48th AIAA/ASME/SAE/ASEE Joint Propulsion Conference & Exhibit*. Reston, VA: American Institute of Aeronautics and Astronautics, 2012. ISBN: 978-1-60086-935-8. DOI: 10.2514/6.2012-3853.

[112] S. M. Sze and Kwok Kwok Ng. *Physics of semiconductor devices*. Third edition. Hoboken, NJ: Wiley-Interscience, 2007. ISBN: 9780471143239.

[113] Zachary R. Taillefer. “Characterization of the Near Plume Region of Hexaboride and Barium Oxide Hollow Cathodes operating on Xenon and Iodine”. Dissertation. Worcester Polytechnic Institute, 2018. URL: https://digital.wpi.edu/concern/etds/xw42n814p?locale=en.

[114] Zachary R. Taillefer, John J. Blandino, and James Szabo. “Characterization of a Barium Oxide Cathode Operating on Xenon and Iodine Propellants”. In: *Journal of Propulsion and Power* 36.4 (2020), pp. 575–585. ISSN: 0748-4658. DOI: 10.2514/1.B37315.

[115] Y. Toda et al. “Field Emission of Electron Anions Clathrated in Subnanometer-Sized Cages in [Ca24Al28O64]4+(4e-)”. In: *Advanced Materials* 16.8 (2004), pp. 685–689. ISSN: 09359648. DOI: 10.1002/adma.200306484.

[116] Y. Toda et al. “Work Function of a Room-Temperature, Stable Electride [Ca24 Al28 O64]4+(e–)4”. In: *Advanced Materials* 19.21 (2007), pp. 3564–3569. ISSN: 09359648. DOI: 10.1002/adma.200700663.

[117] Yoshitake Toda et al. “Surface of room-temperature-stable electride Ca24 Al28 O64 4+(e-)4: preparation and its characterization by atomic-resolution scanning tunneling microscopy”. In: *ACS nano* 5.3 (2011), pp. 1907–1914. DOI: 10.1021/nn102839k.

[118] J. Toledo et al. “Performance comparison of LaB6 and C12A7:e-emitters for space electric propulsion cathodes”. In: *IOP Conf. Ser.: Mater. Sci. Eng.* 2022.

[119] David Torréns-Martín et al. “Raman Spectroscopy of Anhydrous and Hydrated Calcium Aluminates and Sulfoaluminates”. In: *Journal of the American Ceramic Society* 96.11 (2013), pp. 3589–3595. ISSN: 00027820. DOI: 10.1111/jace.12535.

[120] L. J. van der Pauw. “A method of measuring specific resistivity and Hall effect of discs of arbitrary shape”. In: *Philips Research Reports* 13.1 (1958).

[121] L. J. van der Pauw. “A method of measuring the resistivity and hall coefficient on lamellae of arbitrary shape”. In: *Philips Technical Review* 20 (1958), pp. 220–224.

[122] Peter Vandenabeele. *Practical Raman Spectroscopy: An Introduction*. 1st ed. Analytical techniques in the sciences. Hoboken: John Wiley & Sons Incorporated, 2013. ISBN: 1119961904. DOI: 10.1002/9781119961284.

[123] Max Vaupel et al. “Iodine-compatible neutraliser for electric propulsion cubesats and small satellites: SP2022_269”. In: *8th International Conference on Space Propulsion*. 2022.

[124] Max Vaupel et al. “Iodine Fed Advanced Cusp Field Thruster Endurance Test Results: SP2022_092”. In: *8th International Conference on Space Propulsion*. 2022.

[125] Katja Waetzig. “Contacting Methods for C12A7 Electride Ceramic”. In: 01 (2019). DOI: 10.4416/JCST2019-00032.

[126] Katja Waetzig and Jochen Schilm. “Electronic, mechanical, and thermal properties of [Ca 24 Al 28 O 64] 4+ (4e −) electride ceramic”. In: *International Journal of Ceramic Engineering & Science* 3.4 (2021), pp. 165–172. ISSN: 2578-3270. DOI: 10.1002/ces2.10098.

[127] Katja Waetzig et al. “Improved Thermal and Mechanical Properties of [Ca 24 Al 28 O 64] 4+ (4e −) Electride Ceramic by Adding Mo Metal”. In: *Advanced Engineering Materials* 25.6 (2023). ISSN: 1438-1656. DOI: 10.1002/adem.202201286.

[128] H. H. Wittenberg. “Gas tube Design: Published in: Electron Tube Design by RCA Electron Tube Division”. In: *Electron Tube Design*. Ed. by RCA Electron Tube Division. Harrison, New Jersey, USA, 1962, pp. 792–817. URL: https://archive.org/details/ElectronTubeDesign/page/n799/mode/2up.

[129] Yixin Xiao, Xin Zhang, and Rongrong Li. “[Ca 24 Al 28 O 64] 4+ (4e −) are directly and quickly synthesized by self–reduction of C 12 H 10 Ca 3 O 14 + Al 2 O 3 without any reducing agent”. In: *Journal of the American Ceramic Society* 104.4 (2021), pp. 1641–1648. ISSN: 00027820. DOI: 10.1111/jace.17558.

[130] *XRD pattern for Calcium Aluminum Oxide extracted from X'Pert software. Data was calculated from ICSD-000260 using POWD-12++; PDF-No. 01-070-0134: Structure in database from Hoerkner, W., Mueller-Buschbaum, H., J. Inorg. Nucl. Chem. 38 p. 983 (1976)*. 1997.

[131] Osamu Yamaguchi, Akira Narai, and Kiyoshi Shimizu. "New Compound in the System SrO-Al2O3". In: *Journal of the American Ceramic Society* 69.2 (1986), pp. C–36–C–37. ISSN: 00027820. DOI: 10.1111/j.1151-2916.1986.tb04732.x.

[132] Shuwu Yang et al. "Formation and Desorption of Oxygen Species in Nanoporous Crystal 12CaO · 7Al 2 O 3". In: *Chemistry of Materials* 16.1 (2004), pp. 104–110. ISSN: 0897-4756. DOI: 10.1021/cm034755r.

[133] Peter Y. Yu and Manuel Cardona. *Fundamentals of semiconductors: Physics and materials properties*. Fourth edition. Graduate texts in physics. Heidelberg et al.: Springer, 2010. ISBN: 9783642007095.

[134] Zheng Yu et al. "Understanding Oxygen Nonstoichiometry in Mayenite: From Electride to Oxygen Radical Clathrate". In: *The Journal of Physical Chemistry C* 123.18 (2019), pp. 11982–11992. ISSN: 1932-7447. DOI: 10.1021/acs.jpcc.9b01995.

[135] Ivan D. Yushkov et al. "Resistance Switching in Polycrystalline C12A7 Electride". In: *Micromachines* 13.11 (2022). ISSN: 2072-666X. DOI: 10.3390/mi13111917.

[136] Xin Zhang et al. "Sr-doping enhanced electrical transport and thermionic emission of single crystal 12CaO · 7Al2O3 electride". In: *Current Applied Physics* 20.1 (2020), pp. 96–101. ISSN: 15671739. DOI: 10.1016/j.cap.2019.10.008.

[137] Jiping Zhao et al. "Synthesis and Characterization of (Ca 1−x Sr x) 12 Al 14 O 33 Electrides". In: *Crystal Research and Technology* 53.1 (2018), p. 1700201. ISSN: 02321300. DOI: 10.1002/crat.201700201.

[138] Daniel Zschätzsch. "Development of a hollow cathode neutralizer with the new insert material C12A7:2e− and the corroding effect of the alternative propellant iodine on satellite components". Dissertation. Gießen: Justus-Liebig-Universität, 2023.

[139] Daniel Zschätzsch et al. "Investigation of C12A7:e− under harsh conditions in relation to hollow cathode neutralizers". In: *2020(+1) RGCEP - Russian German Conference On Electric Propulsion*. 2021.

[140] Daniel Zschätzsch et al. "Corrosion of metal parts on satellites by iodine exposure in space". In: *Journal of Electric Propulsion* 1.1 (2022), pp. 1–24. ISSN: 2731-4596. DOI: 10.1007/s44205-022-00014-x.

[141] Daniel Zschätzsch et al. “Design and Operation of a Hollow Cathode with a C12A7:2e- Insert in Comparison with a LaB6 Insert: IEPC-2022-102”. In: *37th International Electric Propulsion Conference IEPC*. 2022.

Acknowledgements

I would like to express my sincere thanks and appreciation to all those who have supported me in this "Ph.D." venture. First and foremost, I would like to thank my supervisor, Professor Peter J. Klar. He supported the work that led to this dissertation with both a great deal of freedom, allowing me to develop my own approaches and research on the topic, and with useful advice when my research led to a dead end. Despite all the obstacles along the way, such as corona, the energy crisis or changing budgets, he ensured that I was able to focus on the science. I would also like to thank my second reviewer, Professor Hans Leiter, and the other members of the examining committee, Dr Elm and Professor Heiliger, for reviewing my thesis.

I would also like to thank all my colleagues at the *I. Physikalisches Institut*. Several of you have performed multiple measurements for me, sometimes with 'aesthetically pleasing' results. Special thanks go to Katrin Kroth and Limei Chen. Others simply accompanied me through my sometimes cheerful, sometimes frustrating research days. In particular, I would like to mention all my active and former colleagues in the ion thruster group. In the six years since I joined the group, I have had the pleasure of both learning from experienced predecessors and meeting new space enthusiasts. Kristof Holste, who warmly welcomed me into the group as a master student and always took the time to help me with both scientific and administrative problems. Patrick Dietz, who let me ignite my first ion thruster, Steffen Scharmann, who searched for the first pipe leak I produced. Benny Nauschütt, who programmed an own RPG to document the JUMBO venting procedure. Udo Bachmann, Felix Becker, Felix Kiefer, Andreas Wölki and Nicolas Bauer for their help on various projects. Konstantin Keil, who was a constant and funny companion on many conference trips and a reliable lunch organiser. Jana Zorn, my only female coworker, who shared many cups of tea and board game sessions with me. Special thanks to my 'cathode companion' Daniel Zschätzsch: Cathodes are delicate devices and we have both experienced this through endless, sometimes successful, but

often failed test campaigns. Thank you for your emotional and scientific support, which helped me to endure the long weeks until the first ignition.

My thanks also go to my friends and family who motivated me throughout this four year journey. My brother, whose encyclopaedic knowledge helped me with everything from orbital mechanics to reactions with thiosulphate, and who continuously fuelled my enthusiasm for space with new insight videos. My mum and dad, who sparked my fascination with science and who have been so proud and supportive of every step since. My boyfriend, who encouraged me through the long days of writing this thesis and always believed in me. Thank you all!

Declaration

I declare that I have completed this dissertation single-handedly without the unauthorized help of a second party and only with the assistance acknowledged therein. I have appropriately acknowledged and cited all text passages that are derived verbatim from or are based on the content of published work of others, and all information relating to verbal communications. I consent to the use of an anti-plagiarism software to check my thesis. I have abided by the principles of good scientific conduct laid down in the charter of the Justus Liebig University Giessen „Satzung der Justus-Liebig-Universität Gießen zur Sicherung guter wissenschaftlicher Praxis“ in carrying out the investigations described in the dissertation

Date	Signature